January-2005
CERN-SPSC 2005-002
SPSC P-307 Add.1

Atomic Spectroscopy and Collisions Using Slow Antiprotons

ASACUSA Collaboration (see page iii for the collaboration list)

Addendum to the proposal CERN/SPSC 97-19 and CERN/SPSC 2000-04

EXECUTIVE SUMMARY

After the one-year shutdown of the AD in 2005, ASACUSA collaboration plans to

1. continue already approved ASACUSA programme, namely, i) high-precision spectroscopy of antiprotonic helium atoms and ions, and ii) atomic collision experiments using very low energy antiprotons,

   and to

2. extend ASACUSA programme by including i) a CPT test by measuring the ground state hyperfine structure (GS-HFS) of antihydrogen and ii) measurements of $\overline{p}$-nucleus cross sections at low energy.

A roadmap of ASACUSA programme is shown in the next page.

Accordingly, this document is organized in four parts: In Part I, continuation of the approved ASACUSA programme is briefly described, and Part II discusses how we plan to extend ASACUSA programme. In Part III, we present our beam usage plan for 2006. Detailed technical descriptions are presented in Part IV.

ASACUSA - Atomic Spectroscopy and Collisions using Slow Antiprotons

Part I. Continuation of the approved ASACUSA programme	Spectroscopy (CPT)	Antiprotonic helium atoms and ions	Measure antiproton mass to $<< 10^{-9}$ Measure antiproton magnetic moment to $< 10^{-3}$
	Collision	Ionization cross section and antiprotonic atom formation cross section measurements	Antiprotons extracted from ASACUSA trap make these measurements possible
Part II. Exntending ASACUSA programme	Spectroscopy (CPT)	Antihydrogen ground-state hyperfine splitting (anti-atomic beam method)	Eventual sensitivity to possible CPT-violating effects will be higher than K^0-$\bar{K}^0$ comparison
	Collision	Measure antiproton-nucleus cross sections	Extend the LEAR measurements to much lower energy (eventually down to ~10 eV). Relevant to fundamental cosmology.

ASACUSA Collaboration List

Austria

M. Carnelli, H. Fuhrman, J. Marton, E. Widmann, J. Zmeskal

Stefan Meyer Institut für subatomare Physik, Boltzmanngasse 3, 1090 Vienna, Austria

Denmark

H. Knudsen, P. Kristiansen, U. I. Uggerhoj

Department of Physics and Astronomy, University of Aarhus, DK-8000 Aarhus C, Denmark

S.P. Møller *Institute for Storage Ring Facilities (ISA), University of Aarhus, DK-8000 Aarhus C, Denmark*

H.H. Andersen

Niels Bohr Institute, Blegdamsvej 17, DK-2100 København Ø, Denmark

Germany

T. Ichioka

MPI für Kernphysik (MPI-K), Heidelberg, Saupfercheckweg 1, 69117 Heidelberg, Germany

Hungary

D. Barna, D. Horváth, P. Zalán

Research Institute for Particle and Nuclear Physics, H-1525 Budapest, Hungary

B. Juhász, K. Tőkési

Institute of Nuclear Research (ATOMKI), H-4001 Debrecen, Hungary

Italy

M. Corradini, M. Leali, E. Lodi Rizzini, L. Venturelli, N. Zurlo

Dipartimento di Chimica e Fisica per l'Ingegneria e per i Materiali, Università di Brescia, 25123 Brescia, Italy

Japan

A.J. Dax, J. Eades , R.S. Hayano, T. Ishikawa, K. Gomikawa, N. Ono, W. Pirkl, T. Yamazaki

Department of Physics, University of Tokyo 7-3-1 Hongo, Bunkyo-ku, Tokyo 113-0033, Japan

K. Komaki, Y. Nagata, H.A. Torii, Y. Yamazaki

Institute of Physics, University of Tokyo, Komaba 3-8-1, Meguro-ku, Tokyo 153-8902, Japan and Atomic Physics Laboratory, RIKEN, Wako 351-01, Japan

Y. Kanai, N. Kuroda, A. Mohri, N. Oshima, M. Shibata, V. Varentsov, M. Wada

Atomic Physics Laboratory, RIKEN, Wako 351-01, Japan

Switzerland

M. Hori

CERN, H-1211 Genève 23, Switzerland

United Kingdom

M. Charlton

Department of Physics, University of Wales Swansea, Singleton Park, Swansea, SA2 8PP, UK

R. McCullough

Dept. of Pure and Applied Physics, Queen's University Belfast University Road, Belfast BT7 1NN, UK

Contents

Part I

Continuation of the approved ASACUSA programme

1. High precision spectroscopy of antiprotonic helium atoms and ions

1.1 Two-photon laser spectroscopy of antiprotonic helium atoms

We propose to carry out the first two-photon laser spectroscopy of the antiprotonic helium ($\overline{p}\mathrm{He}^+$) atom [1–4] and measure its transition frequencies to a precision of a few parts in 10^9. This may ultimately lead to a determination of the antiproton charge $Q_{\overline{p}}$ and mass $M_{\overline{p}}$ to a precision of a few parts in 10^{10}. In Fig. 1.1, limits $\delta_{\overline{p}}$ on the possible differences between $Q_{\overline{p}}$ and $M_{\overline{p}}$, and the corresponding proton values (M_p and Q_p) derived from measurements of $\overline{p}\mathrm{He}^+$ made by the ASACUSA collaboration over the years

$$\delta_{\overline{p}} = \frac{Q_p + Q_{\overline{p}}}{Q_p} \sim \frac{M_p - M_{\overline{p}}}{M_p} \tag{1.1}$$

are shown [5, 6]. The current limit, derived from a preliminary analysis of the experimental data taken in 2004, is $(2-3)\times 10^{-9}$. This determination relies on three-body QED calculations [7–11] and on several physical constants, the most important of these being the alpha particle-proton mass ratio

$$m_\alpha/m_p = 3.97259968907(52) \tag{1.2}$$

measured to a precision of 1.3×10^{-10}, and the cyclotron frequency of an antiproton confined in a magnetic field B,

$$\nu_c(\overline{p}) = \frac{-Q_{\overline{p}}B}{2\pi m_{\overline{p}}}, \tag{1.3}$$

measured by the TRAP collaboration [12] to a precision of 9×10^{-11}. The above considerations imply that if the experimental precision on the $\overline{p}\mathrm{He}^+$ transition frequencies were improved by a factor 10, the electgron-antiproton mass ratio could in principle be determined with an accuracy higher than even the electron-proton mass ratio

$$m_e/m_p = 5.4461702173(25) \times 10^{-4} \tag{1.4}$$

which is currently known to a precision of 5×10^{-10}.

In Fig. 1.2 (a), the profile of the $\overline{p}^4\mathrm{He}^+$ transition $(n, \ell) = (37, 35) \rightarrow (38, 34)$ at wavelength $\lambda = 726.1$ nm measured using a pulsed laser having the highest resolution which was commercially available is shown. In 2002, we improved the resolution [Fig. 1.2 (b)] by using more advanced laser techniques, and lower-energy antiproton beams emitted by a radiofrequency quadrupole decelerator (RFQD) [6, 13]. Two peaks separated by an interval $\Delta\nu = 1.8$ GHz can now be seen, which corresponds to the atom's hyperfine structure. In 2004, we attained the profile shown in Fig. 1.2 (c) by using a continuous-wave pulse-amplified dye laser with a resolution and accuracy 1–2 orders of magnitude higher than those previously available. The linewidth ($\Delta\nu \sim 0.5$ GHz) of this latest spectrum is limited by the Doppler broadening effect of $\overline{p}\mathrm{He}^+$ atoms undergoing thermal motion in the cryogenic helium target.

We intend to further increase the resolution by employing a two-photon spectroscopic technique to cancel the thermal Doppler broadening. As in our previous experiments, we plan to

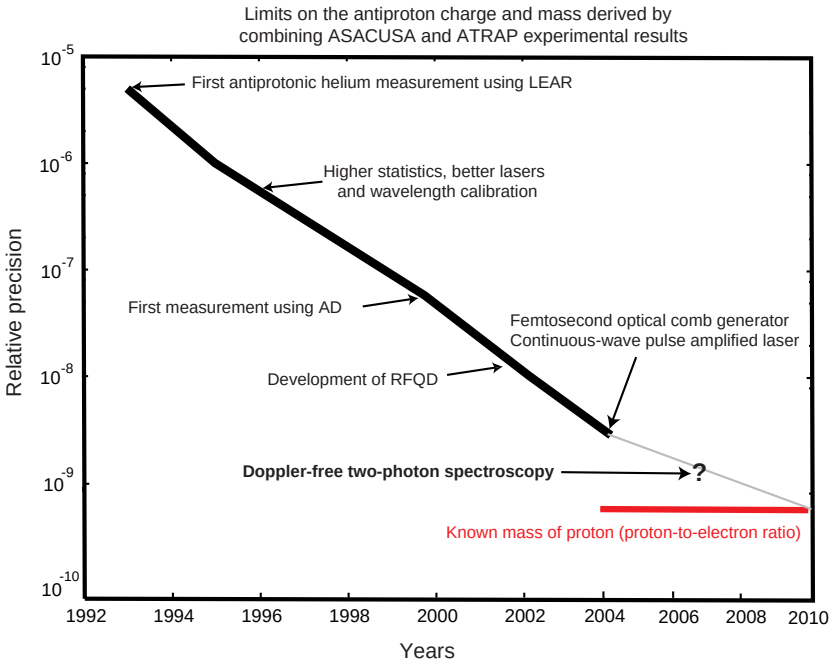

Figure 1.1: *Limit $\delta_{\rm CPT}$ on the possible differences between the antiproton mass $M_{\overline{p}}$ and charge $Q_{\overline{p}}$, and those of the proton's measured over the years, derived by combining the results of the $\overline{p}$He$^+$ laser spectroscopy and Penning trap experiments. The experimental techniques used to improve the precision on the $\overline{p}$He$^+$ transition frequencies over the years are indicated.*

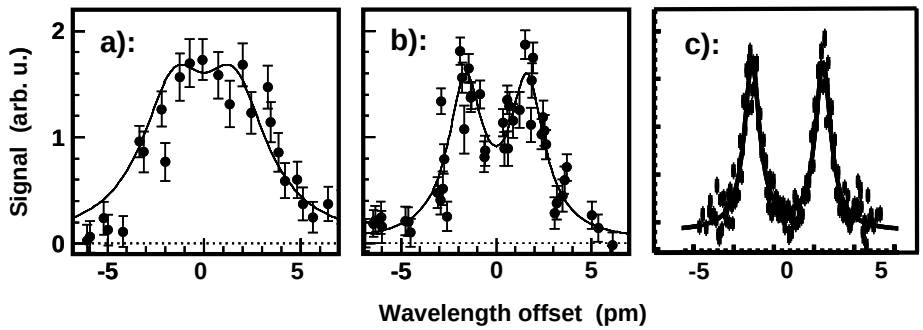

Figure 1.2: *Resonance profile of $\overline{p}^4$He transition $(n,\ell) = (37,35)\rightarrow(38,34)$ at $\lambda = 726.1$ nm, measured (a) using a pulsed laser with the highest resolution commercially available, (b) in 2002 using more advanced laser techniques and a radiofrequency quadrupole decelerator, (c) in 2004 using a continuous-wave pulse-amplified dye laser.*

stop antiprotons of energy $\sim$ 50 keV emitted by the RFQD in a cryogenic helium target of atomic density $\rho \sim 10^{17}$ cm^{-3}, thereby producing $\overline{p}^4$He$^+$ atoms. The atoms will then be irradiated by two counter-propagating laser beams, with their frequencies ν_1 and ν_2 adjusted such that i): their combined frequency $\nu_1 + \nu_2$ is tuned to a two-photon transition such as $(n,\ell) = (36,34)\rightarrow(34,32)$ involving an angular momentum change of $\Delta\ell = 2$, ii): the virtual intermediate state is tuned close to a real state [$(n,\ell) = (35,33)$ in the above example] leading

to an enhancement of the nonlinear two-photon transition probability. Under these conditions, the thermal Doppler width $\Delta\nu$ will diminish to

$$\left|\frac{\nu_1 - \nu_2}{\nu_1 + \nu_2}\right| \Delta\nu, \tag{1.5}$$

which is around ~ 30 MHz in the above example. It should then be possible to determine the $\overline{p}\mathrm{He}^+$ transition frequencies with a precision one order of magnitude higher than before.

1.2 Laser spectroscopy of antiprotonic helium ions

We plan to carry out the first laser spectroscopy of the antiprotonic helium ion ($\overline{p}\mathrm{He}^{2+}$) [14, 15], which is a singly-charged, two-body Coulomb system composed of an antiproton and a helium nucleus. Such an experiment could in principle lead to a determination of the antiproton charge and mass with even higher precision than those currently possible using the neutral three-body $\overline{p}\mathrm{He}^+$ atom. This is because all CPT tests involving $\overline{p}\mathrm{He}^+$ rely heavily on complicated three-body QED calculations to derive the atom's energy levels, the precisions of which are currently limited to several parts in 10^9. The ion, on the other hand, constitutes an ideal semiclassical Bohr system whose spin-independent parts of the energy levels (left side of Fig. 1.3) can be determined to very high precision (10^{-8}) using the simple equation,

$$E_n = -\frac{4R_\infty hc}{n_i^2}\frac{M}{m_e}\frac{Q_{\overline{p}}^2}{e^2} \tag{1.6}$$

where the reduced mass of the system is denoted by M, the electron mass by m_e, the Rydberg constant by R_∞, and the antiproton and electron charges by $Q_{\overline{p}}$ and e.

In the proposed experiment, cold ions of the $\overline{p}^4\mathrm{He}^{2+}$ and $\overline{p}^3\mathrm{He}^{2+}$ isotopes with lifetimes ($\tau_i \sim 100$ ns) against annihilation, and principal and angular momentum quantum numbers $n_i = 28$–32 and $\ell_i = n_i - 1$ will be produced using methods demonstrated in past ASACUSA experiments [16]. Antiprotons of energy $E = 50$ keV ejected from the RFQD will be stopped in a helium target of pressure $P = 0.1$ bar and temperature $T = 6$ K, thereby producing $\overline{p}\mathrm{He}^+$. Laser transitions to an Auger-dominated state (n_A, ℓ_A) is subsequently induced, and a spontaneous Auger decay will then produce the nearest ionic state (n_{i1}, ℓ_{i1}):

$$\overline{p}\mathrm{He}^+_{(n,\ell)} \xrightarrow{h\nu} \overline{p}\mathrm{He}^+_{(n_A,\ell_A)} \rightarrow \overline{p}\mathrm{He}^{2+}_{(n_{i1},\ell_{i1})} + e^-. \tag{1.7}$$

A second laser pulse tuned to an ionic transition frequency then induces a further transition to an energetically lower-lying ionic state (n_{i2}, ℓ_{i2}):

$$\overline{p}\mathrm{He}^{2+}_{(n_{i1},\ell_{i1})} \xrightarrow{h\nu} \overline{p}\mathrm{He}^{2+}_{(n_{i2},\ell_{i2})} \tag{1.8}$$

The resonance signal is detected by measuring the slight difference of the lifetimes of states (n_{i1}, ℓ_{i1}) and (n_{i2}, ℓ_{i2}) against annihilation.

1.3 Antiprotonic helium hyperfine splitting spectroscopy for better determination of the antiproton magnetic moment

The hyperfine structure of $\overline{\mathrm{p}}\mathrm{He}^+$ is a consequence of the interaction of the magnetic moments of the electron and the antiproton, and is very unique due to the large angular momentum $\vec{L}_{\overline{p}}$ of

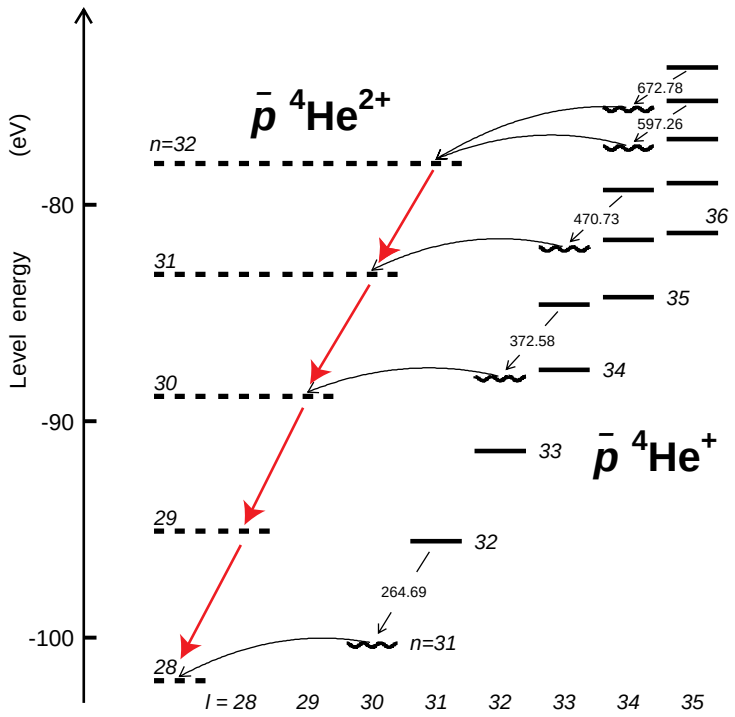

Figure 1.3: *Energy level diagram of* $\overline{p}^4\mathrm{He}^{2+}$ *ions and* $\overline{p}^4\mathrm{He}^{+}$ *atoms. Wavelengths of five* $\overline{p}^4\mathrm{He}^{+}$ *transitions used to ionize the electron are indicated in nanometers. Curved lines indicate Auger transitions to ionic states, red arrows radiative transitions in the* $\overline{p}\mathrm{He}^{2+}$ *ion.*

the antiproton. It leads to a splitting of each state (n, L) into a quadruplet (cf. Fig 1.4), with the dominant splitting arising from the interaction of $\vec{L}_{\overline{p}}$ with the electron spin $\vec{S}_{\mathrm{e}}$ with angular momentum $\vec{F} = \vec{L}_{\overline{p}} + \vec{S}_{\mathrm{e}}$ (called *hyperfine* (HF) splitting). The interaction of the antiproton spin $\vec{S}_{\overline{p}}$ with the other moments leads to a further splitting called *superhyperfine* (SHF) splitting, where the total angular momentum is given by $\vec{J} = \vec{F} + \vec{S}_{\overline{p}}$.

In 2001 and 2003 we performed measurements of the hyperfine structure (HFS) of the $(n, L) = (37, 35)$ state of antiprotonic helium using a laser-microwave-laser resonance method (see below). We measured the two microwave induced transitions with frequencies ν^{+}_{HF} and ν^{-}_{HF}, resp., with a relative precision of 3×10^{-5} [17]. The values agree with recent theoretical calculations [18–20] on a level of 6×10^{-5}, which roughly corresponds to the estimated theoretical accuracy. The measured microwave resonance frequencies, ν^{+}_{HF} and ν^{-}_{HF}, are primarily sensitive to the $\overline{\mathrm{p}}$ *orbital* magnetic moment, and constitute a first measurement of the orbital g-factor for either proton or antiproton with an accuracy of 6×10^{-5}. On the other hand, the splitting between ν^{+}_{HF} and ν^{-}_{HF} is caused by the $\overline{\mathrm{p}}$ spin magnetic moment $\vec{\mu}_{\overline{p}}$ which is currently known with a precision of 0.3% [21]. The experimental error on $\nu^{+}_{\mathrm{HF}} - \nu^{-}_{\mathrm{HF}}$ is much larger that the precision on each frequency, yielding a value for $\vec{\mu}_{\overline{p}}$ with an error of 1.6%. The theoretical precision for $\nu^{-}_{\mathrm{HF}} - \nu^{+}_{\mathrm{HF}}$ is the same as for each value separately (5×10^{-5}), so that no new calculations are needed if the experimental precision could be improved.

As shown below, an improvement of the experimental accuracy by one order of magnitude is possible using the newly developed pulse-amplified cw laser system which has a much narrower band width, better shot-to-shot frequency stability, longer pulse width and longer time delay

between two pulses than the previously used system. This would correspond to an improvement of $\vec{\mu}_{\overline{p}}$ by a factor 2 or more.

1.3.1 Improved laser-microwave-laser method

Since all SHF levels of same (n, L) are thermally equally populated, a laser pulse at $t = t_1$ of frequency f_+ is used to transfer a large fraction of the population of the F^+ doublet to a short-lived daughter state, from where the $\overline{\mathrm{p}}$ quickly annihilates with a nucleon of the He nucleus. Microwave radiation resonant with ν^-_{HF} or ν^+_{HF} transfers population from the F^- doublet to the F^+ one, and a second laser pulse of frequency f_+ measures the population of the F^+ doublet at time $t_2 > t_1$. We fire two subsequent laser pulses of constant frequency into the helium target, while scanning the frequency ν_{MW} of microwave radiation applied in between t_1 and t_2. Each laser pulse leads to a spike in the analogue delayed annihilation time spectrum (ADATS), whose area $I(t)$ is proportional to the population of the level F^+ at time t. We therefore measure the ratio $R = I(t_2)/I(t_1)$ as a function of ν_{MW}, expecting an increase if $\nu_{\mathrm{MW}} = \nu^{\pm}_{\mathrm{HF}}$.

Essential for the signal-to-noise ratio in this measurement is the bandwidth and depopulation efficiency of the lasers used. Fig. 1.2 compares a laser resonance scan of the 726 nm line with the pure pulsed laser system we used so far (middle, laser bandwidth $\sim$ 600 MHz) and the newly developed pulse-amplified cw laser system employed in 2004 (bottom, laser bandwidth $\sim$ 50 MHz). As can be seen, the new laser system leads to a complete separation of the f_+ and f_- lines, so that a laser pulse of frequency f_+ will not any more also partially depopulate the F^- doublet. Furthermore, the pulse length of the new laser was 10 ns as compared to 3 ns before, and can probably be extended to 30 ns. Since the daughter state of the 726 nm transitions has an Auger lifetime exceeding 10 ns, the longer laser pulse translates in a much improved depletion efficiency yielding a larger signal-to-noise ratio.

A further large improvement will result from the much better shot-to-shot frequency stability. This will also allow the increase of the time distance $\Delta t = t_2$–t_1 between the two laser pulses,

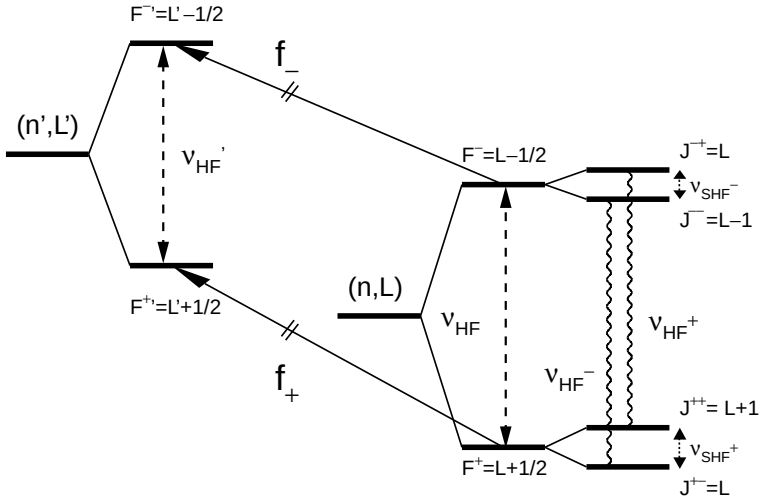

Figure 1.4: *Schematic view of the HF and SHF splitting of a* $\overline{\mathrm{p}}He^+$ *state* (n, L)*, and laser transitions to a short-lived daughter state* (n', L')*. Only laser transitions between HF states are shown because our laser system cannot resolve transitions between SHF levels. Wavy lines denote allowed magnetic transitions associated with an electron spin flip.*

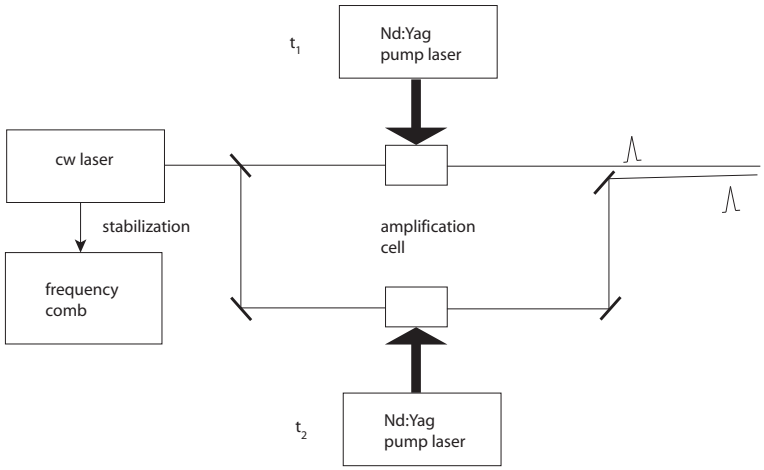

Figure 1.5: *Schematic layout of a frequency-stabilized cw laser with two amplifications stages pumped independently by two Nd:YAG lasers.*

which via the Fourier limit is most likely the largest contributor to the ~ 6 MHz linewidth of our recently obtained microwave spectrum (see Status report 2003). Previously the output of one pulsed laser was split and one part was delayed by multiple reflection between mirrors. This way a maximum delay of $\Delta t = 140$ ns could be achieved without seriously degrading the beam profile.

Using a layout depicted in Fig. 1.5, where the output of a stabilized cw laser is split and amplified in two separate stages pumped by two independent Nd:YAG lasers, pulses with arbitrary delay but identical frequency can be obtained. E.g. an extension from 140 ns to 1 μs would result in a factor 7 narrower linewidth, i.e. < 1 MHz. Whether this is achievable will depend on the influence of collisional broadening and collisional deexcitation processes which might reduce the population asymmetry if Δt becomes too large. Theoretical estimates [22–24] show that both effects might not be a problem under these conditions.

Both major improvements together, the much enlarged signal to noise ratio and the reduction of the linewidth of the microwave resonance lines are likely to result in an improvement of the experimental accuracy of a factor 10 or more, which would reduce the error on the difference $\nu_{\mathrm{HF}}^{-} - \nu_{\mathrm{HF}}^{+}$ to less than 0.1%, which corresponds to the same relative error of the antiproton magnetic moment and therefore an improvement of a factor 3–5 over the current best value.

With the improved stability of the laser system, a total beam time of 4 weeks including set-up and optimization of the laser parameters like power density and time delay between two pulses will be necessary.

2. Atomic collision experiments

2.1 Ultra slow antiproton beams

As is described in the status report, we have succeeded in preparing intense and monoenergetic antiproton beams of 10eV-500eV, which enables, for the first time, to study elementary processes of antiprotonic atom ($\bar{p}A^+$) formation under well-defined conditions [25]. Various antiprotonic atoms such as protonium ($\bar{p}p$), the simplest pure hadronic atom, and $\bar{p}He^{++}$ are expected to keep their intrinsic metastability when they are in vacuum.

2.2 Antiprotonic atom formation processes

When an antiproton approaches an atom with its velocity much lower than the Bohr velocity, the outermost target electron is repelled and accordingly the binding energy of the electron gets shallower, and eventually the electron is released. During this release process, the kinetic energy of the incoming antiproton is consumed, and if the kinetic energy is not high enough to supply the binding energy of the electron, the antiproton is bound to the target nucleus after the electron release, *i.e.*, an antiprotonic atom is formed. In other words, the electron releasing process results either in a simple ionization or in an antiprotonic atom formation depending on the kinetic energy of the antiproton (The same story also holds for other "heavy electrons" like μ^-,π^-, and K^-) [26]. A simple argument on kinematics gives the principal quantum number n of $\bar{p}A^+$ to be

$$n \sim \sqrt{\frac{\mu_{\bar{p}A}}{m_e}\frac{\epsilon_R}{\epsilon_{eA^+} - K_{\bar{p}A}}}, \tag{2.1}$$

where $\mu_{\bar{p}A}$ is the reduced mass of antiproton and atom A, m_e is the electron mass, ϵ_R is the Rydberg constant ($\sim$13.6 eV), ϵ_{eA^+} is the initial binding energy of the released electron, and $K_{\bar{p}A}$ is the initial kinetic energy in the center of mass frame. Equation (2.1) tells that n is a function of $K_{\bar{p}A}$, which varies from $n_{min}(\sim \sqrt{(\mu_{\bar{p}A}/m_e)(\epsilon_R/\epsilon_{eA^+})})$ to ∞ as $K_{\bar{p}A}$ is increased from 0 to ϵ_{eA^+} in the center of mass frame. Because the momentum carried by the released electron is fairly small, the momentum of $\bar{p}A^+$ is practically the same as that of the incident $\bar{p}$. Such a rigorous "momentum conservation" does not hold for molecular targets as discussed later, because the released particle is heavy and can take care of additional momentum.

Among various antiprotonic atoms, protonium ($\bar{p}p$) is particularly interesting because it is the simplest.Such a two-body system in high Rydberg Yrast states can cascade down only via slow radiative transitions with its lifetime much longer than 1 μsec. Quantitative evaluations were made by Cohen employing a CTMC (Classical Trajectory Monte Carlo) method and an FMD (Fermion Molecular Dynamics) method for various atomic and molecular targets [27]. The results for H atoms are given in Fig. 2.1. A clear threshold is seen at 27 eV for $\sigma_{\bar{p}p}$ although the total cross section σ_t varies smoothly across the threshold as described above.

In the case of molecular targets, an antiprotonic molecule is temporarily formed, which then dissociates into an antiprotonic atom and a residual atom(ion) [27]. A qualitative difference of molecular targets from atomic targets is that a molecule has a rather large internal momentum,

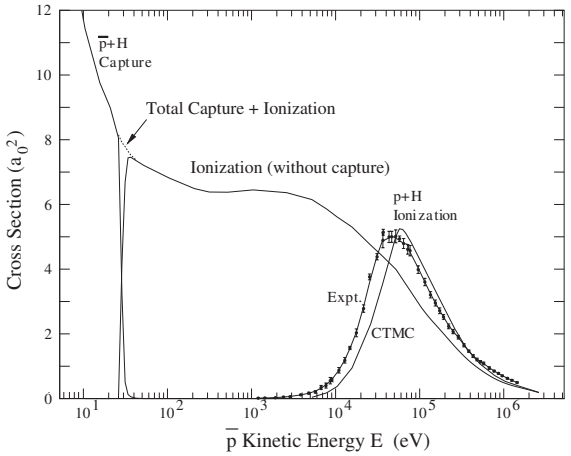

Figure 2.1: *The protonium formation cross section and the ionization cross sections for collisions between antiprotons and H atoms in the laboratory frame evaluated with a CTMC calculation [27].*

which results in a dramatic increase of $\sigma_{\bar{p}p}$ for H_2 as compared with H far beyond the threshold energy for atomic hydrogen.

Various multi-electron antiprotonic atoms are also expected to have intrinsic meta-stability in vacuum when they are prepared under target density conditions sufficiently low that the only collision made in it by a given beam antiproton is the one that creates the antiprotonic atom. The CTMC calculation ([28]) shows that $\bar{p}$Ne can be formed even at relatively high impact energy of antiprotons because a multiple electron release process will play an important role, which in itself contains important information on the role of electron-electron correlation at low energy antiproton collisions.

A collision between a charged particle and a neutral atom (molecule) below a few eV is dominated by the polarization force. The reaction cross section in this case is given by $\sigma_{\rm pol} = \pi e\sqrt{2\alpha/K_{\bar{p}A}}$, where α is the dipole polarizability of an atom and is of the order of 1 atomic unit (a.u.: *e.g.*, $4.5a.u.$ for H and $1.4a.u.$ for He), *i.e.*, the interaction of the incident $\bar{p}$ with the induced dipole becomes important for $K_{\bar{p}A}$ of ~ 1 a.u. and lower. As is seen in Fig. 2.1, the CTMC simulation predicts such a feature for a hydrogen target when the antiproton energy is lower than ~ 50 eV.

Here we are going to study the antiprotonic atom formation processes employing

(1) collisions between 10-100eV $\overline{\rm p}$ beams and a high density supersonic gas jet,

(2) collisions between well-collimated 1meV-100meV neutral beams and antiprotons stored in a MRT (multi ring trap)[29],

(3) collisions between 10-100eV A^+ ions and antiprotons stored in the MRT and

(4) collisions between 1meV-10eV antiprotons with ions.

In the case of (1) and (3), the threshold behaviour of the antiprotonic atom formation can also be studied.

2.3 Stopping power and ionization cross section measurements.

The Atomic Collisions subgroup of this collaboration plans to perform 3 different experiments with slow antiprotons when the AD is revived in 2006, and in the following years. The experiments, their background and the apparatus are described in detail in APPENDIX E.4.

First, we wish to continue our investigation of the energy loss of slow antiprotons in matter. Our measurements in this field at the AD [30, 31] have already led to challenging results for the stopping power of metals and for the large-band-gap insulator LiF. For LiF, for example, we found experimentally, that for antiproton impact the energy loss is proportional to the projectile velocity at least down to $0.4v_{\mathrm{Bohr}}$, in contrast with the theoretically expected behavior, which has a cut-off in dE/dx well above such velocities. This has lead to much activity within theoretical groups such as that of Joachim Burgdörfer at TU Vienna. However, more data are needed to guide the development of a more complete understanding of the mechanisms for energy loss of slow particles. We therefore plan to measure dE/dx in gases and in their frozen state too, to investigate other insulating solid targets, as well as to investigate the dependence on the target phase. The necessary apparatus exists and is well tested.

Second, as described in section 2, during 2004 we achieved the capability to extract a beam of 250 eV antiprotons from the MUSASHI penning trap and to transport it into our AIA ionization apparatus. Preliminary measurements showed the setup to work well, as described in APPENDIX E.4. Furthermore, they indicate a cross section for single ionization of helium at 10 keV which is much different from the "best" calculations – but which on the other hand agree with extrapolations based on our LEAR data obtained at higher energies. We simply need beam time to perform the planned measurements of the cross sections for single and multiple ionization of atomic and molecular hydrogen, and of the noble gases.

Third, we have planned an experiment to measure the angular multiple scattering of slow antiprotons in thin amorphous foils. This will lead to a better understanding of the scattering of antiprotons in the screened Coulomb potential. Such information is very important for the design of other antiproton measurements, as well as for efforts to apply antiprotons in cancer therapy, as pursued by CERN experiment AD4.

Part II

Extending ASACUSA programme

1. Antihydrogen hyperfine structure measurement

1.1 Introduction

1.1.1 Hyperfine structure in hydrogen and antihydrogen

Since the ground state of antihydrogen has infinite lifetime, its high precision spectroscopy will give unprecedented accuracies in terms of CPT symmetry tests. In the case of hydrogen, the ground-state hyperfine splitting (GS-HFS) frequency ν_{HF} has been measured in a classic series of experiments which began in the 1930's with relatively simple atomic beam experiments, and culminated with maser experiments in the early 1970s which ultimately achieved a relative precision of order 10^{-12}. For the antihydrogen atom, a measurement of ν_{HF} with precision equal to that achieved in the hydrogen case some fifty years ago would constitute a commensurately precise test of CPT symmetry. It may also be interpreted in terms of the gravitational interaction of antimatter.

To the leading order, the GS-HFS of antihydrogen is proportional to the spin magnetic moment of the antiproton, $\vec{\mu}_{\bar{p}}$, which is experimentally known only at the level of 0.3%. Below the level of several ppm accuracy, ν_{HF} also depends on the electric and magnetic form factors of the antiproton (cf. section 1.1.2). The measurements of $\nu_{\mathrm{HF}}(\overline{\mathrm{H}})$ to a relative accuracy of better than 10^{-6} as discussed in this letter will therefore yield an improvement of the value of $\vec{\mu}_{\bar{p}}$ by three orders of magnitude, and give some insight into the structure of the antiproton. Furthermore, the only existing phenomenological extension of the standard model that includes CPT violations (the standard model extension – SME – of Kostelecky's group, see section 1.2) predicts that CPT violation in the 1S–2S transition is cancelled in first order, while for the hyperfine structure it is a leading-order effect. In addition, the parameters introduced by Kostelecky et al. have the dimension of energy (or frequency). Therefore, by measuring a relatively small quantity on an energy scale (like the 1.4 GHz GS-HFS splitting), a smaller relative accuracy is needed to reach the same absolute precision for a CPT test.

In other words, *within the framework of SME*, it is not necessary to measure the GS-HFS splitting to 18 digits in order for the measurement to be competitive with the oft-quoted "most sensitive CPT bound" $|m_{K^0} - m_{\bar{K^0}}|/m_{\mathrm{average}} < 10^{-18}$ [32]. This is because $|m_{K^0}c^2 - m_{\bar{K^0}}c^2|/h$ is constrained to $< 1.2 \times 10^5$ Hz in terms of frequency. The measurement of antihydrogen GS-HFS splitting to some 10^{-4} relative accuracy ($\Delta\nu \sim 100$ kHz) can thus already attain a sensitivity to the CPT-violating parameters as good as the $K^0 - \bar{K^0}$ comparison[1].

1.1.2 CPT invariance and atomic spectroscopy

Interpreting particle-antiparticle comparisons

In Table 1.1 and Fig. 1.1 we summarize the presently known physical quantities for the proton, the electron and the hydrogen atom, together with the precision of the theoretical values. Also shown are presently known CPT-invariant properties, which we define for a general case X as:

[1]Note that the $K^0 - \bar{K^0}$ test (sensitive to the a parameter) and the $H - \bar{H}$ test (sensitive to the b parameter) cannot be directly compared; the purpose of the discussion here is to illustrate the order of magnitude of the achievable sensitivity to the CPT-violating parameters.

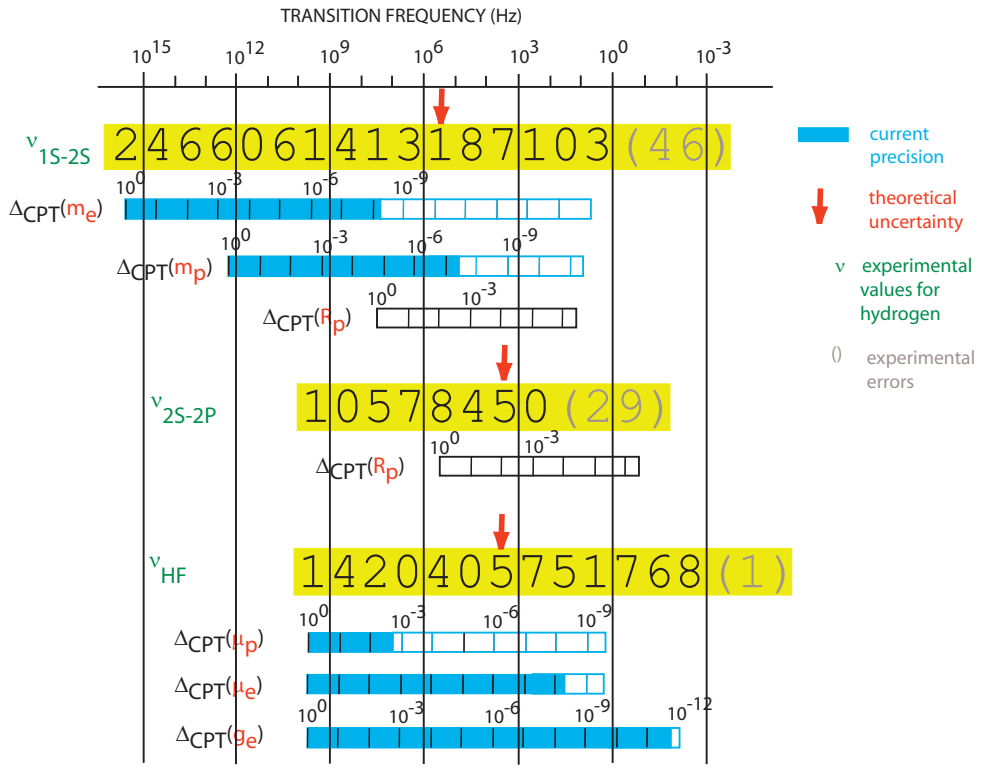

Figure 1.1: *Three experimental values (large numerical letters) of the 1S-2S transition frequency, 2S-2P Lamb shift and the 1S hyperfine frequency of hydrogen are presented together with the theoretical uncertainties. Known information on CPT symmetry is also shown (cf. Table 1.1).*

$$\Delta_{CPT}(X) = \frac{X(\text{antiparticle}) - X(\text{particle})}{X(\text{particle})}. \tag{1.1}$$

Although relative precisions like those of equation 1.1 are dimensionless, care must be taken in interpreting them. First, the scale of X is ambiguous in definition. Thus, Δ_{CPT} of the 1S *binding energy* of hydrogen must have the same significance in terms of CPT invariance as Δ_{CPT} of the *total energy including the rest mass* of the 1S state of hydrogen, but differs from it in absolute magnitude by 8 orders. Second, symmetry violations of all kinds depend on the nature of the physical observables involved. For instance, parity violation dominates only the weak interaction world and CP violation occurs only in the neutral K and B mesons. Nobody knows in which physical quantities CPT violation may appear.

The 1S-2S frequency for hydrogen and antihydrogen

The 1S-2S transition energy is primarily determined by the electron or positron Rydberg constant, as this is directly proportional to the reduced electron-proton (positron-antiproton) mass. Thus (as Fig. 1.1 illustrates) the positron mass determines the first significant figure of ν_{1S-2S} for antihydrogen while the antiproton mass only begins to take effect at the fourth digit. The *theoretical* uncertainty for the hydrogen atom is in the eleventh digit [34, 35] and is due to uncertainty of the experimental knowledge of the proton radius. Its value is determined from fits

to measured elastic electron-proton scattering data, which involve extrapolations to zero momentum transfer q. For some time the most precise value of $\sqrt{< R_{\rm p}^2 >} \equiv r_{\rm p} = 0.862(12)$ fm [42] was derived from data taken in Mainz at low q. A recent reanalysis of all world data, taking into account the effect of Coulomb distortion, has resulted in a significantly higher value of $r_{\rm p} = 0.895(18)$ fm [43]. This value is in agreement with the value extracted from the 1S–2S laser spectroscopy under the assumption that other QED calculations are correct ($r_{\rm p} = 0.890(14)$ fm [44]). A similar comparison of the latest experimental [36] and theoretical [37] values for the 1S Lamb shift (as shown in Table 1.1) yields again a smaller but more precise value of $r_{\rm p} = 0.873(8)$. This shows that our knowledge of the proton radius is still not satisfactory. In this sense, eleventh digit precision in determining the hydrogen and antihydrogen 1S-2S energies yields primarily information on the equality of the proton and antiproton charge distributions.

The classical Lamb shift for hydrogen and antihydrogen

The frequency interval $\nu_{\rm 2S-2P}$ between the $2S_{1/2}$ and $2P_{1/2}$ states of hydrogen has played an important role in the development of Quantum Electrodynamics, since it dominantly originates from QED effects. The experimental precision for $\nu_{\rm 2S-2P}$ is however rather limited due to the short lifetime of the $2P_{1/2}$ state of $\tau_{2P_{1/2}} = 1.6$ ns corresponding to a natural linewidth of 100 MHz, so that its use for high-precision CPT tests is not very promising.

The hyperfine frequency for hydrogen and antihydrogen

The 1S ground state of hydrogen is split due to the interaction of electron spin $\vec{S}_{\rm e}$ and proton spin $\vec{S_{\overline{p}}}$ according to $\vec{F} = \vec{S}_{\rm e} + \vec{S}_{\rm p}$ with quantum numbers $F = 0, 1$ (total spin) and $M =$

Table 1.1: *Measured quantities of proton, electron, and hydrogen. $m_{\rm e}$: electron mass, $m_{\rm p}$: proton mass, $R_{\rm p}$: proton radius, $\mu_{\rm e}$: electron magnetic moment, $\mu_{\rm p}$ proton magnetic moment, $g_{\rm e}$ electron g-factor. $\delta_{\rm exp}$ and $\delta_{\rm th}$ denote the experimental or theoretical error.*

Measured quantities of hydrogen					
quantity	exp. value (Hz)	$\delta_{\rm exp}/\nu$	ref.	$\delta_{\rm th}/\nu$	ref.
$\nu_{\rm 1S-2S}$	2 466 061 413 187 103(46)	1.7×10^{-14}	[33]	1×10^{-11}	[34, 35]
$\nu_{\rm 2S-2P}$	1 057 8450(29)$\times 10^3$	2.7×10^{-6}	[36]	3.8×10^{-6}	[37]
$\nu_{\rm HFS}$	1 420 405 751.768(1)	7.0×10^{-13}	[38]	$(3.5 \pm 0.9) \times 10^{-6}$ *	[39]

Measured CPT quantities			
quantity	value		ref.
$\Delta_{\rm CPT}(m_{\rm e})$	8×10^{-9}		[40]
$\Delta_{\rm CPT}(m_{\rm p})$	1×10^{-8}		[6]
$\Delta_{\rm CPT}(R_{\rm p})$	—		
$\Delta_{\rm CPT}(\mu_{\rm p})$	$(-2.6 \pm 2.9) \times 10^{-3}$		[32]
$\Delta_{\rm CPT}(\mu_{\rm e})$	8×10^{-9}	**	
$\Delta_{\rm CPT}(g_{\rm e})$	$(-0.5 \pm 2.1) \times 10^{-12}$		[41]

* difference between theory and experiment $(\nu_{\rm th} - \nu_{\rm exp})/\nu_{\rm exp}$.
** the accuracy of the electron magnetic moment is determined by the accuracy of the electron mass.

$-1, 0, 1$ (projection of F onto the magnetic field axis). The hyperfine splitting between the $F = 0$ and $F = 1$ states of the hydrogen and antihydrogen atoms is directly proportional to both the electron(positron) and proton(antiproton) spin magnetic moments. As with the 1S-2S transition, it is extremely well-known empirically for hydrogen. The impact of this on quantum physics at every stage of its development has been considerable, as Ramsey's extremely useful and informative review [45] demonstrates. These studies date back to the early 1930's, when Rabi [46–48] made a simple Stern-Gerlach beamline of inhomogeneous magnetic fields used as spin-state selectors, through which hydrogen atoms were transported. The advent of magnetic resonance methods saw determinations of the hyperfine splitting of the hydrogen ground state via microwave-induced transitions, first by Nafe and Nelson [49] and later by Prodell and Kusch [50], who reached the highest relative precision of 4×10^{-8} of all atomic beam experiments. When it became possible to observe hydrogen atoms for times of order 10 seconds in a maser cavity, the precision increased accordingly [51], and it is in such experiments that the best value of $\nu_{\rm HF}$ with relative accuracy $< 10^{12}$ (cf. Table 1.1) was obtained.

The hyperfine coupling frequency $\nu_{\rm HF}$ in the hydrogen ground state is given to the leading term by the Fermi contact interaction, yielding

$$\nu_F = \frac{16}{3}(\frac{M_p}{M_p + m_e})^3 \frac{m_e}{M_p} \frac{\mu_p}{\mu_N} \, \alpha^2 c \, Ry, \tag{1.2}$$

which is a direct product of the electron magnetic moment and the anomalous proton magnetic moment (M_p, m_e denote proton and electron mass, c the speed of light, α the fine structure constant, and Ry the Rydberg constant). Using the known proton magnetic moment,

$$\mu_p = 2.792\ 847\ 386(63)\ \mu_N, \tag{1.3}$$

with

$$\mu_N = 7.622\ 591\ 4\ \text{MHz/T}, \tag{1.4}$$

this formula yields $\nu_F = 1418.84$ MHz[52], which is significantly different from the experimental value. This 1000-ppm discrepancy led to the discovery of the anomalous electron g-factor ($g_e = 2.002...$).

Even after higher-order QED corrections [34] still a significant difference between theory and experiment remained, as

$$\delta(\text{QED}) = \frac{\nu(\text{QED}) - \nu(\text{Exp})}{\nu(\text{Exp})} = 32.55(10)\ \text{ppm}. \tag{1.5}$$

This discrepancy was accounted for by the non-relativistic magnetic size correction (Zemach correction) [34]:

$$\Delta\nu(\text{Zemach}) = \nu_{\rm F} \frac{2Z\alpha m_{\rm e}}{\pi^2} \int \frac{d^3q}{q^4} \left[\frac{G_E(-q^2) G_M(-q^2)}{1+\kappa} - 1 \right], \tag{1.6}$$

where $\nu_{\rm F}$ is the Fermi contact term defined in eq. (1.2), $G_E(-q^2)$ and $G_M(-q^2)$ are the electric and magnetic form factors of the proton, and κ its anomalous magnetic moment. The Zemach corrections therefore contain both the magnetic and charge distribution of the proton.

A detailed treatment of the Zemach corrections can be found in [39], resulting in a deviation of the theoretical value from the experimental one by

$$\frac{\nu(\text{exp}) - \nu(\text{th})}{\nu(\text{exp})} = 3.5 \pm 0.9\ \text{ppm}. \tag{1.7}$$

But this result is derived assuming that the electric and magnetic radii are equal, which is not experimentally well verified. At least the uncertainty in the magnetic radius of the proton is much larger than in the electric one. Therefore the uncertainty in Eq. 1.7 could be up to a factor 3 larger [53].

A further structure effect, the proton polarizability, is only estimated to be 4 ± 2 ppm [53], of the same order as the value above. The "agreement" between theory and experiment is therefore only valid on a level of ~ 4 ppm. Thus, we can say that the uncertainty in the hyperfine structure reflects dominantly the electric and magnetic distribution of the proton, which is related to the origin of the proton anomalous magnetic moment, a current topic of particle-nuclear physics. A first measurement of the antihydrogen hyperfine structure will initially provide a better value for the poorly known antiproton magnetic moment ($\mu_{\overline{p}}$), the current 0.3 % relative precision of which has been obtained from the fine structure of heavy antiprotonic atoms [21] . Subsequent, more precise values of $\nu_{\rm HF}(\overline{\rm H})$ will yield information on the magnetic form factor of the antiproton ($G_M(\overline{p})$), etc.

1.2 A theoretical model for CPT violation

At what scale and in what kind of physical observables might we then find CPT violating effects and what might be their significance? As is well known, CPT violation would require the abandonment of one or more of the cherished axioms of relativistic quantum field theory, which has had conspicuous success in all domains of particle physics. It is the fact that even so, most physicists believe that for a variety of reasons the standard model is incomplete that drives speculation about CPT-violation. For example, since several of the conditions required in the mathematical proof of the CPT theorem no longer hold in string theory, CPT violation could be used as a signature for string theory.

In recent years, the group of V.A. Kostelecky at Indiana has developed an extension to the standard model that includes both CPT as well as Lorentz-invariance violating (LIV) terms in the Lagrangian of a quantum field theory [54–58]. Although this model does not directly predict any CPT violation nor LIV, it can be used as basis to compare CPT tests in different sectors, and as a guide where to look for possible CPT violating effects. In fact, various groups have already done so [12, 59–64]. We describe this particular model below (although we do not base our proposed study of the antihydrogen hyperfine structure on it alone).

For the case of hydrogen and antihydrogen, the model [58] has the feature that CPT-violation effects might modify the triplet-singlet hyperfine structures of both hydrogen and antihydrogen, but differently. By introducing a number of CPT-violating parameters (generically denoted by a, b, c, and d below) as well as Lorentz-invariance violating (LIV) terms these authors can relate each of various physical observables to the theoretical parameters. In the hydrogen atom this adds an energy correction to states with electron and proton spin components m_J and m_I with value (m_e and m_p denote the electron and proton mass, resp.):

$$\Delta E^{\rm H}(m_J, m_I) = a_0^e + a_0^p - c_{00}^e m_e - c_{00}^p m_p \tag{1.8}$$

$$+(-b_3^e + d_{30}^e m_e + H_{12}^e) m_J/|m_J| \tag{1.9}$$

$$+(-b_3^p + d_{30}^p m_p + H_{12}^p) m_I/|m_I|. \tag{1.10}$$

For antihydrogen, the parameters a, d, and H reverse sign. The anomalous energy terms $\Delta E^{\rm H}$ and $\Delta E^{\overline{\rm H}}$ arise from Lorentz invariance violation, among which the parameters a_0's and b_3's are responsible for CPT violation.

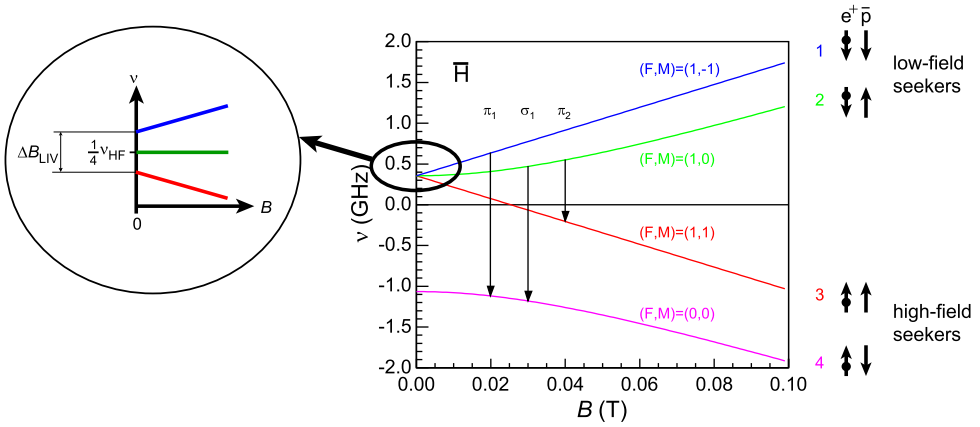

Figure 1.2: *Right: Zeeman splitting of the ground state hyperfine levels of antihydrogen (Breit-Rabi diagram). The spin alignments of positron and antiproton in the high-field limit, when the spins are decoupled, is shown to the right. Left: Zero-field splitting of the $F = 1$ states in the presence of a CPT violating interaction as predicted by Bluhm et al. [58].*

The parameters introduced by Kostelecky et al. have the dimension of energy (or frequency). Therefore, by measuring a relatively small quantity on an energy scale (like the 1.4 GHz GS-HFS splitting), a smaller relative accuracy is needed to reach the same absolute precision for a CPT test. Another advantage of a measurement of ν_{HF} comes from the fact that the transition energy is a difference of two energy levels, and therefore does not involve any of the above parameters (unless the transitions between hyperfine levels are measured in a magnetic field), making the 1S–2S transition frequency of free hydrogen and antihydrogen insensitive to the type of CPT violation described in this model. On the other hand, the hyperfine states have the following energy shifts ($|1\rangle$ to $|4\rangle$ refer to the different states as shown if Fig. 1.2)

$$\begin{aligned}
|1\rangle: &\quad \Delta E_1^H = -b_3^e - b_3^p + d_{30}^e m_e + d_{30}^p m_p + H_{12}^e + H_{12}^p \\
|2\rangle: &\quad \Delta E_2^H = -\cos 2\theta \, [b_3^e - b_3^p - d_{30}^e m_e + d_{30}^p m_p - H_{12}^e + H_{12}^p] \\
|3\rangle: &\quad \Delta E_3^H = -\Delta E_1^H \\
|4\rangle: &\quad \Delta E_4^H = -\Delta E_2^H,
\end{aligned} \tag{1.11}$$

where $\cos 2\theta$ represents the mixing of the $(1,0)$ and $(0,0)$ states (the mixing angle depends on the principal quantum number n and the magnetic fields B and obeys $\tan 2\theta_n \approx (51\mathrm{mT})/n^3 B$). In this way, the hyperfine transition frequencies are directly connected to the parameters of the spin-dependent terms.

In the presence of an external field B the $F = 1$ and $F = 0$ energy levels are split according to the Breit-Rabi formula

$$\begin{aligned}
|1\rangle: &\quad E_1 &&= \tfrac{1}{4}E_0 - \tfrac{1}{2}(g_J + g_I)\mu_B B + \Delta E_1 \\
|2\rangle: &\quad E_2 &&= -\tfrac{1}{4}E_0 + \tfrac{1}{2}E_0\sqrt{1+x^2} + \Delta E_2 \\
|3\rangle: &\quad E_3 &&= \tfrac{1}{4}E_0 + \tfrac{1}{2}(g_J + g_I)\mu_B B - \Delta E_1 \\
|4\rangle: &\quad E_4 &&= -\tfrac{1}{4}E_0 - \tfrac{1}{2}E_0\sqrt{1+x^2} - \Delta E_2, \\
\text{with} &\quad x &&= (g_I - g_J)\mu_{\mathrm{B}}\, B/E_0, \\
&\quad g_J &&= g_{e^-} = -2.0023193043718(75) \text{ (in units } \mu_{\mathrm{B}})[65], \\
\text{and} &\quad g_I &&= g_{\mathrm{p}}\, m_{\mathrm{e}}/m_{\mathrm{p}} = 0.003042064412(30) \text{ (in units } \mu_{\mathrm{B}})[65].
\end{aligned} \tag{1.12}$$

The formula is valid for both H and $\overline{\mathrm{H}}$, but due to the opposite sign of the magnetic moments of the antiparticles, the states $|1\rangle$ and $|3\rangle$ have different quantum numbers:

hydrogen	antihydrogen
$\|1\rangle \to (F,M) = (1,1)$	$\|1\rangle \to (1,-1)$,
$\|2\rangle \to (F,M) = (1,0)$	$\|2\rangle \to (1,0)$,
$\|3\rangle \to (F,M) = (1,-1)$	$\|3\rangle \to (1,1)$,
$\|4\rangle \to (F,M) = (0,0)$	$\|4\rangle \to (0,0)$.

(1.13)

One consequence of this model is that the degeneracy of the $F = 1$ triplet state at zero applied magnetic field (B) is lifted, giving the $(F,M) = (1,1)$ and $(1,-1)$ states opposite energy shifts, as shown in Fig. 1.2. The effect is as if a very small fictitious pseudo-magnetic field

$$\Delta B_{\mathrm{LIV}} = \frac{2\Delta E_1^{\mathrm{H}}}{g_{\mathrm{J}}\mu_{\mathrm{B}}} \tag{1.14}$$

is present in free space. Furthermore, a part of ΔE_1^{H} depends on the CPT-violating parameters, and changes sign for $\mathrm{H} \to \overline{\mathrm{H}}$. For a magnitude of the CPT-violating parameters leading to $\Delta E_1^{\mathrm{H}}/h = 1$ Hz, ΔB_{LIV} would be 10^{-6} Gauss. The quantization axis and the direction of the hypothetical pseudo-magnetic field must then somehow be defined, perhaps with respect to the earth's rotation axis (in which case the energy shifts would be subject to diurnal variation).

CPT-violation of this kind would therefore show up as hyperfine structure anomalies to be detected by studying spin-state polarizations. Were we dealing with muonium and antimuonium, the corresponding spin polarization would be revealed by the muon decay asymmetry. In the hydrogen/antihydrogen case this possibility is obviously not available; polarization states may nevertheless be selected and analyzed by their spin-dependent deflection in inhomogeneous magnetic fields. The hyperfine transitions that can be detected under these circumstances are (the upper sign of $\pm M$ stands for H, the lower one for $\overline{\mathrm{H}}$):

$$\begin{aligned}
&\pi_1: \ (F,M) = (1,\pm 1) \to (0,0): && \nu_{14} &&= \tfrac{1}{2}\nu_0 - \tfrac{1}{2}(g_J+g_I)\mu_B B/h + \tfrac{1}{2}\nu_0\sqrt{1+x^2} + \tfrac{\Delta E_1+\Delta E_2}{h}\\
&\pi_2: \ (F,M) = (1,0) \to (1,\mp 1): && \nu_{23} &&= \tfrac{1}{2}\nu_0\left[-1+\sqrt{1+x^2}\right] - \tfrac{1}{2}(g_J+g_I)\mu_B B/h + \tfrac{\Delta E_2-\Delta E_1}{h}\\
&\sigma_1: \ (F,M) = (1,0) \to (0,0): && \nu_{24} &&= \nu_0\sqrt{1+x^2} + \tfrac{2\Delta E_2}{h}.
\end{aligned} \tag{1.15}$$

The low-field seeking states $(1,\pm 1)$ and $(1,0)$ initially selected are converted to high-field seeking states $(1,\mp 1)$ and $(0,0)$. Since the transition frequencies of all these transitions are highly dependent on the external field, only zero or very low field conditions are experimentally suitable for high-precision spectroscopy. This implies that only the π_1 and σ_1 transitions can be measured. Their frequencies in the limit of $B \to 0$ ($\Delta E_2 \to 0$) are:

$$\begin{aligned}
&\pi_1: \ (F,M) = (1,\pm 1) \to (0,0): && \nu_{14} &&= \nu_0 + \tfrac{\Delta E_1}{h}\\
&\sigma_1: \ (F,M) = (1,0) \to (0,0): && \nu_{24} &&= \nu_0.
\end{aligned} \tag{1.16}$$

The π_1 resonance may then show an anomaly, while the σ_1 resonance does not.

1.3 Measurement of the ground-state hyperfine splitting

Maser conditions are probably unobtainable with antihydrogen at the moment, since the spin-state selected atoms are not trapped in the maser cavity, but make many wall collisions before

finding their way out through their entrance aperture. Attempts to measure $\nu_{\rm HF}$ by microwave spectroscopy in neutral-atom traps are limited in accuracy due to the inhomogeneous magnetic field used for trapping, and the finite temperature distribution of the trapped atoms. E.g. in a typical neutral-atom trap used for hydrogen spectroscopy [66], the atoms will experience Zeeman level shifts due to their thermal motion. So far experiments on RF-spectroscopy of trapped neutral atoms have not been able to achieve high precision, but only to extract the temperature distribution of atoms, even though these atoms had a temperature as small as 60 mK [67, 68].

We therefore plan to adopt a similar method to that of the classic hydrogen experiments. Thus we envisage a beamline in which the antihydrogen atoms emerging from the source pass through

i) an inhomogeneous magnetic field, which selects their spins and velocities,

ii) a microwave cavity which induces spin-flip transitions when tuned to $\nu_{\rm HF}$, and

iii) a second inhomogeneous field which analyzes the state of the spin-flipped atoms.

In contrast to the case of hydrogen, the number of antihydrogen atoms which can be expected is of course sharply limited. To compensate to some extent for this, we make use of sextupole magnet systems since these can accept and transport antihydrogen atoms emerging into a larger solid angle compared to Stern-Gerlach type experiments.

Interfacing a sextupole beamline to a nested Penning trap (à la ATHENA/ATRAP) turns out to be very difficult; axial extraction of antihydrogen atoms would result in a diminishingly small solid angle, while radial extraction would require an entirely new design of meshed electrodes and a split solenoid. In addition, a relatively large antihydrogen source size of the nested trap configuration is unfavourable in terms of $\bar{H}$ transport and focussing. We therefore propose to use different antihydrogen production methods, i) a radiofrequency Paul trap (Appendix B) and/or ii) a cusp trap (Appendix C).

The compact design of the Paul trap and its point-like source size makes it possible to couple the $\bar{H}$ source to the sextupole beamline with a much larger solid angle and a better optics than the nested-trap configuration. In case of the cusp trap, the source size is larger, but if spin-polarized antihydrogen atoms can be extracted as discussed in Appendix C, the first sextupole magnet in the beam line may be eliminated to achieve a larger detection solid angle.

A schematic view of the whole experimental apparatus is shown in Fig. 1.3. The two sextupole magnets S1 and S2 are aligned so as to accept antihydrogen atoms emitted transversally from the formation region. The focussing and spin selection in the sextupoles is based on the magnetic field gradient force which acts on the magnetic moment of the antihydrogen atoms. A strong magnetic field gradient will introduce a bend in their trajectory depending on the direction of their alignment with respect to the magnetic field. The four possible hyperfine states of an antihydrogen atom, characterized by the quantum numbers $F = 0, 1$ (total spin) and $M_F = -1, 0, 1$ (projection of F onto the magnetic field axes), then divide into two pairs: the so-called "high-field seekers", which move towards regions of higher magnetic field, and the "low-field seekers" (cf. Fig. 1.2) which move toward weaker-field regions.

For two identical sextupole magnets, the trajectories shown in Fig. 1.3 correspond to low-field seekers that do not change their spin direction inside the cavity. A resonant microwave field would transform the low-field seekers into high-field seeker, which would be blocked in S2, and the on-resonance count rate at the antihydrogen detector would drop from a constant off-resonance rate. The planned experimental setup is described in more details in Appendix A.

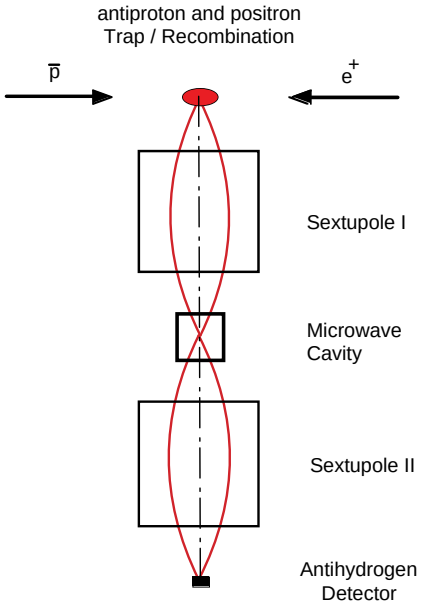

Figure 1.3: *A schematic layout of a simple microwave resonance experiment for antihydrogen. The antihydrogen atoms, which are produced in the central region of a charged particle trap, are transported via a pair of sextupole magnets. Spin selected antihydrogen atoms in the first sextupole magnet enter a microwave cavity and spin-flipped atoms are analyzed in the second magnet.*

2. $\bar{p}$-NUCLEUS CROSS SECTIONS AT LOW ENERGY

2.1 Introduction

The dynamics of the antiproton-nucleus ($\bar{p} - A$) interaction and the structure of the nucleus appear to affect in an unexpected way the behavior of the $\bar{p} - A$ annihilation cross section (σ_{ann}) at low energies. In light nuclei the $\bar{p}$−D and $\bar{p}$ −^{4}He annihilation cross sections at $\bar{p}$ momentum below 60 MeV/c drop to the $\bar{p} - p$ level, whereas at higher momenta ($\gtrsim$ 100 MeV/c) the $\bar{p}$ nucleus annihilation cross section increases regularly with the number of nucleons in the nuclei[69].

A recent low statistics measurement of the $\bar{p}$−^{20}Ne annihilation cross section at 57 MeV/c [70] seems to confirm a saturation effect of σ_{ann} with the mass number A at decreasing $\bar{p}$ momentum (see Fig.2.1), in agreement with the description of strong interaction effects in hadronic atoms, including $\bar{p}$ atoms. Moreover, a low statistics measurement in ^{3}He [71] obtained a value similar to the ^{20}Ne one, thus supporting a strong dependence on the nucleus structure.

To understand the behavior of $\sigma_{ann}(\bar{p} - A)$, experiments are needed to confirm the existing low statistics measurements, and additionally new measurements should be performed on $\bar{p}$ annihilation with heavier nuclei and at even lower energies.

2.1.1 The $\bar{N}$-nucleus , $\bar{N}$-nucleon interaction at low energies

The measurements performed at LEAR in 1980s on $\bar{p}$ [72] and $\bar{n}$ [73] annihilation on nuclei at momenta ranging from 600 down to 200 MeV/c yielded a cross section $\sigma_{ann} = \sigma_o A^\nu$ with $\nu \approx 2/3$.

The behaviour of σ_R (reaction cross section) with the incident momentum was similar for all nuclei and followed that of the $\bar{p} - p$ interaction (see Fig.2.1). This suggests a picture where the dominant reaction mechanism is the $\bar{N} - N$ annihilation on quasi-free nucleons and the differences in σ_R among the nuclei are explainable in terms of eclipse effects, which reduce the probability that a target nucleon is "seen" by the incident antinucleon.
At 200 MeV/c this picture of the $\bar{p}$-nucleus annihilation is questionable but experimental data on $\bar{p}$−^{20}Ne and $\bar{p}$−^{4}He are still in agreement with the $A^{2/3}$ law. Antineutron data [74] also follow this behavior from 280 MeV/c down to $\approx$ 60 MeV/c on target nuclei from intermediate to heavy.
On the contrary antiproton annihilation on light nuclei at momenta below 100 MeV/c seems to be very weakly dependent on the mass of the target nucleus against any naive expectation of a scaling law with the number of nucleons in the target. A set of measurements of antiproton-proton and antiproton-nucleus annihilation cross sections [70, 71, 75, 76] and of widths and shifts of spectroscopic transitions in antiprotonic atoms [77–79], together with several model analyses [80–90] have demonstrated that huge saturation effects dominate the $\bar{p}$-nucleus interaction, both in the negative energy bound state domain and in the positive energy reaction sector.

An "intersection" point at laboratory momentum 30 - 60 MeV/c exists (Fig.2.1) such that $\bar{p}$−D and $\bar{p}$−^{4}He annihilation cross sections are larger than $\bar{p} - p$ annihilation cross sections at larger momenta, but smaller at smaller momenta. Data on these nuclei are satisfactorily precise, but they are not enough to interpolate univocally the energy dependence of their annihilation

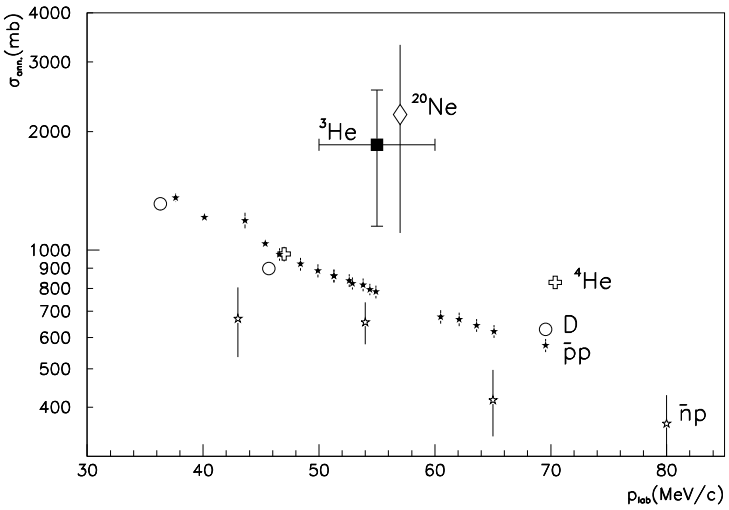

Figure 2.1: *Antiproton annihilation cross sections for p, D, ^{3}He, ^{4}He and Ne. Full stars and empty stars correspond respectively to $\bar{p}-p$ and $\bar{n}-p$ data. See text for references.*

rate below 100 MeV/c where S-wave scattering is even more dominant. Moreover, low-statistics data on $\bar{p}-^{20}$Ne and $\bar{p}-^3$He annihilation at about 60 MeV/c [70, 71] exist. When Coulomb effects are subtracted, the neon result has the same size as that of $\bar{p}-p$, while the ^{3}He result is twice as large as the others (including ^{4}He) at the same momentum.

On the interpretation side, it has been recently observed [87–89] that for low energy annihilations on nuclei a strong suppression has to be expected on the very general ground that large annihilation rates would contradict the Heisenberg uncertainty principle. It was demonstrated that annihilation cross sections should be approximately independent on the target mass number A, apart from Coulomb and surface effects. This result is in agreement with the optical-potential calculations [82, 86, 90] at least at very small momenta (see Fig. 2.2). These studies suggest that bulk nuclear matter effects are not relevant in the $\bar{p}$-nucleus physics at small energy, and Coulomb effects can be understood and subtracted [88]. Indeed, most of the above quoted potential models, and also phenomenological analyses [94–96] for the annihilation process suggest that the $\bar{N}-N$ and $\bar{N}$-nucleus annihilation processes take place in a thin spherical shell placed just outside the nuclear surface. This mechanism prevents any investigation of the target structure at low energies, but makes the annihilation an ideal tool for probing the details of the external region of the nucleus, such as the neutron/proton ratio at the nuclear surface or the extraction energy of the peripheral nucleons. Following the suggestions coming from the experiments on antiprotonic atoms, a certain correlation should exist between the annihilation probability and the extraction energy of the most peripheral nucleon, even if this correlation is not always verified and data on isotopes look contradictory [97]. Among the positive energy data available, ^{3}He and ^{4}He data seem to confirm the relevance of the extraction energy of the most peripheral nucleon, while deuteron data contradict it. Indeed, according to this point of view, $\bar{p}-$deuteron annihilation rates should be larger than $\bar{p}-^3$He ones (Coulomb effects apart), which should be larger than $\bar{p}-^4$He ones. Seemingly, the N/Z composition at the nuclear surface plays a non negligible role, in agreement with the fact that $\bar{n}-p$ annihilation rates are

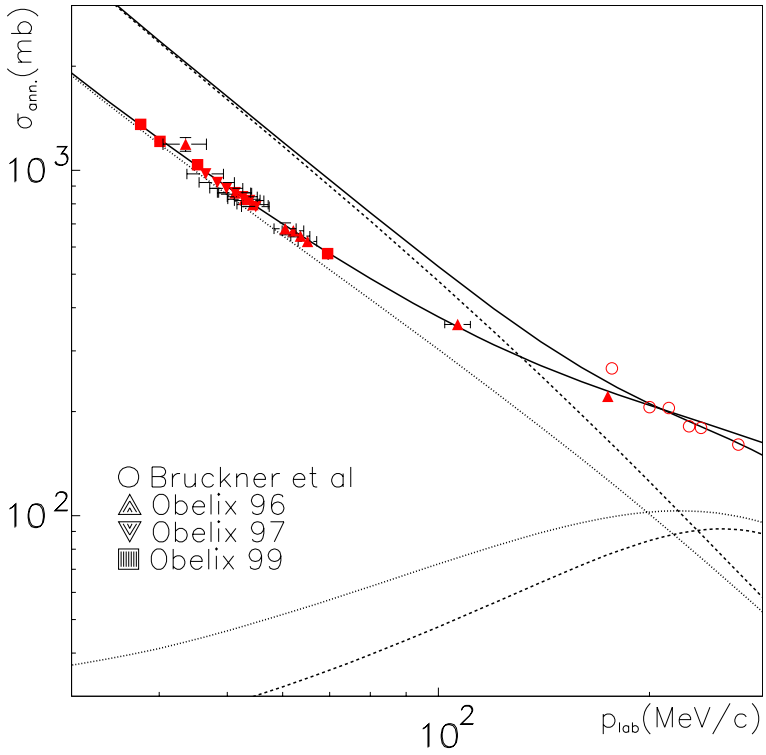

Figure 2.2: *Optical potential fits to $\bar{p} - p$ annihilation data. The continuous line fitting the low energy points corresponds to the potential described in [87]. The upper continuous line corresponds to the same potential modified by decreasing the imaginary strength from 8000 to 1000 MeV. Dotted lines show the S- and P-wave contributions for the former potential, dashed lines show the same for the latter. Data are taken from Brückner et al[91], and from the Obelix collaboration[76, 92, 93].*

lower than $\bar{p} - p$ ones at momenta 50-200 MeV/c [98]. In presence of more complete sets of data, well-tested few-body techniques exist that would permit to relate data on light nuclei to subnuclear interactions (at least in the case of D, ^{3}He and ^{4}He).

Measurements of the total annihilation cross sections for antinucleons on light nuclei are also relevant for fundamental cosmology[99–101]. The matter vs antimatter asymmetry of the visible universe does not match the approximate matter vs antimatter symmetry of the known physical laws. Several mechanisms have been proposed to explain the origin of the matter/antimatter asymmetry. One such is the possibility of the matter/antimatter asymmetry being a local one, so the universe would be composed by separated islands of matter and of antimatter, at the beginning of its life or perhaps still now. In this scenario, annihilation could play a relevant role in the border regions between matter and antimatter islands. In inflation based scenarios there are no arguments to constrain the magnitude of the space scale of the islands. For small distance scales antimatter islands have now disappeared and we surely need an asymmetric baryogenesis to explain the overall baryon dominance. For large distance scales antimatter islands could have survived until now. For intermediate distance scales most annihilations took place at about the nucleosynthesis time, or later but still before the recombination time. This means energies between 1 eV and 1 MeV (age of universe between 1 s and 30000 years). In this case we may have relevant production of high energy antinucleons in those antimatter regions where anti-

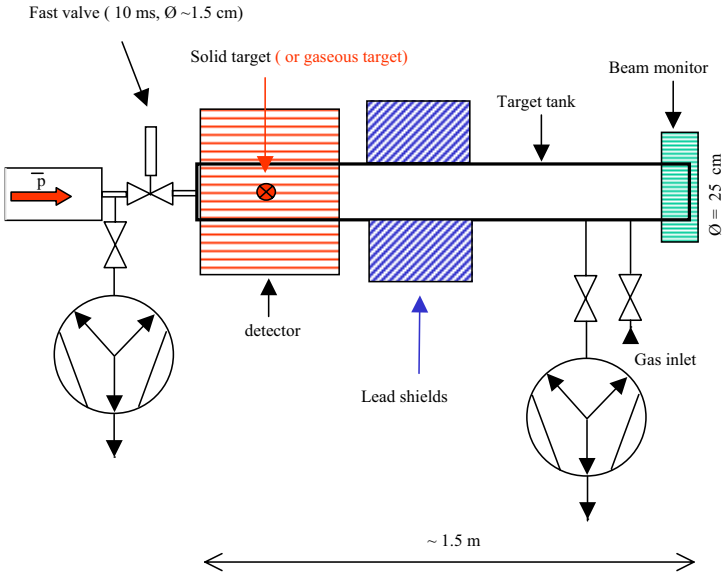

Figure 2.3: *Experimental set-up for* $E_k \approx 1 - 5$ *MeV.*

nucleosynthesis took place, as a consequence of the later annihilation of the antinuclei. Thus there are two stages of annihilation, the first one before nucleosynthesis, at $T \gtrsim 70$ keV, the second well after nucleosynthesis, at $T \lesssim 3$ keV. The physics during the two regimes is quite different. At first matter and antimatter are in the form of nucleons and antinucleons, after nucleosynthesis they are in the form of ions and anti-ions.

The precise evolution of these processes is strongly affected by the values of the corresponding cross sections. So the understanding of these phenomena could be seriously enhanced by measurements of antinucleon–light nucleus annihilation cross sections in the keV-MeV region.

On the other side, a comparison between data on light and heavy nuclei could permit to understand the real role of general quantum principles and of the nuclear surface.

2.2 Strategy of the measurements

2.2.1 Experimental technique for $\mathbf{E}_k \approx 1 - 5$ MeV

In order to investigate the dependence on the mass number of the $\bar{p}$-nucleus annihilation cross sections in the MeV region, we propose the experimental setup shown in Fig.2.3. The $\bar{p}$ beam from the AD will be focused on the entrance window of a target ($\sim$ 1.5 m long, 25 cm in diameter). The detector is a Scintillating Fiber Tracker, as shown in Fig.2.4, by which it will be possible to reconstruct the annihilation vertex by tracking at least two of the outgoing charged mesons. Thanks to the good time resolution ($\sim$1 ns) of this detector, we will disentangle tracks from different vertices. We will start data taking after antiprotons enter the gaseous target within a $40 - 50$ ns time gate, to avoid signals due to mesons from annihilation on the end wall.

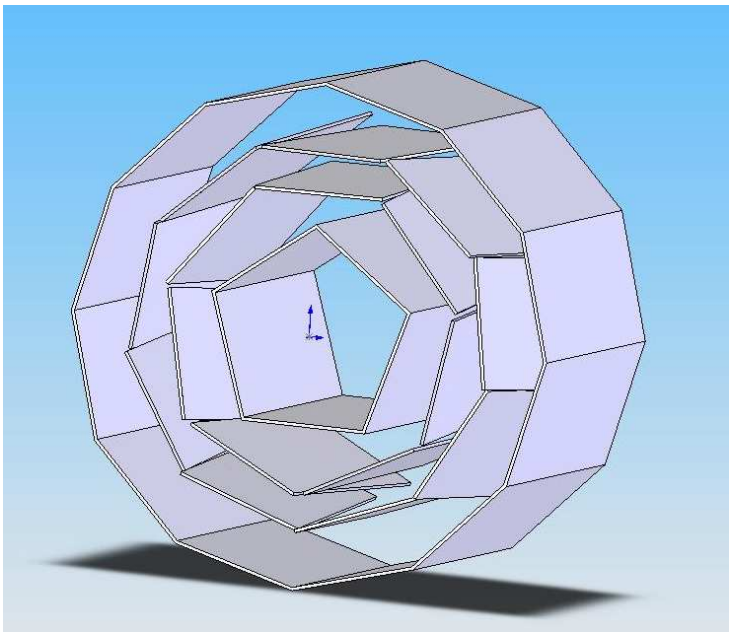

Figure 2.4: *Experimental set-up. Each module has* 20×40 cm^2.

We will use gaseous targets (^{3}He, ^{4}He, H_2, D_2) at $\approx$ 50 mbar pressure and/or thin solid targets (like C, Si with thicknesses of the order of 1 μm). The good knowledge of $\bar{p}$ annihilation cross sections in H_2 (Fig.2.1) will be useful. If we admix percentages of heavier atoms (Ne, Xe) or molecules into H_2 targets and compare the annihilation rates we will obtain ratios of annihilation cross sections in an unbiased way. Also, it will be possible to optimize data taking and analysis by inserting a thin solid target in H_2 gas and successively in the other gases to realize normalization and minimize errors in the ratios of annihilation cross sections on different nuclei.

We assume to acquire at least 10 events per AD shot: so in some hours we will obtain annihilation cross sections with $5\% - 10\%$ accuracy per sample, eventually taking advantage of the AD extraction mode in which each pulse is divided into 9 subpulses. Thanks to the AD-RFQD beam line of the ASACUSA collaboration in two weeks it will be possible to describe a good scenario for different nuclei and energies.

2.2.2 Experimental technique for $E_k \lesssim$1.5 keV

The proposed experimental setup is based on the Monoenergetic Ultra-Slow Antiproton Source for High-precision Investigation (MUSASHI), that releases antiprotons with energies in the range 10-1500 eV in a time interval $1 - 10$ s.

Low-energy antiprotons will enter a gaseous target (Fig.2.5) at low density ($P \lesssim 10^{-2}$ mbar): the tracker acquisition gate will start at the $\bar{p}$ starting time and will be open for $1 - 10$ s. All $\bar{p}$ annihilations can be acquired (acquisition rate of the order 10^6 Hz). The off-line selection of the fiducial volume will realize the collection of the in flight annihilation events. We will collect signals from annihilations on the lateral wall too, due to Rutherford scattering, and on the end wall. If $\bar{p}$ annihilation cross-sections scale as $1/v^2$, at 10^{-3} mbar pressure we will have some reconstructed in flight annihilation events per 10^6 antiprotons. We will use dilute samples of

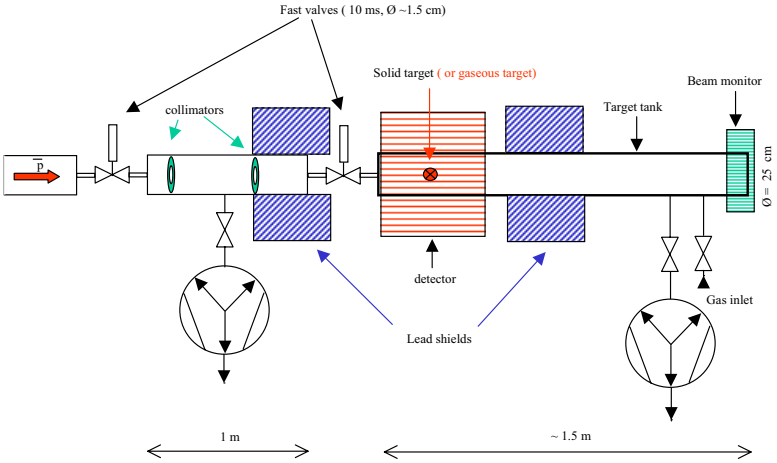

Figure 2.5: *Experimental set-up for* $E_k \lesssim 1.5$ *keV.*

heavy nuclei (like Xe) in H_2 or ^{4}He to optimize annihilation ratios in presence of much stronger Rutherford scattering processes.

Firstly, we will improve the number of the reconstructed events by shielding the detector from mesons originating from background annihilations on the end wall. After we will transfer downstream the detector to investigate the geometrical beam distribution from the vertices of $\bar{p}$-annihilations on the end wall for each sample target.

We will use fast valves and a suitable pumping system to assure differential pumping between the target and the MUSASHI high-vacuum (see Fig.2.5).

Thanks to the brilliant $\bar{p}$ beam from the MUSASHI-trap, atomic capture processes can be studied even at lower gas densities starting with the information on $\bar{p}$ stopping power in H_2, D_2, ^{4}He targets we gained from OBELIX at LEAR[102–104].

Part III

2006 Beamtime Plans

Assuming that AD will operate some 20+ weeks in 2006, we plan to allocate about 2/3 of the beamtime for the experiments discussed in Part I to take data and to produce immediate physics results. During the 18-month shutdown, many of the setups described in Part II and in Appendices B and D will be constructed, which will be commissioned using the remaining 1/3 of the beamtime.

Experiments discussed in Part I

Measurement	Number of weeks
Spectroscopy	
$\bar{p}$ He two-photon spectroscopy, $\bar{p}$ He ion (Part I, Sect. 1.1,1.2)	4
$\bar{p}$ He hyperfine splitting (Part I, Sect. 1.3)	4
Atomic collision	
Ionization cross section (Part I, Sect. 2.3)	4
$\bar{p}$ A (Sec. 2.2)	3
Subtotal	15

Experiments discussed in Part II

Nuclear cross section (5 MeV beam: Part II, Sect. 2.2.1)	2
Antihydrogen GS-HFS (Part II, Sect. 1.1)	
Paul trap commissioning	2
Cusp trap commissioning	2
Subtotal	6

Total	21

From 2007 onward, as Paul and cusp traps become better tuned, we will allocate more weeks for antihydrogen GS-HFS experiments, gradually phasing out the antiprotonic helium spectroscopy and atomic collision experiments described in Part I.

Part IV

Appendix - Detailed technical descriptions

A. Antihydrogen GSHFS measurement – strategy overview

A.1 Essential characteristics of formed antihydrogen

Possible ways to form antihydrogen atoms from trapped antiprotons and positrons will described in the next sections. It is common to all scenarios that the atoms are no longer confined by the magnetic or RF fields and can thus escape from the formation region in all directions. Recently cold antihydrogen atoms have been produced by ATHENA [105] and ATRAP [106, 107] using nested Penning traps initially proposed by Gabrielse et al. [108]. The formed $\overline{\mathrm{H}}$ atoms are commonly believed to have temperatures of 4.2 or 15 K, resp., corresponding to the cryogenic environment in which they are produced. First measurements of the velocity distribution of ATRAP, however, seem to indicate that much larger velocities might be present [109]. Further development will be needed to reduce the temperature of formed $\overline{\mathrm{H}}$ atoms, which seems feasible using the radiofrequency Paul trap system described in section B. Nevertheless, for the initial stage, a measurement system capable of using antihydrogen atoms of temperature up to 100 K seems necessary.

For the measurement of the ground-state hyperfine splitting frequency ν_{HF} as well as $\nu_{1\mathrm{S}-2\mathrm{S}}$ it is necessary to form antihydrogen atoms in the ground state. ATRAP reported mostly Rydberg-antihydrogen [106], while ATHENA has only inconclusive information obtained by measuring the temperature dependence of the $\overline{\mathrm{H}}$ formation rate [110]. It is therefore probably necessary to enhance the ground-state fraction by using laser stimulated recombination [111, 112], for which access for laser beams to the formation region has to be foreseen in the experimental layout.

The double sextupole structure needed for the measurement with $\overline{\mathrm{H}}$'s produced in cusp traps or Paul traps typically has a solid angle of $\sim 5 \times 10^{-5} - 10^{-4}$. Assuming that the recently reported production rates can be scaled by the factor 100 higher antiproton trapping efficiency of the ASACUSA RFQD and catching trap, and that both the temperature can be reduced and the ground-state fraction of formed antihydrogen can be increased, one can expect an event rate at the $\overline{\mathrm{H}}$ detector of about one event per minute during the mixing cycles, enough to make one scan per day. With further improvements of the production process, a high-statistics determination of the resonance shape will be possible.

A.2 Velocity distribution of antihydrogen atoms in the beam

$\overline{\mathrm{H}}$ atoms leaving the formation region move almost freely. The kinetic energy and direction may depend on the condition of recombination, but at the present stage these are not well known.

For the present purpose we assume that the produced antihydrogen atoms follow a Maxwell distribution at the trap temperature T and distribute isotropically. The distribution is given by

$$\Delta N/N = \frac{4}{\pi}\, v'^2\, e^{-v'^2}\, \Delta v', \tag{A.1}$$

with $v' = v/v_{\mathrm{m}}$ and $v_{\mathrm{m}} = \sqrt{2kT/m}$. $\Delta N/N$ is the relative number of atoms in the velocity interval between v' and $v' + \Delta v'$. v_{m} is the most probable velocity, T the temperature of the

atom cloud and m the mass of an antihydrogen atom. Typical Maxwell distributions and mean velocities are given in Fig. A.1.

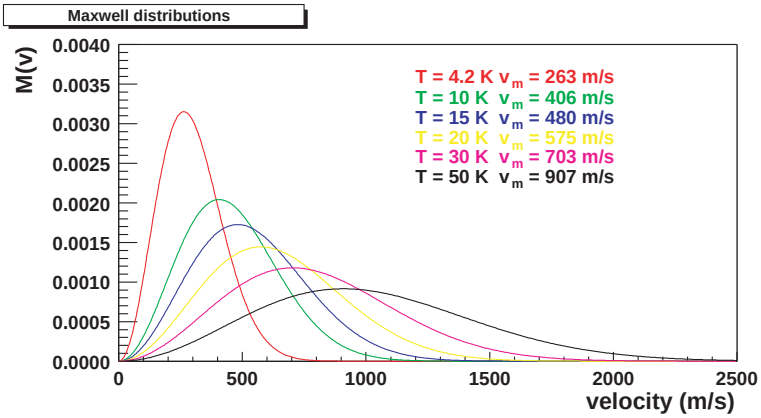

Figure A.1: *Maxwellian velocity distribution for various temperatures of the produced antihydrogen.*

A.3 Antihydrogen beam transport in sextupole fields

The magnetic energy of a hydrogen atom of magnetic moment $\vec{\mu}$ in a magnetic field $\vec{B}(\vec{r})$ is

$$V_{mag} = -\vec{\mu} \cdot \vec{B}. \tag{A.2}$$

Thus, the neutral atom feels a force

$$\vec{F} = -\text{grad}\, V = \text{grad}\, (\vec{\mu} \cdot \vec{B}). \tag{A.3}$$

If a moving antihydrogen atom experiences changes of the magnetic field $\vec{B}$ that are slow compared to the Larmor frequency, its magnetic moment will adiabatically follow the magnetic field lines, keeping its projection onto them constant. The product $\vec{\mu} \cdot \vec{B}$ will therefore only depend on the *magnitude* of $\vec{B}$ (provided $\vec{\mu}$ is constant), not on its direction.

Sextupole magnets are commonly used to focus neutral atoms. A sextupole field is described by a scalar potential S with form (in cylindrical coordinates r, ϕ, z)

$$S(r, \phi) = C\, r^3\, \sin 3\phi \tag{A.4}$$

The magnetic field following from $\vec{B} = -\text{grad}\ S$ has the cylindrical coordinates $(3Cr^2 \sin 3\phi,$ $3Cr^2 \cos 3\phi,\ 0)$. Its magnitude is then simply given by

$$B(r) = 3C\, r^2 = cr^2, \tag{A.5}$$

The magnetic field lines of a sextupole field are shown in Fig. A.2. They are produced by magnetic poles of alternating polarity shaped as equipotential surfaces of $S(r, \phi)$.

The bending force as defined in Eq. (A.3) becomes then

$$\vec{F} = \text{grad}\, (\vec{\mu} \cdot \vec{B}) = \text{grad}\, (\mu B(r)), \tag{A.6}$$

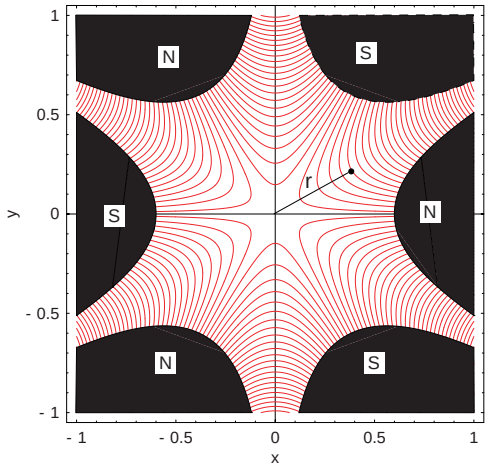

Figure A.2: *Magnetic field lines (red) of a sextupole magnet. The black parts are the magnet poles which follow an equipotential line. N = north pole, S = south pole.*

which has only a radial component

$$F_r = \mu \frac{\partial B}{\partial r} = 2c\mu r. \tag{A.7}$$

An antihydrogen atom moving in z direction (perpendicular to the plane shown in Fig A.2) with velocity v_z will undergo radial harmonic oscillations with frequency

$$\omega = \sqrt{\frac{2c\mu}{m}}, \tag{A.8}$$

Thus the focal length l_f of a sextupole is given by the flight time of an atom in z direction corresponding to half an oscillation period in radial direction

$$l_f = \frac{\pi}{\omega} v_z = \pi v_z \sqrt{\frac{m}{2c\mu}}. \tag{A.9}$$

The double field gradient c is practically limited by the strength of the magnetic field at the pole surface ($r = r_{\max}$), so that c is determined by $B(r_{\max}) = B_m = c r_{\max}^2$ or

$$c = B_m / r_{\max}^2. \tag{A.10}$$

The focal length as function of the three experimental parameters B_m, $r_{\max}$, and v_z then becomes

$$l_f = \pi v_z r_{\mathrm{m}} \sqrt{\frac{m}{2B_m\mu}}. \tag{A.11}$$

Fig. A.3 shows l_f for typical ranges of the three parameters. Assuming velocities of about 500 m/s corresponding to the mean velocity for a temperature of 15 K and $B_m = 1.2$ T (typical for iron magnets), maximum sextupole sizes will be 1.25 m length for a radius of 0.1 m, or 2.5 m for a radius of 0.2 m. In reality, however, the sextupole sizes can be shorter, because not the whole oscillation half period has to be inside the sextupole.

In recent years, atomic beam lines using sextupole magnets have been further developed for sources of polarized hydrogen using permanent magnets ($B_m = 1.65$ T [113]) or superconducting

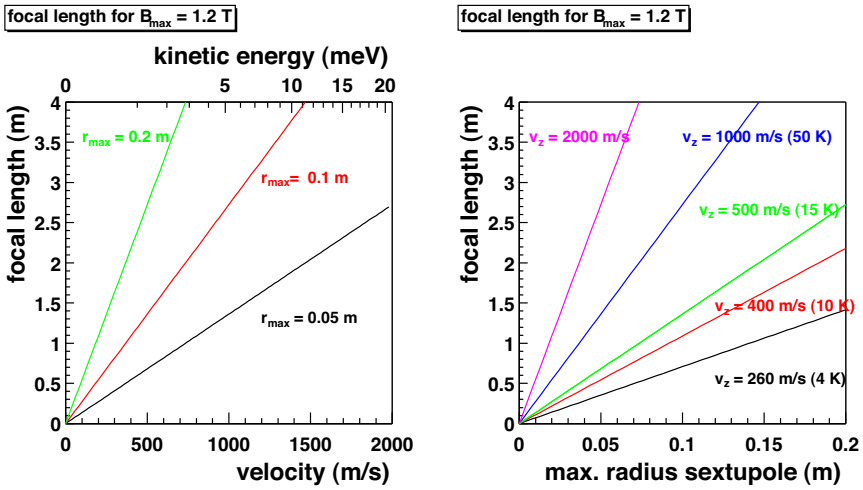

Figure A.3: *Dependence of the focal length of a sextupole on the atom velocity (left) and sextupole radius (right).*

ones ($B_m = 4$ T [114]). In our case, since the first sextupole is located rather far away from the $\overline{\mathrm{H}}$ source and covers a small solid angle, the increase in bending power leads only to a small increase in transmission. The choice of material for the sextupoles will therefore be made based on other considerations like easiness of operation etc.

A.4 Estimation of the event rate

In order to estimate the event rate, a Monte-Carlo program was used to simulate the antihydrogen trajectories through different experimental layouts. In the simulations, a point-like antihydrogen source of 50 K was assumed. Figure A.4 shows the trajectories of initially $(F, m) = (1, -1)$ (i.e. low-field seeking) antihydrogen atoms with two different configurations. The upper two subfigures represent a case when a small iris was inserted just before the microwave cavity, thereby allowing only "doubly focused" trajectories to pass through. The first subfigure shows the trajectories when the $\overline{\mathrm{H}}$ spin was not flipped (off resonance), while the second subfigure shows the trajectories when the $\overline{\mathrm{H}}$ spin was flipped (on resonance).

It is clearly seen that no atoms whose spin has been flipped in the cavity arrive at the antihydrogen detector, so that no background exists for the detection of $\overline{\mathrm{H}}$ atoms except of pions from $\overline{\mathrm{p}}$'s annihilating inside the sextupoles. They can be eliminating by proper shielding. The optimization of the shielding is straightforward and will be performed by GEANT simulations once a layout has been chosen.

For the shown configuration, the transmission ϵ is $\sim 2 \times 10^{-4}$, i.e. of all formed antihydrogen atoms of the $(F, m) = (1, -1)$ state, the fraction ϵ reaches the $\overline{\mathrm{H}}$ detector. Since the background is very low, and antihydrogen annihilation can easily be detected with 100% efficiency, there is no loss in the detection process. Out of all states formed, the low-field seekers constitute only 50%. Furthermore, due to aberrations we may lose another estimated factor 2–4, so that off resonance we expect fractions between 2.5×10^{-5} and 1×10^{-4} of the atoms to arrive at the $\overline{\mathrm{H}}$ detector. Taking the observed production rate of ATHENA and scaling it with the factor 100 more efficient trapping demonstrated by ASACUSA using our RFQD, we can expect a

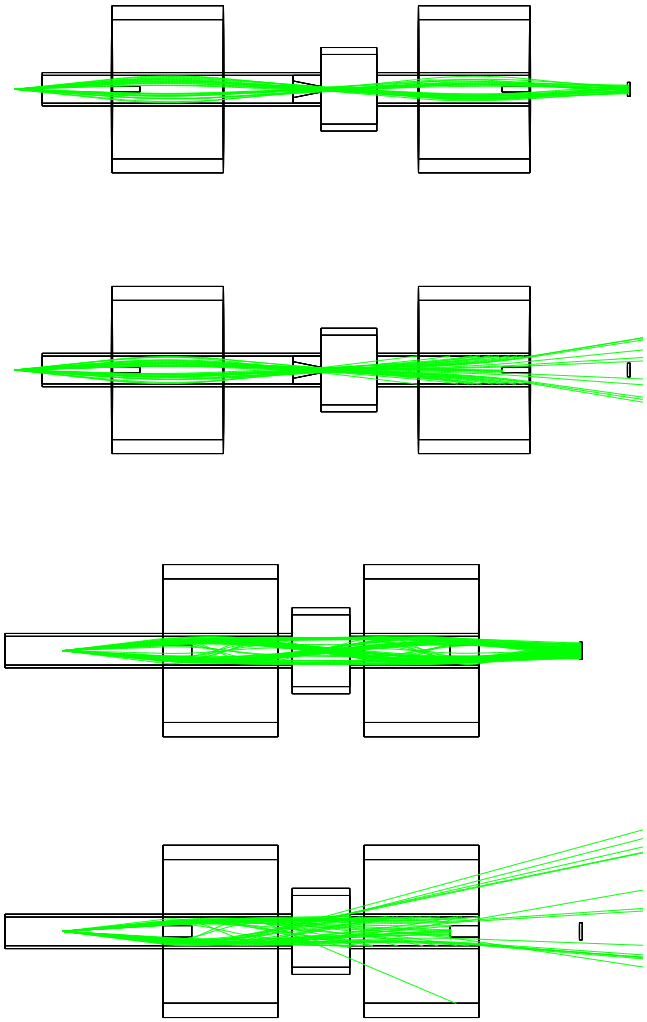

Figure A.4: *Trajectories of antihydrogen atoms through different sextupole layouts. Upper two: double focusing, off resonance (no spin flipping) and on resonance (spin flipped); lower two: single focusing, off and on resonance. The internal diameter of the beam pipe is 10 cm.*

production rate of $\sim 200\ \overline{\mathrm{H}}$/s, yielding a count rate on resonance of about 0.2 – 1 events/minute. If, instead of the assumed 50 K, the temperature of the $\overline{\mathrm{H}}$ source is e.g. 150 K and the magnetic field strength cannot be changed, then the transmission efficiency decreases only by a factor 2-3.

The lower two subfigures of Fig. A.4 show a layout in which the iris was removed and the two sextupoles were placed closer to each other. This way, also "singly focused" atoms can reach the detector. This increases the transmission efficiency to $\sim 4 \times 10^{-4}$ by allowing antihydrogen atoms in a wider velocity range to pass through. However, this might increase the Doppler broadening of the resonance peak.

Figure A.5: *12.9 GHz cavity used by ASACUSA to measure the hyperfine structure of antiprotonic helium. It has an inner diameter of 28.8 mm, and uses meshes on both top and bottom of the cylinder to let antiprotons and laser beams pass. The microwave radiation is provided by a rectangular wave guide from top, and the magnetic field strength in the cavity is monitored by a pick-up antenna attached below.*

A.5 Microwave resonance apparatus

A microwave cavity for 1.42 GHz has typically the dimensions of the corresponding wavelength of 21 cm, and has openings for the antihydrogen atoms to enter and leave. A possible solution is a scaled copy of the 12.9 GHz cavity used by our group to measure the hyperfine splitting of antiprotonic helium at the AD [17, 115]. It is a cylindrical cavity oscillating in the TM_{110} mode and would be placed with the cylinder axis parallel to the sextupole axis. Thus the magnetic field strength is independent of the z direction. The 12.9 GHz cavity has two meshes with a transmission of 80% on top and bottom of the cylinder which cover about half of the opening area, and still reaches Q-factors of several 1000. For a resonance frequency of 1.42 GHz, the dimensions would be about 25 cm in diameter and a length of 22 cm, which would nicely fit in the space between the two sextupoles.

In order to avoid unwanted Majorana spin-flips in the otherwise field-free region between the two sextupoles, a weak ($\sim$ 0.1 Gauss) homogeneous magnetic field can be applied in this region, which includes the microwave cavity as well. Even though such a static field changes the transition frequencies [see Eq. (1.15)], the shifts can be easily calculated and the measured frequencies can be corrected.

A.6 Resonance line shape and achievable resolution

The microwave field will induce transitions between 2 of the hyperfine states of the atom. The transition probability P_{12} between two stable levels 1, 2 of an atom which spends a time T inside an oscillating magnetic field $B(t) = B_0 e^{-i\omega t}$ can be easily calculated from the time dependent

Schrödinger equation and is given in many textbooks [116] as

$$P_{12} = \frac{4b^2}{4b^2 + (\omega - \omega_0)^2} \sin^2 \left[\frac{1}{2} \sqrt{4b^2 + (\omega - \omega_0)^2}\, T \right] \tag{A.12}$$

with $\hbar\omega_0 = E_2 - E_1$ being the energy difference between the two states and b the transition amplitude which depends on the strength of the oscillating magnetic field B_0 and the transition dipole moment. The probability has a maximum for $bT = \pi/2$, which defines the relation between the cavity length $L = v_z T$ and B_0. Since the only observable transitions are those flipping the positron spin, the transition dipole moment is of the order of a Bohr magneton. Then, in the case of $v_z \sim 500$ m/s and $L \sim 20$ cm, a magnetic field amplitude of $B_0 \sim 5 \times 10^{-4}$ Gauss is needed.

For a given velocity, the width of $P_{12}(\nu)$ is given by $\delta\nu = 0.799/T$, which for the above parameters yields $\delta\nu = 2.2$ kHz and $\delta\nu/\nu_{\mathrm{HF}} = 1.6 \times 10^{-6}$. The Monte-Carlo simulations for the double focusing experimental layout show (e.g. Fig. A.6) that the velocity distribution after the double solenoid is rather narrow (FWHM ~ 25 m/s for $v = 350$ m/s), so that the final resonance line width will not be significantly broadened. With good enough statistics, the center of the resonance line can easily be determined with a relative precision of 10^{-6} or better.

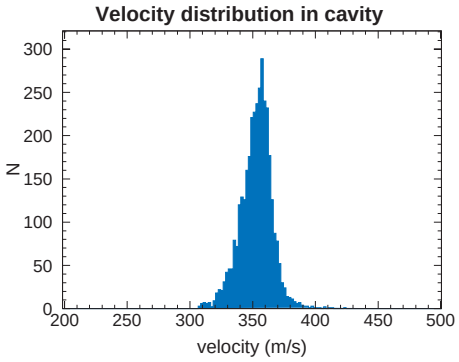

Figure A.6: *Velocity distribution inside the microwave cavity for those* $\overline{\mathrm{H}}$ *atoms which were detected after the second sextupole.*

A.7 Antihydrogen detection

When antihydrogen atoms collide with matter, the annihilation of both antiproton and positron can be used to uniquely identify $\overline{\mathrm{H}}$ atoms. As shown in the following section on the production methods, the double sextupole structure is only transparent to $\overline{\mathrm{H}}$ atoms in the desired spin states. All other $\overline{\mathrm{H}}$ atoms will annihilate around the formation region or inside the sextupoles, and by applying proper shielding, the annihilation products can be kept from reaching the antihydrogen detector region. This way, a detection efficiency of 100% for antihydrogen atoms can be easily obtained without serious background.

B. Antihydrogen production in a two-tone radiofrequency Paul trap

A new method for producing cold antihydrogen atoms occupying the 1s ground state using radiofrequency Paul traps is proposed and theoretically described. It involves first capturing keV-scale antiprotons in a superconducting linear radiofrequency Paul trap, cooling them to sub-eV temperatures by resonant resistive cooling, and compressing them into a dense cloud of diameter $d < 1$ mm. The cold antiprotons are transferred to a superconducting hyperbolic Paul trap and allowed to interact with positrons, the two particle species being simultaneously confined by radiofrequency fields applied in the MHz and GHz regions. The positrons are cooled by resistive and radiative cooling in the trap, the antiprotons by colliding with the positrons; those having the lowest energies fall into a sub-millimeter-sized region at the trap center, where electric and magnetic fields are negligibly small. A high-power laser beam at wavelength $\lambda = 11$ μm is focused into the central region, inducing radiative recombination and formation of antihydrogen in the $n = 11$ state; a second laser at wavelength $\lambda = 377$ nm (or 866 nm) induces further transitions to the $3d$ (or $2p$) state. These atoms quickly deexcite to the ground state, and can emerge from the trap through several openings between the trap electrodes. Only ground-state atoms are emitted, as those in the higher-lying states are ionized by the strong radiofrequency fields near the edges of the trap; antiprotons and positrons emerging from the ionization are recaptured by the trap, cooled, and recycled to form antihydrogen again. The fact that antihydrogen production occurs in a very small region at zero magnetic field is advantageous for carrying out any high-precision spectroscopy experiments.

B.1 Introduction

Antihydrogen atoms have recently been produced using Penning traps with magnetic fields of a few tesla [105, 106]. We here propose a method of producing cold antihydrogen in the 1s ground state by simultaneously confining antiprotons and positrons in a radiofrequency Paul trap [117]. The method has the following advantages enabling high-precision laser and microwave spectroscopy experiments,

1. *point-like antihydrogen source*, radiofrequency fields cause positrons and antiprotons with the lowest energies to fall into a millimeter-sized region at the trap center. This point-like region can be easily irradiated by strongly-focused laser beams, thereby achieving the high photon densities needed to efficiently induce radiative recombination and formation of antihydrogen, and deexcitation to its ground state,

2. *Zero magnetic field*, these antihydrogen atoms are unperturbed by the Zeeman effect as they are produced in a zero magnetic field,

3. *Extraction of antihydrogen*, the antihydrogen are emitted from the trap through numerous openings between its electrodes, and can be used to carry out in-flight antihydrogen

experiments,

4. *Selectivity of the 1s state, and antiproton/positron recycling*, only ground-state antihydrogen are emitted, as atoms in the higher-lying states are ionized by the strong RF fields near the edges of the trap; antiprotons and positrons emerging from the ionization are recaptured by the trap, cooled, and recycled to form antihydrogen again,

5. *Compact design*, the trap is relatively small ($\sim$ 20 cm diam) as it requires no superconducting magnet.

The present report is organized in the following way. The basic principals of Paul traps is described in Section B.2, the general layout of the experiment in Section B.3. The superconducting linear Paul trap used to trap keV-scale antiprotons and cool them to sub-eV temperatures is described in Section B.4. Finally, the two-tone superconducting hyperbolic Paul trap used to produce antihydrogen is described in Section B.5.

B.2 General principles of Paul traps

A Paul trap commonly consists of three electrodes: two end-cap electrodes which are hyperboloids of revolution around the z-axis and complementary to a ring electrode, which also has a hyperbolic cross-section with the dimensional constraint $r_0^2 = 2z_0^2$ [117–121]. Radiofrequency fields denoted by $(-U + V\cos\omega t)/2$ and $(U - V\cos\omega t)/2$ are applied to the end-cap and ring electrodes, respectively, the maximum DC and RF potentials denoted by U and V. The potential in the trap is given by

$$\theta = (U - V\cos\omega t)\,\frac{x^2 + y^2 - 2z^2}{4z_0^2} = (U - V\cos\omega t)\,\frac{x^2 + y^2 - 2z^2}{2r_0^2}. \tag{B.1}$$

The motions of charged particles with mass m and charge e in the field follow the Mathieu equations and are stably trapped only if the values of the constants of motion,

$$q = \frac{8eV}{m(r_0^2 + 2z_0^2)\omega^2}, \qquad a = \frac{-16eU}{m(r_0^2 + 2z_0^2)\omega^2}. \tag{B.2}$$

are within the shaded area shown in the "stability diagram" of Fig. B.1. The particle motions can be roughly separated into two parts: the secular oscillations occurring in the z- and $r-$ directions at low frequencies,

$$\omega_r = \sqrt{\frac{e^2V^2}{2m^2r^4\omega^2} + \frac{eU}{mr_0^2}}, \qquad \omega_z = \sqrt{\frac{2e^2V^2}{m^2z^4\omega^2} - \frac{2eU}{mz_0^2}} \tag{B.3}$$

and having large amplitudes, and the micromotion occurring at the RF drive frequency ω and having a small amplitude. The total energy of the particle is given by

$$E_{\rm tot} = \frac{m\omega_r^2 r_{\rm max}^2}{2} + \frac{m\omega_z^2 z_{\rm max}^2}{2} \tag{B.4}$$

wherein the maximum excursion of the particle (i.e. the "size" of the particle orbit) from the trap center is denoted by $z_{\rm max}$ and $r_{\rm max}$. This energy tends to zero for cold particles confined in the center of the trap where the radiofrequency fields are zero. The pseudo-potential Θ (the

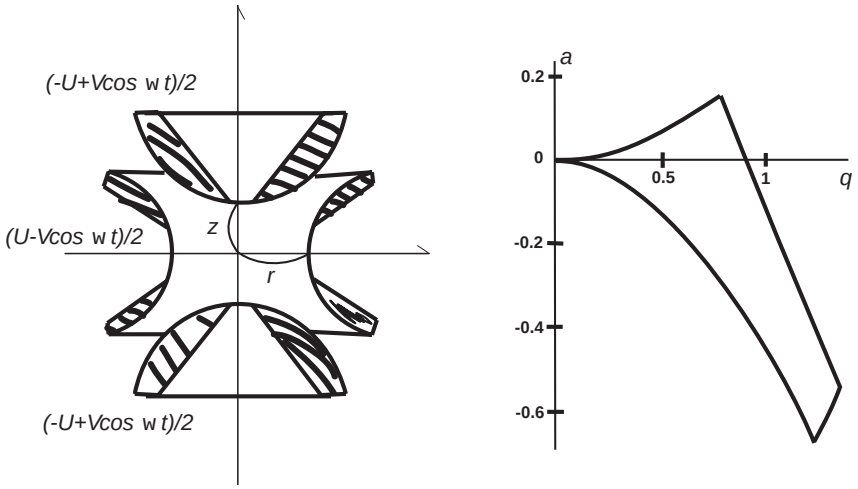

Figure B.1: *Stability diagram of a three-dimensional radiofrequency Paul trap.*

"depth" of the trap equal to the highest kinetic energy of the particles that can be confined) is given by

$$\Theta_{\rm r} = \frac{m\omega_r^2 r_0^2}{2}, \qquad \Theta_{\rm z} = \frac{m\omega_z^2 z_0^2}{2}. \tag{B.5}$$

We next consider the confinement of N particles in the above Paul trap. In the equilibrium state, the particle distribution exactly neutralizes the trap pseudopotential, such that a cloud of uniform charge density Q and ion density n_0 with radius $R_{\rm cloud}$, given by

$$Q = \frac{m\varepsilon_0(2\omega_r^2+\omega_z^2)}{e},\ n_0 = \frac{m\varepsilon_0(2\omega_r^2+\omega_z^2)}{e^2},\ R_{\rm cloud} = \left(\frac{3Ne^2}{4\pi m\varepsilon_0(2\omega_r^2+\omega_z^2)}\right)^{1/3} \tag{B.6}$$

is formed. According to Eq. B.3, the surface of the cloud is heated by the radiofrequency to a temperature

$$T = \frac{1}{k_B}\left(\frac{9meN^2(2\omega_r^2+\omega_z^2)}{128\pi^2}\right)^{1/3} \tag{B.7}$$

which increases with the number of trapped particles N. At low particle temperatures, the radiofrequency field penetrates and heats only a thin skin on the outside of the cloud with a thickness equal to the Debye length

$$\lambda = \sqrt{\frac{k_B T}{m(2\omega_r^2+\omega_z^2)}}. \tag{B.8}$$

The particles in the interior of the cloud are heated by making elastic collisions with the outer-lying particles.

The particles can be cooled [118, 122–124] by introducing between the endcap electrodes of the trap a shunt impedance consisting of an inductor L and capacitor C (this includes the ~ 100 pF capacitance of the electrodes themselves), its LC resonant frequency tuned to the secular frequency ω_z. This causes the small current induced between the two electrodes by the oscillatory motion of the particle to be dissipated in the LC circuit having an effective impedance,

$$R_z = \frac{Q_z}{\omega_z C}, \tag{B.9}$$

where Q_z is the quality factor of the resonant circuit. The typical time constant of this 'resistive cooling' is to the first approximation, irrespective of the number of particles confined, and has been experimentally and theoretically verified to be about

$$\tau_{\rm cool} = g\frac{4mz_0^2}{e^2R_z} \tag{B.10}$$

where g is a geometric factor equal to about $\sim$ 1.3 in the hyperbolic trap above. Effective impedances of around $R \sim 1$ MΩ are needed to cool particles within a short interval $\tau_{\rm cool} \sim 1$ s. In past experiments, some 10^4 protons have been confined in a hyperbolic Paul trap and cooled from T=3000 K to 900 K [118] using this technique.

The above considerations show that when designing a Paul trap to confine positrons and antiprotons with the lowest possible energy ($T < 100$ K),

1. the gradient of the radiofrequency field should be small enough to avoid radiofrequency heating,

2. large traps (i.e. $z >> R_{\rm cloud}$) are needed to provide the high pseudopotentials which would stably confine many particles over long periods of time,

3. large traps require the application of correspondingly large radiofrequency power. On the other hand, high power dissipation in the trap electrodes would lead to deterioration of the vacuum in the trap due to outgasing. Both the dissipation and outgasing can be minimized by using cryogenic superconducting structures,

4. a tuned LC circuit with high Q-values provided by superconducting elements is needed to cool the particles quickly.

B.3 General layout of the experimental apparatus and methods

In Fig. B.2, a plan view of the proposed experimental layout is shown, while a detailed cross-sectional view of the antihydrogen source is shown in Fig. B.3. The setup consists of

1. the radiofrequency quadrupole decelerator (RFQD) currently installed in the ASACUSA beamline, which will be used to decelerate the 5.3-MeV antiprotons provided by AD to energies $E < 100$ keV,

2. a superconducting linear Paul trap used to capture the above antiprotons and cool them to sub-eV energies, and compress them into a cloud of diameter $d < 1$ mm,

3. a commercial positron accumulator, which provides 25-ns-long pulsed beams containing $\sim 10^8$ positrons of diameter $d < 1$ mm and temperature $T << 1$ eV (see Section D),

4. a novel two-tone superconducting hyperbolic Paul trap, used to simultaneously confine positrons and antiprotons, cool them, and produce antihydrogen,

5. CW laser beams of wavelength $\lambda = 11$ μm and 377 nm, used to induce radiative recombination of positrons and antiprotons, and deexcitation to the ground state of antihydrogen. The major part of the required laser systems and diagnostic tools already exist in the ASACUSA laser hut,

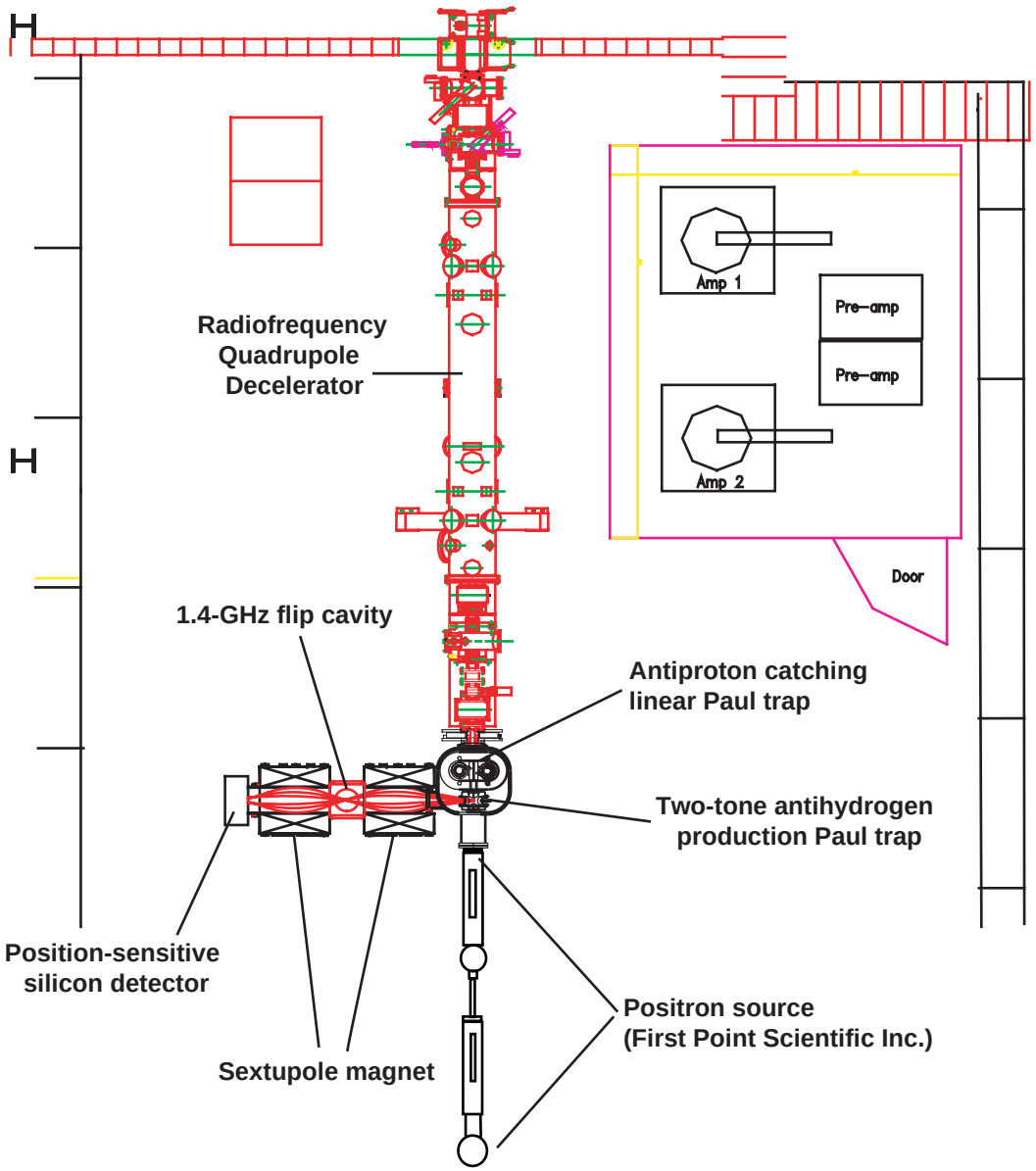

Figure B.2: *Top view of proposed antihydrogen experiment, including spectrometer for HFS spectroscopy.*

6. calorimetric detectors, c.f. lead tungsten scintillators read out by photomultipliers, used to detect the annihilation of antiprotons and positrons with a large solid angle, but with limited spatial resolution and no vertex reconstruction capabilities,

7. two sextupole magnets and radiofrequency cavities comprising an atomic beam line, used for GS-HFS measurements of antihydrogen atoms emitted from the Paul trap.

All the Paul traps will be placed in a common ultra-high vacuum chamber, and cryogenically cooled to $T = 1.6$–4.2 K to reach a residual pressure of $P < 10^{-13}$ mb corresponding to an antiproton lifetime $\tau = 1$ hour against annihilation on residual gas molecules. Similar vacuum and

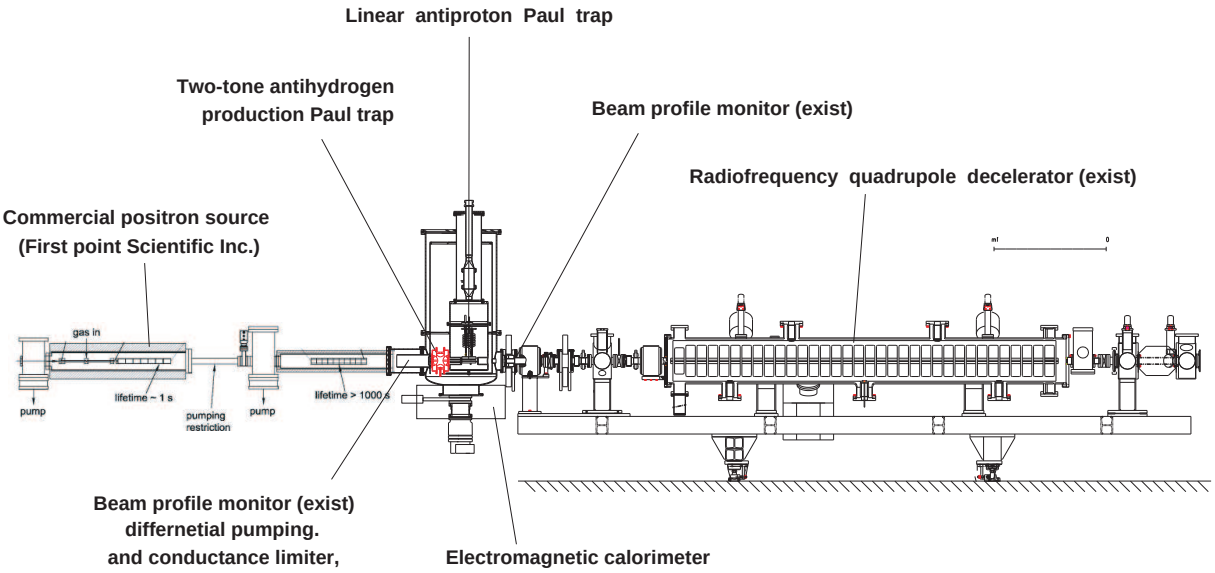

Figure B.3: *Cross-sectional view of the antiproton, positron, and antihydrogen recombination traps.*

cryogenic requirements [125] have already been achieved at the AD by the ATRAP, ATHENA, and ASACUSA experiments. The traps will be constructed out of niobium and will be operated in the superconducting mode in order to sustain the large radiofrequency fields needed to confine the antiprotons and positrons with minimal power dissipation.

Simulations and experiments show that the particle temperature is strongly dependent on the strength of the RF field, and the number of particles in the trap [126–128]. We intend to decrease the temperature of the antiprotons to $T < 100$ K first by using a Paul trap with a larger volume and smaller RF field than those previously used to trap protons, and second by increasing the resistive cooling rate by several orders of magnitude [129], with high-Q superconducing LC circuits.

B.4 Superconducting linear Paul trap for antiprotons

In this section, we describe the linear Paul trap used for cooling and compressing the antiproton cloud. As already demonstrated in ASACUSA's previous experiments [6], we propose to decelerate pulsed beams containing 2×10^7 antiprotons with energy $T = 5.3$ MeV to $T \sim 100$ keV using the RFQD. The beam emitted from the RFQD has an energy spread $\Delta T \sim 10$ keV, angular divergence $\theta = 30°$, and pulse-length $\Delta t \sim 200$ ns. The antiprotons will be focused using two solenoid magnets into a 10-mm-diam beam spot on the surface of a 1.0-micron-thick Mylar foil, and those emitted from the other side are captured by a linear Paul trap. Similar traps and RFQ's have been used for many years in radioactive beam facilities at CERN, GSI [130], GANIL, KEK, NSCL, and other places to capture high-energy ions and cool them. The spatial beam profile will be measured by a secondary electron microwire profile monitor [131], while the time profile and intensity will be measured by Lucite Cherenkov counters [132]. The transverse and longitudinal energy distributions of the antiprotons after traversing the foil, estimated using a Monte Carlo simulation, are shown in Fig. B.4. About 70% of the antiprotons annihilate in the foil, whereas 30% are emitted with longitudinal and transverse energies $E = 0$–10 keV and

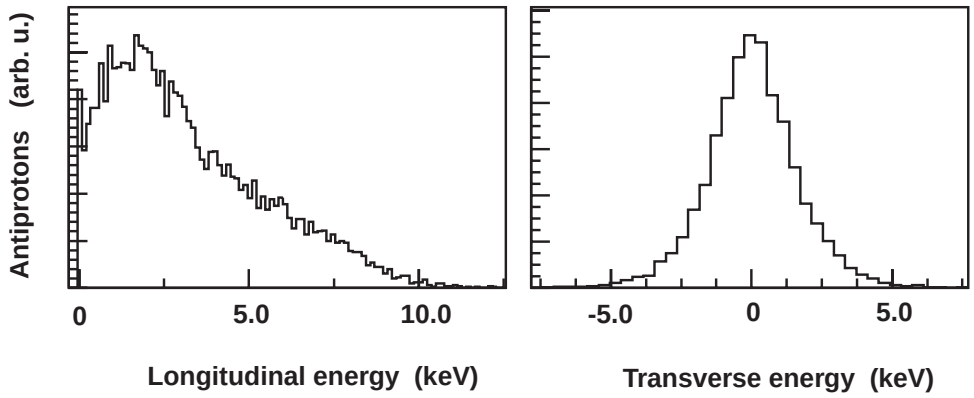

Figure B.4: *Longitudinal (left) and transverse (right) energy distributions of the antiprotons emitted from the deceleration Mylar foil.*

Table B.1: *Various possible combinations of the operational parameters of the linear Paul trap for antiprotons.*

Drive ω (MHz)	Voltage (kV)	q	Secular freq. ω_r (MHz)	Potential Θ (kV)	Captured $\overline{p}$ per AD pulse
40	**50**	**0.67**	**9.5**	**4.2**	1.7×10^6
40	**60**	**0.81**	**11.4**	**6.1**	1.8×10^6
45	60	0.64	10.2	4.8	1.7×10^6
50	60	0.52	9.2	3.9	1.6×10^6

0–5 keV. This simulation included the theoretical emittances of the beam entering the foil derived from beam-dynamics simulations of the RFQD, the multiple scattering effect according to the Moliere distribution, and the energy straggling effect according to the Vavilov distribution. Experimental data of the energy loss and straggling (which depends on the average energy lost by the antiproton per atomic collision) at such low-energy regions are not available, and were approximated using a crude extrapolation. These calculations are thus questionable, but they do agree qualitatively with the results of previous laser spectroscopy experiments of $\overline{p}\mathrm{He}^+$ and Penning trap experiments using the RFQD and a similar Mylar foil, so the results are believed to be accurate within a factor 2–3. From the above beam dynamics considerations, the linear Paul trap requires an aperture $d_a \sim 30$ mm (defined by the beam diameter $d \sim 10$ mm), an electrode longitudinal length $l > 200$ mm (defined by the pulse length ~ 200 ns), and a pseudopotential defined by Eq. B.5 of a few keV to efficiently capture the antiprotons.

A three-dimensional computer model of the Paul trap is shown in Fig. B.6. It consists of four parallel rods of diameter $d_r = 40$ mm and length $l = 150$ mm, with a distance $2r = 30$ mm between the surfaces of the opposing rods. By negatively biasing the electrodes relative to ground, the antiprotons can be readily ejected with the corresponding longitudinal energy. Ring electrodes of thickness 15 mm and inner diameter $d = 20$ mm are placed 5 mm away from the two ends of the trap. Before antiproton injection, the downstream ring is biased at a DC voltage -5 kV, the upstream one at 0 kV. Immediately after the 200-ns-long antiproton pulse traverses the upstream ring, it is biased to -5 kV with a rise time ~ 200 ns, thereby longitudinally confining the antiprotons in the trap.

A beam dynamics simulation was made wherein a beam containing 6×10^6 antiprotons delivered from the RFQD entered the Mylar foil, and the antiprotons emitted from the foil having the longitudinal and transverse energy distributions shown in Fig. B.4 were allowed to enter the Paul trap. The trajectories of these antiprotons were tracked for 10^5 radiofrequency cycles (corresponding to $\sim$ 0.1 s), and the number $N_{\overline{p}}$ of antiprotons confined stably after this period was derived. In Table B.1, the q-value, secular frequency ω_r, and depth of the pseudopotential Θ of the linear Paul trap derived using the equations,

$$q = \frac{2eV}{m\omega^2 r_0^2}, \quad \omega_r = \frac{eV}{\sqrt{2}mr_0^2\omega}, \quad \Theta = \frac{m\omega_r^2 r_0^2}{2e} = \frac{q^2 m\omega^2 r_0^2}{16e} \tag{B.11}$$

and the simulated number of antiprotons $N_{\overline{p}}$ confined are shown for various combinations of the radiofrequency drive ω and voltage V.

In Table B.2, the full specifications of the trap chosen with a radiofrequency $\omega = 40$ MHz and voltage 60 kV (which implies a pseudopotential of 6 kV and accumulation rate 1.8×10^6 $\overline{p}$ per 100 s) are shown. The high radiofrequency amplitudes are attained by placing stems with an effective inductance $L_{\rm rf} = 310$ nH in parallel to the capacitance $C_{\rm elect} = 30$ pf of the four rod electrodes, such that a resonance with the drive frequency

$$\omega = \frac{1}{\sqrt{L_{\rm rf}\left(\frac{1+s}{1-s}\right)C_{\rm elec}}} = 2\pi 40 \text{ MHz}, \tag{B.12}$$

is attained. In the above equation, s is a parameter (near 0.25) caused by the coupling between neighboring inductor stems in the cavity. Larger RF voltages may increase the risk of multipactoring effects (wherein successive secondary electron emission from the electrodes lead to discharge). The particle density n_0, charge density Q, and cloud radius $r_{\rm cloud}$ in the equilibrium state were estimated using the equations,

$$n_0 = \frac{2\varepsilon_0 m\omega_r^2}{e^2}, \quad Q = -\frac{2\varepsilon_0 m\omega_r^2}{e}, \quad r_{\rm cloud} = \sqrt{\frac{N}{ln_0\pi}}. \tag{B.13}$$

The RF field causes heating in the transverse direction with a temperature $e\Theta(r_{\rm cloud})/k_B \sim 200$ K; the cloud diameter $2r_{\rm cloud} \sim 40$ μm is thus slightly larger than the Debye length $\lambda_D \sim 15$ μm.

The transverse motions of the trapped antiprotons are resistively cooled by introducing a capacitor $C_{\rm sec}$ between a pair of opposing electrode rods, so that the LC-circuit comprised by it and the above-mentioned inductor $L_{\rm rf}$ is in resonance with the secular frequency ω_r,

$$\omega_r = \frac{1}{\sqrt{L_{\rm rf}\left(\frac{1-s}{1+s}\right)C_{\rm sec}}} = 2\pi 11.4 \text{ MHz}. \tag{B.14}$$

The coupling parameter s enters in the above equation with an opposite sign compared to that of Eq. B.12 because of the different polarities of the radiofrequency current flowing through the inductors for the quadrupole resonance ω compared to the dipole one ω_r. The required capacitance can therefore be calculated,

$$C_{\rm sec} = C_{\rm elec}\left(\frac{\omega}{\omega_r}\frac{(1+s)}{(1-s)}\right)^2 \sim 1 \text{ nF} \tag{B.15}$$

Table B.2: *Chosen parameters of the linear Paul trap for antiprotons.*

Radiofrequency drive	40 MHz
Radiofrequency drive fluctuations	10 kHz
Maximum radiofrequency voltage between neighboring electrodes	60 kV
Voltage fluctuations (open loop)	60 V
Distance between opposite electrodes $2r_0$	30 mm
Electrode length l	150 mm
Electrode segment number	3
Electrode segment DC voltage	50 V
Electrode capacitance C_{elec}	30 pF
Effective DC inductance of stem L_{rf}	320 nH
Dipole cooling capacitance C_{sec}	1.0 nF
Potential on ring electrodes on both ends	6000 V
Switch-on speed of ring electrodes	100–200 ns
Ring electrode inner diameter	20 mm
Distance from ring electrodes to rod electrodes	5 mm
q-value	0.81
Secular motion frequency ω_r	11.4 MHz
Pseudopotential depth	6.0 kV
Antiprotons trapped per AD shot	1.8×10^6
Antiproton density at equilibrium	4×10^6 mm^{-3}
Charge density at equilibrium	2×10^{15} C/m^3
Cloud diameter at equilibrium	~ 40 μm
RF-heating temperature at cloud surface	~ 200 K
Debye length λ_D at cloud surface	~ 15 μm
Q-value of resistive cooling circuit	10^6
Cooling time constant	~ 9 s
Cooling time from capture to equilibrium	100 s
Antiproton-antiproton collision rate	~ 1 MHz
Electrode temperature	1.6 K

The time constant of resistive cooling can then be calculated as,

$$\tau_{\mathrm{cool}} = g\frac{2mr_0^2}{e^2R_z} = g\frac{2mr_0^2\omega C_{\mathrm{sec}}}{e^2Q} = g\frac{2mr_0^2\omega^2(1+s)^2C_{\mathrm{elec}}}{e^2\omega_z(1-s)^2Q}, \tag{B.16}$$

which can be expressed using the q-parameter as,

$$\tau_{\mathrm{cool}} = g\frac{4\sqrt{2}mr_0^2\omega(1+s)^2C_{\mathrm{elec}}}{e^2q(1-s)^2Q} = \frac{8\sqrt{2me\Theta}r_0(1+s)^2C_{\mathrm{elec}}}{e^2q^2(1-s)^2Q}. \tag{B.17}$$

The above expression shows that in a linear Paul trap comprising a radiofrequency cavity wherein the electrode capacitance C_{elec} and dipole-cooling capacitance share a common inductor, the resistive cooling time tau_{cool} is proportional to C_{elec} and trap diameter r_0 (both of which are determined by the transverse and longitudinal sizes of the antiproton beam), the square root of the pseudopotential (defined by the energy distribution of the antiprotons), and the inverse of the quality factor Q. The characteristic cooling time of the antiprotons calculated from Eq. B.17 assuming a quality factor $Q \sim 10^6$, dipole capacitance $C = 1$ nF, and geometric

factor $g = 4$ is $\tau \sim 9$ s. It would thus take 100 s to cool the antiprotons from 1 keV to the equilibrium temperature $T = 200$ K and diameter $d = 40$ μm. Faster cooling can only be achieved by reducing the trap radius r or reducing the pseudopotential, thus sacrificing the number of trapped antiprotons per unit time.

The resistive cooling occurs in only one plane (i.e. the transverse plane x), but the motions in the other two planes y and z are also cooled by strong collisional coupling between the three motions; first, particles rebound at the two ends of the linear Paul trap occurring at a rate

$$\frac{c}{l}\sqrt{1 - \frac{mc^2}{mc^2 + k_B T}}, \tag{B.18}$$

i.e. 1–2 MHz at the initial temperature $T = 1$–4 keV. Second, at lower temperatures and higher particle densities, velocity-changing collisions occur at a rate

$$f = \frac{n_0 e^4 \log_e \Sigma}{4\pi\varepsilon_0^2 \sqrt{m}(k_B T)^{3/2}}, \tag{B.19}$$

wherein $\Sigma = 15$–20 is the ratio of the cut-off distance for the Coulomb interaction between two adjacent antiprotons to that of closest approach, which depends on the plasma conditions. At the equilibrium temperature $T = 200$ K, the collision rate is $f = 1$ MHz.

The above Eq. B.17 assumes that the distribution width $\Delta\omega_r$ of the antiproton secular frequency is small compared to the bandwidth ω_r/Q of the LC cooling circuit. In reality, however, when the hot antiproton cloud (temperature $T \sim 4$ keV) is initially captured, the frequencies of the particle motions show a relativistic second-order Doppler shift given by

$$\left(\frac{\Delta\omega_r}{\omega_r}\right)_{\text{hot}} = -\frac{3k_B T}{mc^2} \sim 10^{-6} - 10^{-5}. \tag{B.20}$$

At low temperatures and high charge densities, on the other hand, antiprotons displaced from the trap center by space-charge effects experience different amplitudes of RF heating, which leads to a spatially-dependent, second-order Doppler shift given by

$$\left(\frac{\Delta\omega_r}{\omega_r}\right)_{\text{cold}} = -\frac{e^2 N}{8\pi\varepsilon mc^2 l} \sim 10^{-12}. \tag{B.21}$$

In order to cool all antiprotons distributed within the bandwidth $\Delta\omega_r$, therefore, the Q-value of the LC circuit must be less than $(\omega_r/\Delta\omega_r)_{\text{hot}} = 10^5$–$10^6$ (even though superconducting cavities would easily achieve values of $Q > 10^7$).

Experiments using a room-temperature copper model have shown that the resonant frequency of the superconducting cavity can fluctuate by ~ 10 kHz due to microphonic disturbances. Moreover the radiofrequency voltage amplitude in an amplifier used in open loop can typically fluctuate by $\sim 10^{-3}$; these can cause slow time-dependent changes in the particle's ω_r-frequency of

$$(\Delta\omega_r)_{\text{fluct}} = \sqrt{\frac{\Delta V^2}{V^2} + \frac{\Delta\omega^2}{\omega^2}} \sim 10^{-3}. \tag{B.22}$$

A servo-lock system is needed on both the amplitude and frequency of the RF drive, so that the ω_r-value of the particles would coincide with the LC resonance frequency of the antiprotons with a precision 10^{-6}.

In Fig. B.5, a cross-section view of the superconducting linear Paul trap and cryogenic system are shown. The trap electrodes and radiofrequency stems are housed in a 400-mm-diam, 700-mm-high cylindrical cavity made of niobium. Three-dimensional computer simulations on the

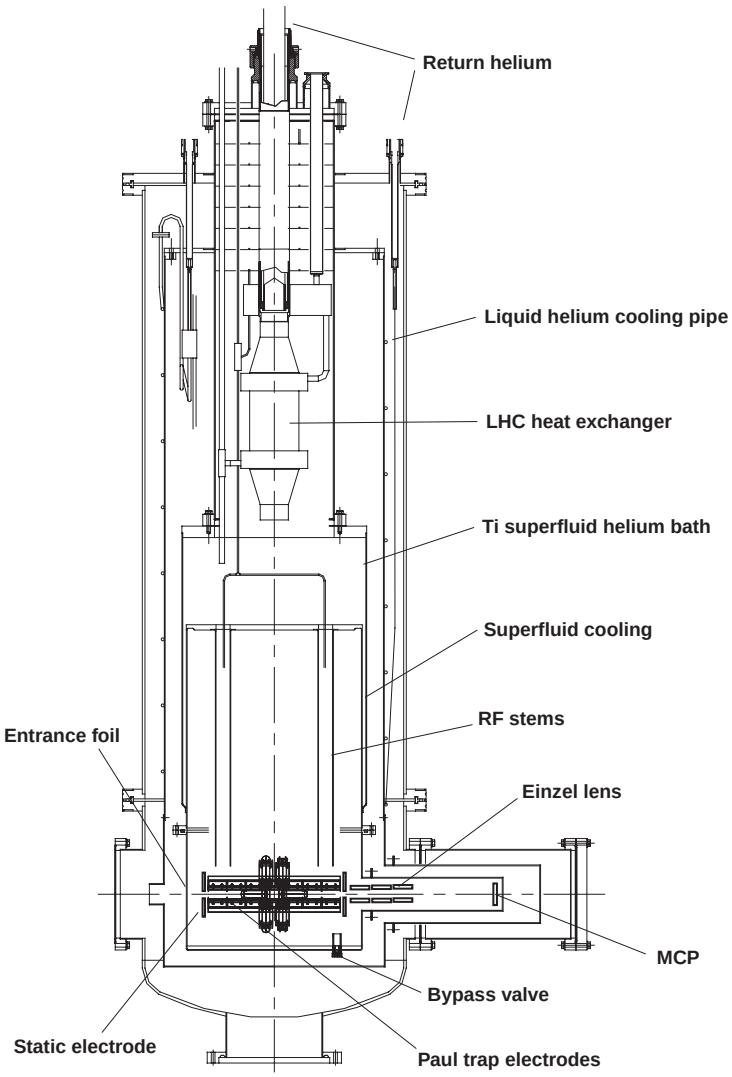

Figure B.5: *Cross-section view of the superconducting linear Paul trap and cryostat for antiproton capture and cooling.*

RF properties of the cavity show that the largest heat dissipation occurs on the top flange of the cavity (estimate ~ 1 W), and an additional few hundred milliwatts are dissipated on each of the four stems supporting the Paul trap. In order to maintain the temperature of these locations below the superconducting transition point, the cavity walls are directly cooled by superfluid helium housed in a titanium reservoir welded onto the outside of the cavity. Part of the superfluid helium is brought down from the reservoir through the hollow stems and allowed to flow through the Paul trap electrodes and cool them. Liquid helium is constantly filled into the reservoir (i.e. a "constant flow cryostat") from a nearby 500-liter-dewar, and cooled to superfluid temperatures by the pumping out of helium gas through a heat exchanger. A radiation shield is fixed to the outside of the cavity, and cooled by liquid helium flowing through pipes welded onto the shield surface.

The vacuum inside the cavity (maintained by cryogenic pumping at $T = 1.6$ K to a level $< 10^{-13}$ mb needed to attain an antiproton lifetime ~ 10 min) is separated from that of the

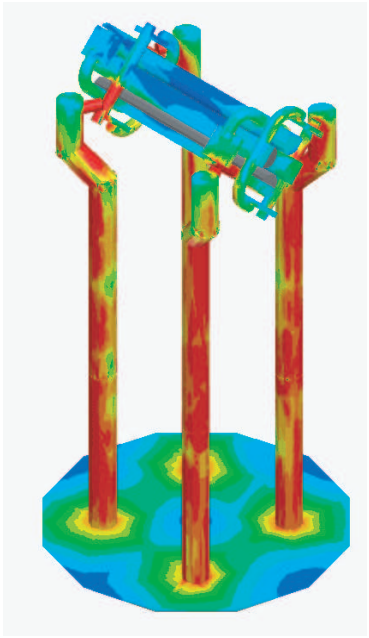

Figure B.6: *Simulated heat dissipation in the linear Paul trap. A few hundred milliwatts are dissipated in each of the four stems, the rest on the bottom plate.*

outer vacuum chamber connected to the RFQD (typical vacuum $\sim 10^{-8}$ mb) by a 1-μm thick mylar foil, which also acts as a degrader foil for the antiprotons. Similar foils have been used in laser spectroscopy experiments of antiprotonic helium, wherein a vacuum difference of 10^{-7} was attained between the two sides of the foil. When pumping down from atmospheric pressure, a bypass valve is opened at the bottom of the cavity which ensures that no pressure difference is exerted on the foil.

In the initial phase of experiments, trapping and cooling of protons in the trap will be tested using the duoplasmatron facility of CERN. Cooled protons are extracted from the trap through a series of Einzel lenses, which focus the beam onto the surface of a microchannel plate detector (maintained at room temperature). The secondary electrons are bombarded onto a phosphor screen, the image of which is captured by a CCD sensor, thus providing the diameter and intensity of the particle beam.

B.5 Two-tone Paul trap

A Paul trap with a 3-dimensional radiofrequency field can in principle simultaneously trap particles with opposite charges, as demonstrated by Schermann et al. [133] for large numbers (density $\rho \sim 10^7$ cm^{-3}) of Tl^+ and I^- ions. Simultaneous trapping of antiprotons and positrons, however, is difficult because of the large (factor ~ 1800) difference in their mass-to-charge ratios. Paul traps using a single radiofrequency drive can only trap particles with m/e-values and kinetic energy E simultaneously satisfying the two conditions,

$$\frac{m}{e} > \frac{8.8V}{m(r_0^2 + 2z_0^2)\omega^2}, \quad E < \frac{q^2 m \omega^2 r_0^2}{16e} \tag{B.23}$$

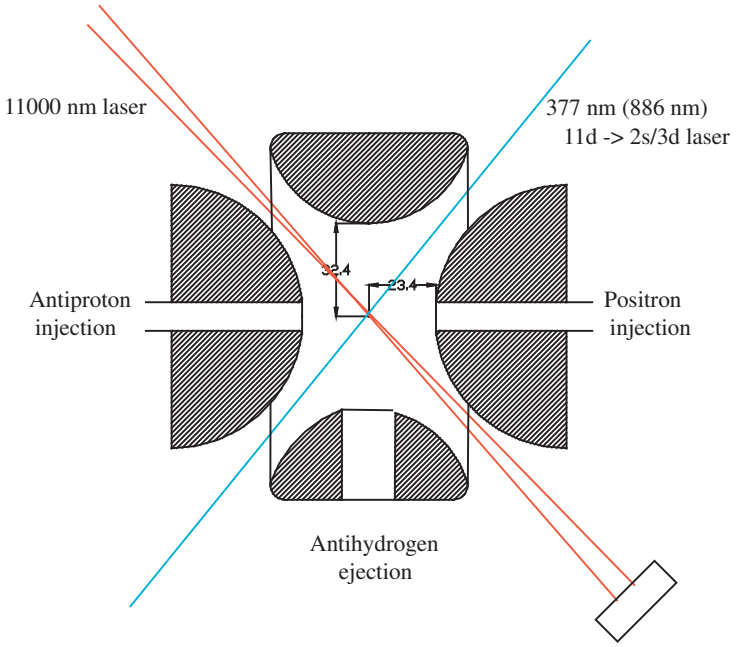

Figure B.7: *Cross-section view of two-tone Paul trap with various holes for antiproton/positron injection, antihydrogen ejection, and laser irradiation.*

This implies that the positrons require a very high radiofrequency drive ω for stable trapping, whereas the antiprotons require a large V-value as its pseudopotential Θ (scaling with m/e) is only 1/1800 as large as the positron's. The dilemma is that application of high radiofrequency amplitudes to trap the antiprotons would lead to excessive heating of the positron cloud and a decrease in the antihydrogen production rate.

We here solved this problem by applying two quadrupole radiofrequency fields (frequency ω_1 with amplitude V_1, and ω_2, V_2) of the form,

$$\theta = -\left(V_1 \cos\omega_1 t + V_2 \cos\omega_2 t\right) \frac{x^2+y^2-2z^2}{4z_0^2} \tag{B.24}$$

$$= -\left(V_1 \cos\omega_1 + V_2 \cos\omega_2 t\right) \frac{x^2+y^2-2z^2}{2r_0^2}. \tag{B.25}$$

to trap both antiprotons and positrons. The equations of motion for antiprotons and positrons can now be written,

$$\frac{d^2 r_{\overline{p}}}{dt^2} + \left(\frac{e}{m_{\overline{p}} r_0^2}\right)\left(U - V_1 \cos\omega_1 t - V_2 \cos\omega_2 t\right) r_{\overline{p}} = 0, \tag{B.26}$$

$$\frac{d^2 z_{\overline{p}}}{dt^2} - \left(\frac{2e}{m_{\overline{p}} r_0^2}\right)\left(U - V_1 \cos\omega_1 t - V_2 \cos\omega_2 t\right) z_{\overline{p}} = 0 \tag{B.27}$$

$$\frac{d^2 r_{e^+}}{dt^2} + \left(\frac{e}{m_{e^+} r_0^2}\right)\left(U - V_1 \cos\omega_1 t - V_2 \cos\omega_2 t\right) r_{e^+} = 0, \tag{B.28}$$

$$\frac{d^2 z_{e^+}}{dt^2} - \left(\frac{2e}{m_{e^+} r_0^2}\right)\left(U - V_1 \cos\omega_1 t - V_2 \cos\omega_2 t\right) z_{e^+} = 0 \tag{B.29}$$

Under the condition $U = 0$, $V_1 >> V_2$, and $\omega_1 >> \omega_2$, we can define the a and q parameters of motion for positrons as follows,

$$q_{e^+} = \frac{8eV}{m_{e^+}(r_0^2 + 2z_0^2)\omega_1^2}, \quad a_{e^+} = \frac{-16eV_2 \cos\omega_2 t}{m_{e^+}(r_0^2 + 2z_0^2)\omega_1^2}, \tag{B.30}$$

and analyze the positron trajectories by considering V_1 as the main radiofrequency amplitude and V_2 as a small-amplitude, slowly-changing perturbation on the end-cap electrodes. The secular motion frequencies for positrons can thus be written,

$$\omega_{re^+} = \sqrt{\frac{e^2V_1^2}{2m_{e^+}^2 r_0^4 \omega_1^2} + \frac{eV_2 \cos\omega_2 t}{m_{e^+} r_0^2}}, \quad \omega_{ze^+} = \sqrt{\frac{2e^2V_1^2}{m_{e^+}^2 r_0^4 \omega_1^2} - \frac{2eV_2 \cos\omega_2 t}{m_{e^+} r_0^2}}. \tag{B.31}$$

which is a good approximation under the condition,

$$\frac{eV_1^2}{2m_{e^+} r_0^2 \omega_1^2} >> V_2 \tag{B.32}$$

i.e. the a-value, ω_{re^+} and ω_{ze^+} make slow, small-amplitude oscillations around $a = 0$, $eV_1/\sqrt{2}m_{e^+}r_0^2\omega_1$, and $\sqrt{2}eV_1/m_{e^+}r_0^2\omega_1$. The pseudopotentials in the two planes can be written,

$$\Theta_{\mathrm{re^+}} = \frac{m_{e^+}\omega_{re^+}^2 r_0^2}{2e} = \frac{eV_1^2}{4m_{e^+}r_0^2\omega_1^2} + \frac{V_2 \cos\omega_2 t}{2} \tag{B.33}$$

$$\Theta_{\mathrm{ze^+}} = \frac{m_{e^+}\omega_{ze^+}^2 z_0^2}{2e} = \frac{eV_1^2}{m_{e^+}r_0^2\omega_1^2} - V_2 \cos\omega_2 t. \tag{B.34}$$

The ω_2-radiofrequency acts as a small destabilizing force, but is overwhelmed by the stronger stabilizing force exerted by the ω_1-frequency. Stable trapping is achieved when

1. the q_{e^+}-value is smaller than ~ 0.9,
2. the amplitude of the a-value $-16qV_2/m(r_0^2 + 2z_0^2)\omega_1^2$, remains inside the stability region,
3. the initial kinetic energy of the positrons (injected into the trap at typically ~ 1 eV in the z-direction) are smaller than the pseudopotentials defined in Eq. B.34.

The above perturbative treatment does not apply in the antiproton case because its larger mass results in the conditions,

$$\frac{eV_1^2}{2m_{\overline{p}}r_0^2\omega_1^2} < V_2, \qquad \frac{eV_2^2}{2m_{\overline{p}}r_0^2\omega_2^2} < V_1. \tag{B.35}$$

and so its trajectory is actually quite complicated, being equally influenced by both radiofrequencies. Unlike the positron case, however, both ω_1 and ω_2 frequencies act as confining forces (the former determining the short-term confinement, the latter the long-term one), and so the antiproton may be considered as traveling in a superposition of two pseudopotentials produced by the two frequencies,

$$\Theta_{\mathrm{r\overline{p}}} = \frac{m_{\overline{p}}(\omega_{r1\overline{p}}^2 + \omega_{r2\overline{p}}^2)r_0^2}{2e}, \qquad \Theta_{\mathrm{z\overline{p}}} = \frac{m_{\overline{p}}(\omega_{z1\overline{p}}^2 + \omega_{z2\overline{p}}^2)z_0^2}{2e}. \tag{B.36}$$

Table B.3: *Chosen parameters of the hyperbolic Paul trap for antihydrogen production.*

Dimension r_0	32.5 mm
Dimension z_0	23 mm
Radiofrequency drive ω_1	3 GHz
Radiofrequency amplitude V_1	80 kV
Radiofrequency drive ω_2	1 MHz
Radiofrequency amplitude V_2	40 V
Positron q-value	0.15
Positron oscillatory a-value	-1.7×10^{-4}–1.7×10^{-4}
Positron oscillatory pseudopotential	2100–2200 V
Positron radial secular motion ω_{re^+}	(78.0 ± 0.4) MHz
Positron axial secular motion ω_{ze^+}	(156.0 ± 0.5) MHz
Number of positrons trapped	10^4
Positron density at equilibrium	5×10^5 mm^{-3}
Positron charge density at equilibrium	7×10^{-5} C/m^3
Positron cloud diameter at equilibrium	350 μm
Temperature at positron cloud surface (no cooling)	400 K
Antiproton q_1-value	8×10^{-5}
Antiproton q_2-value	0.37
Antiproton pseudopotential due to ω_1	1.2 V
Antiproton pseudopotential due to ω_2	3 V
Number of antiprotons trapped	10^4
Antiproton density at equilibrium	7×10^2 mm^{-3}
Antiproton charge density at equilibrium	1.2×10^{-7} C/m^3
Antiproton cloud diameter at equilibrium	3 mm
Temperature at antiproton cloud surface (no cooling)	50 K
Dipole cooling capacitance $C_{\rm sec}$	70 pF
Superconducting cooling inductor L	15 nF
Switch-on speed of V_1 and V_2	several 10 ns
Debye length λ_D at cloud surface	~ 15 μm
Q-value of resistive cooling circuit	10^4
Cooling time constant	~ 1 s
Positron-positron collision rate	~ 1 MHz
Antiproton-positron collision rate	~ 1 kHz
Total antiproton-positron collision rate	~ 10 MHz
Electrode temperature	1.6 K

wherein the four secular frequencies $\omega_{r1\overline{p}}$, $\omega_{r2\overline{p}}$, $\omega_{z1\overline{p}}$, and $\omega_{z2\overline{p}}$ are defined as

$$\omega_{r1\overline{p}} = \frac{eV_1}{2m_{\overline{p}}^2 r_0^2 \omega_1^2}, \quad \omega_{r2\overline{p}} = \frac{2eV_2}{m_{\overline{p}}^2 r_0^2 \omega_2^2}, \quad \omega_{z1\overline{p}} = \frac{eV_1}{2m_{\overline{p}}^2 r_0^2 \omega_1^2}, \quad \omega_{z2\overline{p}} = \frac{2eV_2}{m_{\overline{p}}^2 r_0^2 \omega_2^2} \tag{B.37}$$

In Fig. B.7, the cross-section view of the superconducting Paul trap for antihydrogen production is shown, having dimensions $r_0 = 32.5$ mm and $z_0 = 23$ mm with a hyperbolic shape $r_0^2 = 2z_0^2$. The large electrode size (~ 10 times greater than those typically used in Paul traps) is needed to attain a combination of high pseudopotential and low radiofrequency heating. The parameters of the Paul trap are tabulated in Table. B.3; we apply a radiofrequency drive of $\omega_1 = 3$ GHz and $V_1 = 80$ kV to trap the positrons, and $\omega_2 = 1$ MHz and $V_2 = 40$ V to trap the

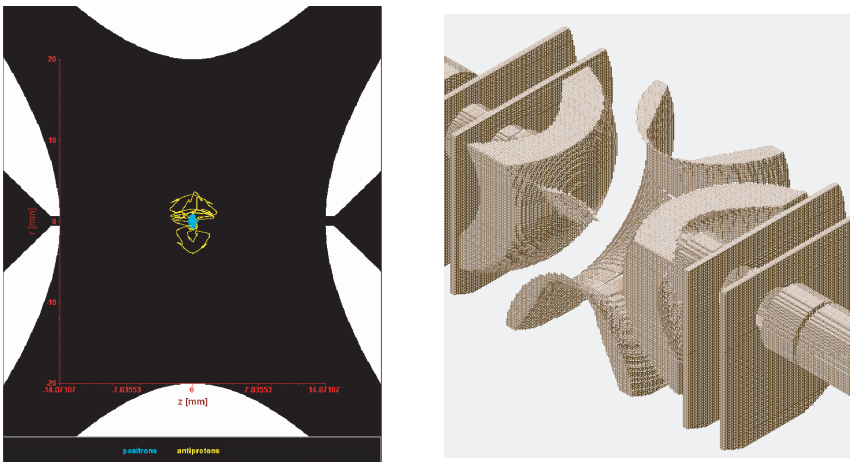

Figure B.8: *Simulation result of* 10^4 *antiprotons and positrons simultaneously confined in the two-tone Paul trap.*

antiprotons. The q-value of the positron due to the ω_1 frequency is 0.15, whereas the a-value oscillates between $\pm 1.7 \times 10^{-4}$ due to the application of ω_2. The pseudopotential of the positrons thus oscillates between 2100 and 2200 V, the radial and axial secular motions between 77.6–78.4 MHz and 155.5–156.5 MHz, respectively. When 10^4 positrons are confined and the equilibrium between the space-charge effect and the pseudopotential is reached, we obtain a positron density $n_{e^+} = 5 \times 10^5$ mm^{-3} and cloud diameter $d_{e^+} = 350$ μm, its surface heated to $T_{e^+} = 400$ K by the radiofrequency field.

In the antiproton case, the ω_1 and ω_2 frequencies produce q-values of 8×10^{-5} and 0.37, respectively, and pseudopotentials of 1.2 V and 3 V. For 10^4 antiprotons, a density 700 mm^{-3} is reached, with a relatively large cloud diameter ~ 3 mm. The surface of the antiproton cloud is quite cold ~ 50 K, which would allow the production of cold antihydrogen.

In order to check the validity of the above calculations, we performed Monte-Carlo simulations of the particle trajectories using two different computer codes; the Ion Trajectory Simulation (ITSIM) program developed exclusively for Paul trap design, and Simulation Package (SIMION) version 7.0 which is a general particle-tracking program. A three-dimensional representation of the above hyperbolic Paul trap was generated, and the relevant radiofrequencies applied. The two programs differ in the way the particle trajectories are integrated (ITSIM has static integration times, whereas SIMION has an algorithm that adjust automatically the integration time at each step), and the way particle-particle collisions are handled (ITSIM uses Langevin collision models, SIMION a statistical Monte-Carlo method). In Fig. B.8, the result of 10^4 confined antiprotons and positrons tracked for 10^7 ω_1 radiofrequency cycles (~ 3 ms) is shown. Both simulations derived positron-cloud diameters of 200–500 μm and antiproton cloud-diameters 2–3 mm with temperatures $T \sim 100$ K, in essential agreement with the above analytical results.

Resistive cooling will be carried out by introducing a superconducting inductor $L = 15$ nF between the two end-cap electrodes, thus comprising a LC circuit together with the electrode capacitance $C_{\rm elec} \sim 70$ pF in resonance with the 156-MHz axial secular motion of the positrons. A Q-value of 10^4 would correspond to a fast cooling time of 1 s. The 3-GHz micromotion of the positrons also causes radiative energy loss, which occurs with a typical time constant ~ 10–100 s. A given positron collides with another positron at a rate ~ 1 MHz, and with an antiproton

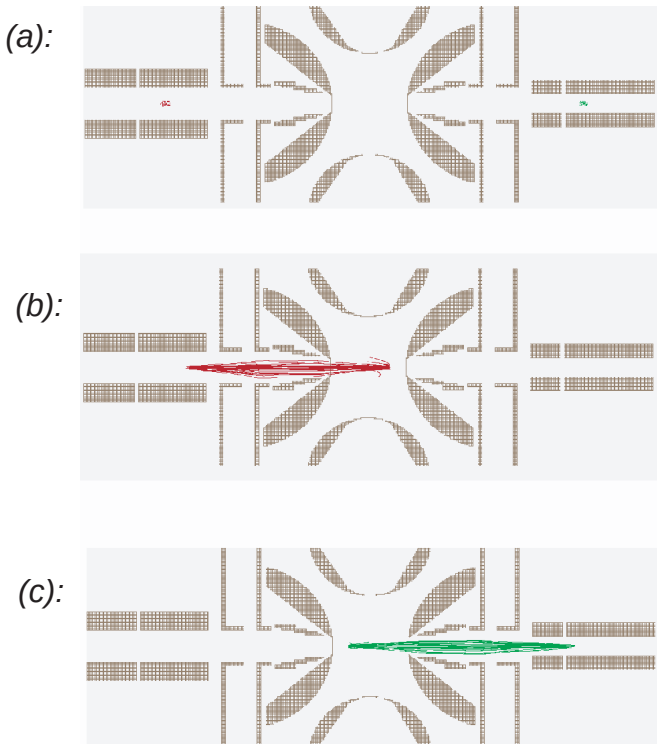

Figure B.9: *Simulated antiproton (red) and positron (green) clouds before injection (a). Antiproton injection into the Paul trap (b). Positron injection (c).*

at a rate 1 kHz; in this way, the kinetic energy in all three planes of motion in both particles are cooled.

In Fig. B.9, the result of a particle-tracking simulation wherein antiprotons (shown in red) are transported from the linear Paul trap to the hyperbolic one is shown. The electrodes of the linear Paul trap will be floated to 1 V, thus ejecting the antiprotons which have an initial diameter of 0.1 mm and transverse energy spread of $\sim$ 400 K. Several Einzel lenses focus the beam through a small hole in the end-cap electrode. Once the antiprotons are inside the trap, the end-caps can be slightly biased ($\sim$ 1 V) and the radiofrequency turned on, thereby capturing the antiprotons. These simulations show that this transport efficiency is about $\sim$ 30%. Transport of the positrons is more technically difficult; both the RF field of 80 kV and DC bias of the end-cap electrodes must be switched on with a rise-time of a few ten nanoseconds. The positron cloud must be strongly compressed both transversely (less than 1 mm) and longitudinally (less than 10 mm). However since the accumulation rate of the positrons from the ^{22}Na source is very high (10^8/s), the transport efficiency is allowed to be quite low ($< 10^{-2}$).

B.6 Antihydrogen production in 1S-state

As described above, the Paul trap confines 10^4 positrons and antiprotons at temperature $T \sim$ 100 K. The high positron temperature implies that antihydrogen production will proceed via

spontaneous radiative recombination, the rate of which is given by [111],

$$\sigma = 3.2 \times 10^{-11}\mathrm{cm}^3/\mathrm{s} \times \sqrt{\frac{1\mathrm{meV}}{kT}} \left[1 + \frac{-0.5\ln(\frac{kT}{1\mathrm{meV}})}{5.2}\right] n_{e^+} \sim 0.02 \text{ Hz}, \tag{B.38}$$

wherein the positron density is estimated to be $n_{e^+} = 5 \times 10^8$ cm^{-3}. The total production rate is given by integrating over the entire spatial overlap between the antiproton and positron clouds, i.e. over the 350 μm-diam sphere:

$$\int \sigma n_{e^+} n_{\overline{p}} d^3r = 2\mathrm{Hz}. \tag{B.39}$$

Two laser beams will be used to further increase the production rate, one at wavelength $\lambda = 11.1$ μm inducing radiative recombination into the antihydrogen 11d state, the second at $\lambda = 377$ nm deexciting it to the $2p$ state. The theoretical gain factor for this stimulated recombination can be calculated,

$$G = \frac{0.86 \times 10^{-9}\mathrm{eVs} \cdot 2(2l+1)}{\tau kT[5.2 - 0.5\ln(kT/1\mathrm{meV})]} \tag{B.40}$$

wherein τ is the effective lifetime of the daughter state. At temperature $T \sim 100$ K we obtain a factor $G \sim 70$, which implies an antihydrogen production rate of ~ 100 Hz.

These gain factors will be achieved using

1. A $^{13}C^{16}O_2$ laser beam with wavelength $\lambda = 11.1$ μm and power $P = 50$ W. A system of mirrors arranged in a multi-pass orientation will focus the beam to a power density ~ 100 kW/cm^3 at the 0.3-mm-diam interaction region where antihydrogen is produced,

2. A 10-W Nd:YAG laser will be used to pump a titanium-sapphire laser, thereby producing a laser beam of power $P = 1.5$ W and wavelength $\lambda = 754$ nm. Using a LBO crystal the laser will be frequency-doubled to wavelength $\lambda = 377$ nm with a conversion efficiency around $(20 - 30)\%$. This laser system already exists in the ASACUSA experimental area.

Neutral antihydrogen dissipate and leave the trap through holes cut in the trap electrodes with a solid angle of $5\% \times 4\pi$, and are transmitted to the ground-state HFS sextupole beamline. Spontaneous radiative recombination causes about $\sim 40\%$ of the antihydrogen to be produced in the $n \leq 4$ states, while laser stimulated recombination drives nearly all of them into the 2p state. The cascade time (the time required until all of the antihydrogen deexcites to the ground state) is shown in Fig. B.10; it increases quickly with n, reaching ~ 100 μs for $n = 15$. The time-of-flight between antihydrogen production and emission from the 70-mm-diam trap is 50, 40 and 30 μs for atom temperatures 50, 100, and 300 K. This implies that all antihydrogen atoms produced in the $n \leq 13$ states with temperature $T \sim 50$ K will deexcite to the 1S or 2S states before leaving the trap.

In Fig. B.11 (left), the electric field gradient needed to ionize an antihydrogen occupying a state with principal quantum number n is shown. The 3-GHz RF field reaches a maximum value 20 kV/cm at the edges of the trap, which corresponds to $n > 13$ states being ionized. In Fig. B.11 (right), the minimum n-value of the state ionized by the RF field is shown as a function of the distance from the trap center. States with $n > 20$ (i.e. those made by 3-body recombination) are ionized within a 1-cm-diam region at the trap center. Thus we conclude that the trap has the following characteristics favourable for spectroscopy of antihydrogen atoms,

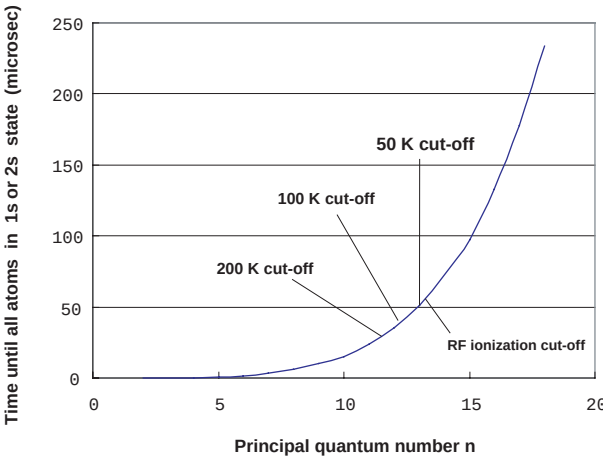

Figure B.10: *Cascade time until nearly all of the antihydrogen are in the 1S or 2S states. All antihydrogen produced with a principal quantum number $n \leq 13$ and temperature $T = 50$ K will deexcite to the 1S or 2S states before being emitted from the trap. The corresponding cut-off points $n \leq 12$ for temperatures $T = 100$ and 200 K are shown. States above $n > 14$ are ionized by the radiofrequency field.*

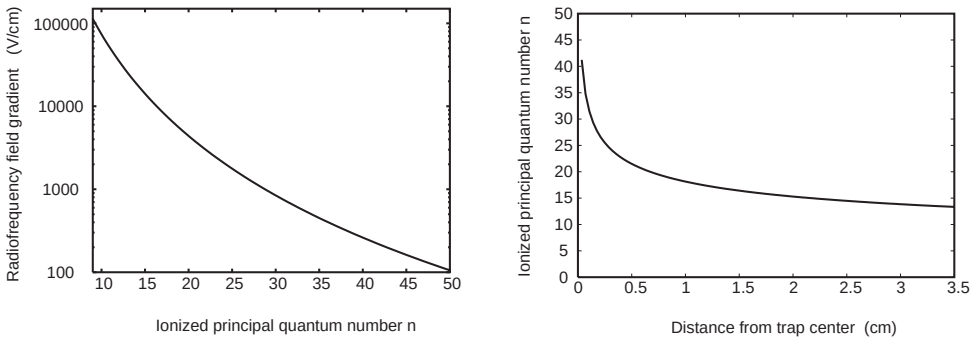

Figure B.11: *Radiofrequency field gradient versus the minimum principal quantum number n that is ionized (left). The minimum n-value ionized as a function of the distance from the center of the hyperbolic Paul trap.*

1. Antihydrogen atoms emitted from the Paul trap are all in either the 1S or 2S states,
2. Antihydrogen in the high-n states are ionized by the RF field, and the emerging antiprotons and positrons are recaptured by the trap and used to make antihydrogen again.

B.6.1 Antihydrogen detector systems and beam monitors, data acquisition

The present experiment will use simple detector systems:

1. Secondary electron emission microwire chambers to detect the beam profiles of the antiproton and positron beams during injection and transport between the traps,

2. Acrylic Cherenkov counters [132] to detect the intensity and time profile of the incoming antiproton beam,

3. Electromagnetic calorimeters consisting of seven layers of scintillators and lead plates, read out by 2-inch photomultipliers. These will measure the annihilation of antiprotons or anihydrogen atoms on an event-by-event basis, by detecting the charged pions emerging from the annihilation.

The detectors will be read out by CAMAC- and SCXI-based data acquisition systems, each equipped with an embedded microprocessor and connected to an external workstation via ethernet network.

B.6.2 Feasibility tests to be done at CERN and their requirements

The basic design for the two Paul traps already exists, and their radiofrequency properties have been extensively tested using room-temperature copper models. The superconducting linear Paul trap for antiproton capture and cooling will be completed by end of 2005. All aspects of their operation, particularly the resistive cooling, will then be tested and optimized using a proton beam of energy E = 60-100 keV provided by the CERN duoplasmatron ion source located in Bat. 152. The diameter and approximate temperature of the proton cloud in the trap will be measured by extracting it onto a microchannel plate detector located 30 cm away from the trap. The first trapping and cooling of antiprotons will be carried out during a few weeks of beamtime in 2006.

A cryogenic design of the antihydrogen recombination trap will be produced by fall of 2005, the design being modified depending on the results of the above test of the linear Paul trap. The final apparatus with two Paul traps occupying a common cryostat will be pertaining completed by end of 2006, with tests using the antiproton beam scheduled for 2007.

With the latter proviso concerning manpower and materials, we also request occasional technical assistance and advice from the CERN cryogenics laboratory, and consultations with CERN experts on superconducting cavities. We will also need to be able to use some CERN workshop and laboratory facilities in manufacturing some of the technically difficult parts of the RF Paul traps, particularly those pretaining to superconducting cavities.

C. Production of a spin-polarized $\bar{H}$ beam with a cusp trap

The key objective for either laser or microwave spectroscopy of antihydrogen atoms is to prepare an adequate number of them in the 1S ground state at low temperature and to confine these in a neutral atom trap. The principal mechanisms for antihydrogen atom synthesis are three body recombination processes in a high density, low temperature plasma. This inevitably results in the high-Rydberg state atoms which are not suitable for spectroscopic purposes. In the present section, a cusp trap scheme is proposed in which these antihydrogen Rydberg states may not only be synthesized at low temperatures but also trapped at for a time long enough to allow most of them to cascade down to the ground state for subsequent use in a variety of experiments. The cusp trap consists of a magnetic quadrupole (cusp) field formed by a pair of superconducting solenoids together with an electrostatic octupole [134]. The operation principle of this field configuration is described below.

Figure C.1 shows an overview of the experimental setup used for the 1S ground state hyperfine splitting measurements with the cusp trap scheme. The central part is schematically shown in fig. C.2, which consists of the cusp trap for synthesizing a beam of 1S antihydrogen atoms in low-field seeking (LS) states, a microwave cavity for inducing spin flip transitions to high-field seeking (HS) states, a sextupole lens which focusses LS- but de-focuses HS-states emerging from the cavity and an antihydrogen detector. The upper right corner of fig.C.2 shows schematically the expected antihydrogen count rate on the detector as the RF cavity frequency passes through the hyperfine transition frequency. The depth of the resonance is primarily determined by contamination from excited-state antihydrogen atoms.

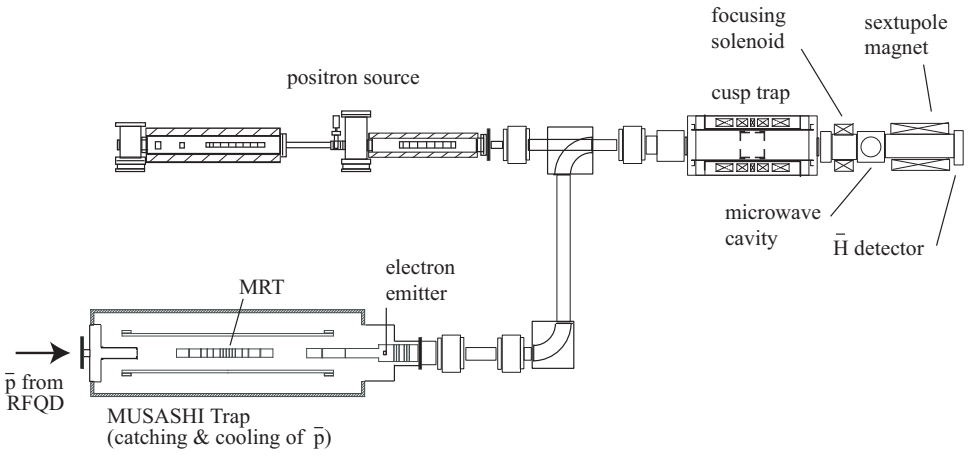

Figure C.1: *An overview of the experimental setup of the cusp trap scheme. The main components of the setup are the MUSASHI trap for catching and cooling of antiprotons from the RFQD, the positron source see Sect. D), the cusp trap, the microwave cavity, the sextupole magnet, and the antihydrogen atom detector.*

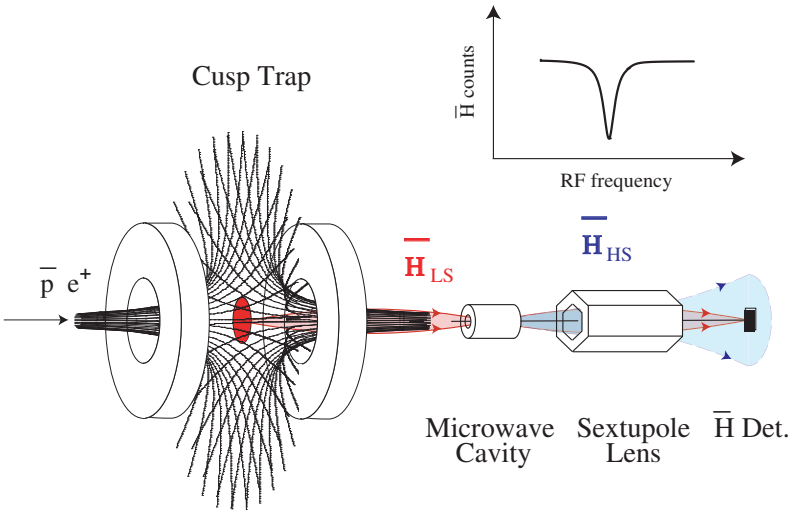

Figure C.2: *A schematic layout of the cusp trap configuration (left) together with a microwave cavity and a sextupole lens for hyperfine transition measurements of antihydrogen atoms.*

C.1 Positron Confinement

As is schematically shown in fig.C.1, the positron source and the cusp trap are configured on the same axis, and the positrons are transferred from the positron source. The cusp magnetic field configuration (see fig.C.3(a)) can stably confine a neutral plasma [135] although charged particles still escape along the magnetic-field lines. In the case of a non-neutral plasma, this leakage can be " plugged "by applying an electric octupole field, as illustrated in fig. C.3(b), where C_u, C_m and C_d are upstream, middle and downstream cylindrical electrodes, respectively, and D_u and D_d are upstream and downstream disk-shaped electrodes. The present scheme therefore possesses advantageous plasma stabilization properties in addition to simply confining the non-neutral plasma. Prototype experiments have already demonstrated electron plasma confinement, with confinement time proportional to the square of the magnetic field strength, and with a plasma density distribution that is nearly parabolic in the central region [29] [136]. The electron plasma lifetime in the cusp trap magnetic field of $\sim$ 1T has also been proved to be much longer than is required for the proposed hyperfine structure experiment. Such a high magnetic field is essential not only to realize a long trapping time but also to cool electrons via synchrotron radiation. We can safely assume that a sample of positrons can be stored in a similar manner.

The positron distribution along the magnetic field line is determined by the balance of the three forces, the space charge of positrons, the electric octupole field, and the magnetic force $-|\vec{\mu}_l|\nabla|\vec{B}|$, where $\vec{\mu}_l$ is the orbital magnetic moment of the positrons. Positrons in the cusp trap move back and forth along the magnetic field lines, and thus interact with each other and reach local equilibrium over a region determined by the balance among the three forces. This is in a sense similar to the familiar case of non-neutral plasma in a uniform magnetic field. Because the magnetic field (zero at the center of the cusp trap) increases monotonically in all directions away from the center up to several Tesla (see discussion below), off-centre positrons cool quickly via synchrotron radiation. This eventually causes sympathetic cooling of positrons on the same field line.

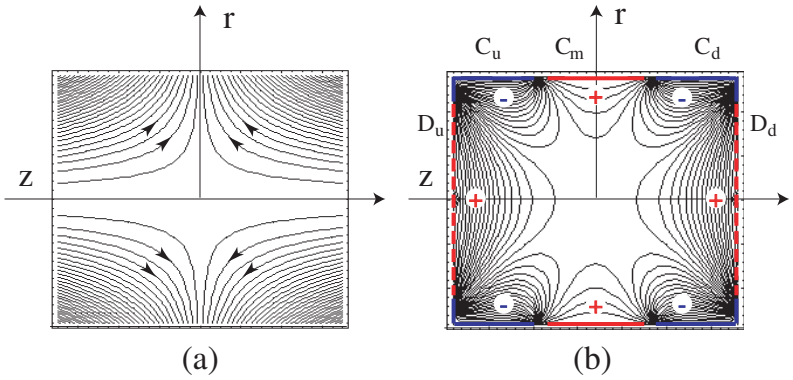

Figure C.3: *(a)Magnetic field lines of the cusp field. (b) Equipotential surfaces of the octupole field. For confining positrons, electrodes D_u, C_m, and D_d (see text) are positively biased whereas C_u and C_d are negatively biased, resulting overall in an octupole electric field configuration. Both the magnetic and electric fields have rotational symmetry with respect to the z-axis.*

When $\vec{\mu} = 0$, the effective potential in the positron cloud along the magnetic field line is constant because of the balance between the space charge potential and the octupole potential. However, when $\vec{\mu}$ is finite, the positron cloud is compressed by the third force described above along the magnetic field line, and will have a higher space charge potential than that with $\vec{\mu} = 0$. In other words, a potential well for antiprotons is formed at the position of the positron cloud, and antiprotons and positrons automatically condense near the central region of the cusp trap to form a neutral plasma even when they are very cold (this can never happen in the case of the nested trap scheme).

C.2 Antiproton Injection and Cooling

Once the positrons are cold enough, an antiproton pulse can be injected into the cusp trap along the axis of its magnetic field z. To confine these simultaneously with the positrons, three electrodes must be added outside of the octupole electrodes as shown in fig.C.4. From left to right these are a disk-shaped outer upstream electrode D_{ou}, a cylindrical outer electrode C_o, and a disk-shaped outer downstream electrode D_{od}.

Pulsed antiprotons injected from the left side of the cusp trap pass through D_{ou}, D_u, the positron cloud at the centre of the trap, and the electrode D_d. They are then reflected by electrode, D_{od}. On their return trip towards D_{ou}, they once again pass through the positron cloud. Before they reach this initially grounded electrode, it is switched to a negative bias. The result is that the antiprotons are subsequently confined inside these outer electrodes. An example of a confined antiproton's trajectory is shown by the brown line in fig. C.4. As can be seen, antiprotons move back and forth in the direction of z-axis as well as in the z=0 plane. To 'plug' the motion in the z-plane, the cylindrical electrode C_o surrounding the octupole electrodes is also negatively-biased (see fig. C.4). During their travels, they pass through the positron plasma at the trap centre, and thus are sympathetically cooled via collisions with positrons. The end result is that they are eventually confined in the same region as the positrons.

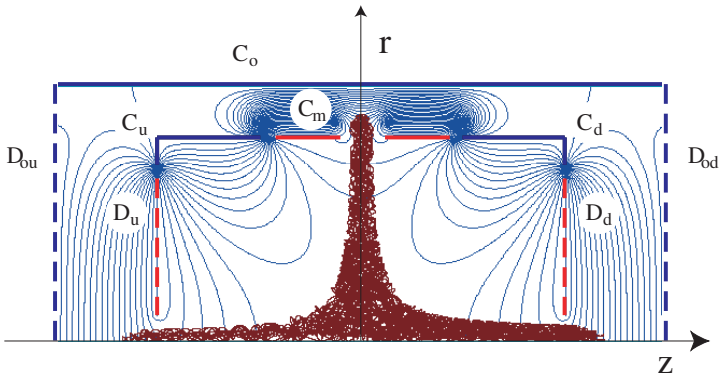

Figure C.4: *A trajectory of antiprotons with negatively biased outer electrodes. It is seen that antiprotons are stably confined. The dotted lines indicate that these parts are made by mesh electrodes so that the synthesized antihydrogen can be extracted with high transmission efficiency.*

C.3 Synthesis of Spin-Polarized Antihydrogen Beam

As explained above, cooling of the antiprotons results in an electrically neutral mixture of positrons and antiprotons condensing near the central region of the trap. Consequently, the recombination of antiprotons with positrons can be expected to take place at much lower temperature than the case for a nested trap configuration [105, 106].

It is quite difficult to evaluate the velocity distribution or a temperature of LS antihydrogen atoms in the cusp trap on account of unknown factors such as (among others) (1) the velocity dependence of the recombination rate in a magnetic field, (2) the re-ionization rate via motional Stark effect, (3) the spin-exchange rate due to collisions with dense positrons in the trap (LS-HS conversion). In the following discussion, we would nevertheless assume that the antihydrogen atoms are in 1S state and have a Maxwell-Boltzman distribution.

The resulting antihydrogen atoms can be focused or even be trapped depending on their kinetic energies as follows. Let 's assume an antihydrogen atom is formed in the 1S state with total spin F=1 near the center of the cusp trap, where the magnetic field is very small. When such an atom enters a non-zero magnetic field region, its state splits into the triplet $(F, M_F) = (1,1), (1,0), (1,-1)$ according to its total magnetic quantum number M_F . As the Breit and Rabi diagram [137] shows, the magnetic moment μ in the (1,1) and (1,0) states is anti-parallel to the magnetic field B; antihydrogen atoms in these states 'prefer' weaker fields and move into them. They are therefore called low-field seekers (LS). High-field seekers (HS) (the (1,-1) and (0,0) states) have μ parallel to B and are attracted towards higher fields. In the case of (1,1) and (1,-1) states, μ has no dependence on $|\vec{B}|$, although it varies with $|\vec{B}|$ for the states (1,0) and (0,0).

The force on an antihydrogen atom, $\vec{f}$, and its potential energy, W, at a position $\vec{r}(= (r, \theta, z))$ can be written in terms of an effective magnetic moment $\mu_{eff} > 0$ as

$$\vec{f}(\vec{r}) = s\mu_{eff}(|\vec{B}(\vec{r}|)\nabla|\vec{B}(\vec{r})|, \tag{C.1}$$

$$W(\vec{r}) = s\int_0^{\vec{r}} \mu_{eff}(|\vec{B}(\vec{r})|d(|\vec{B}(\vec{r})|) \tag{C.2}$$

where $s = +1$ and $s = -1$ are for HS and LS, respectively. Trajectories of antihydrogen atoms in these states are then evaluated by solving the equation of motion numerically. The magnetic field in the central region is quadrupolar and its strength $|\vec{B}|$ is proportional to $\sqrt{r^2 + 2z^2}$. LS atoms are decelerated but those with sufficient kinetic energies can overcome the magnetic barrier and then be focused on the central z-axis of the trap. The solid lines in fig. C.5 show examples of the simulated trajectories of 0.27meV LS atoms for a reasonable magnetic field configuration [134]. It is seen that the fraction of LS atoms with divergence angle θ less than ~ 24 degrees are focused. Assuming that the energy distribution of antihydrogen atoms is the same as that of antiprotons having the Maxwell-Boltzman distribution of 4K, the overall efficiency for collecting antihydrogen atoms can be estimated to be $\sim 0.3\%$, which corresponds to a flux enhancement of ~ 30. The trajectories of 0.27meV HS antihydrogen atoms are shown by the dotted lines in fig. C.5, which are diverging and are practically removed from the forward direction. This results in an intensity-enhanced antihydrogen beam with $\sim 100\%$ spin polarization.

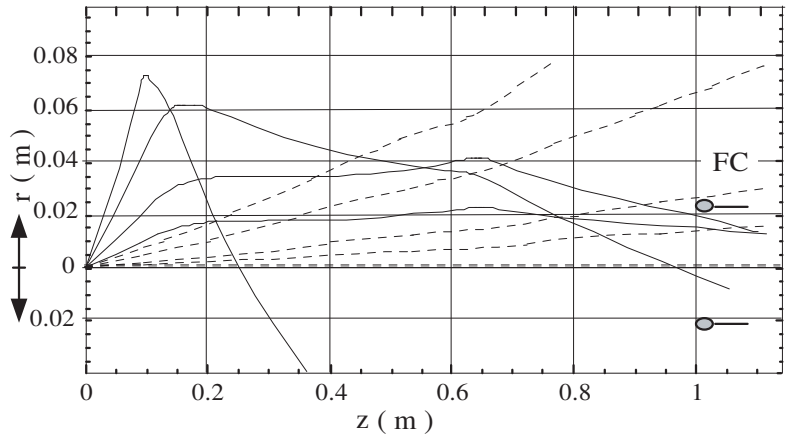

Figure C.5: *Some trajectories of antihydrogen atoms in LS(solid lines) states emitted at 5, 10, 20, and 30 degrees, and in HS (dotted lines) states emitted at 0.5, 1.1, 3 and 5 degrees with kinetic energies around 4K. [134]*

The potential barrier height for the LS antihydrogen atoms by the cusp field is given by $\sim 60 B_{\max}[\mathrm{T}]\mu\mathrm{eV} \sim 0.7 B_{\max}[\mathrm{T}]\mathrm{K}$. Those atoms which have kinetic energies less than this are confined by this magnetic well, i.e., the cusp trap configuration proposed here confines not only charged particles of both polarity but also neutral particles [1]. Figure C.6 shows possible trapped fractions for four different magnetic barriers as a function of the temperature of antihydrogen atoms in 1S state.

Because the magnetic cusp has a null point at the centre, Majorana spin-flip transitions [138] can occur as atoms pass through its central region. This shortens the confinement time of antihydrogen atoms in the LS states. However, the transition can take place only around the region very close to the symmetry point at the center of the trap where $|\vec{B}| \sim 0$ and a considerable fraction of low energy antihydrogen atoms can then be expected to be confined in

[1] Antihydrogen atoms will initially be formed in high Rydberg states, and generally have high angular momenta. The magnetic properties of antihydrogen atoms are accordingly governed by the orbital magnetic moment rather than the spin magnetic moment, which is favorable for efficient trapping of antihydrogen atoms and for quenching them down to 1S state. It is important to remove these excited components for precision measurements of the hyperfine splitting of antihydrogen atoms.

the cusp trap for long periods [2]. In conclusion, the trapping times to be expected from the above discussion should be sufficient to allow antihydrogen atoms in Rydberg states to cascade down to the 1S ground state [139].

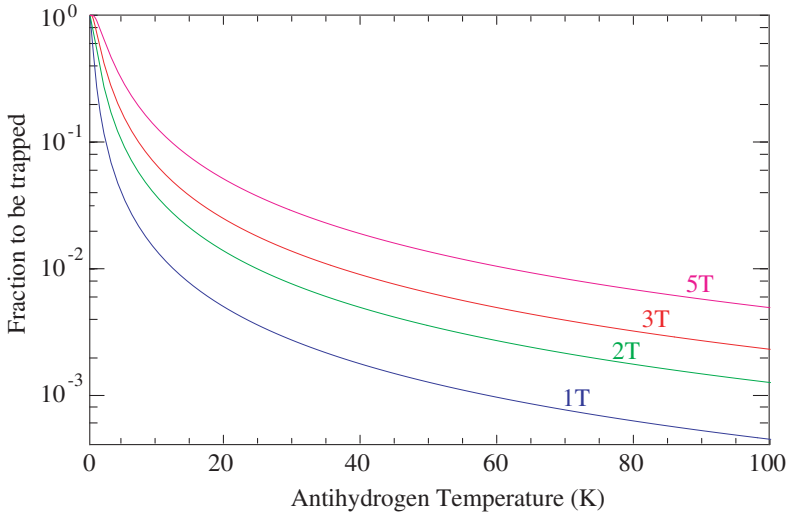

Figure C.6: *Trapped fraction of antihydrogen atoms as a function of the antiproton plasma temperature for the trap depth of 1T, 2T, 3T, and 5T.*

C.4 Superconducting Quadrupole Magnet

Figure C.7 shows the quadrupole magnet in preparation at RIKEN, which consists of several superconducting coils coaxially configured with the bore radius of 160mm and the total length of 650mm. The present coil configuration allows to generate not only the cusp field but also a quasi-uniform field. Figure C.8 shows a photograph of the superconducting magnet. The maximum field strength $B_{max}is \sim 3.5T$ at $|z| = 0.15m$ with weak dependence on r. In the z=0 plane, it increases more or less linearly and reaches $\sim 1.3T$ at $r = 0.06m$.

The proposed cusp trap scheme will be fully tested with electrons and protons. During these tests the synthesis of hydrogen atoms, the transport and the trapping characteristics feature will be examined, initially with a warm bore, and then with a cold bore at ∼4K. Once hydrogen atoms are synthesized, a considerable fraction (something like $\sim 10\%$) of them are expected in metastable 2S states, which can be easily detected with a microchannel plate detector. Since antihydrogen atoms are initially created in high orbital angular momentum states with correspondingly large magnetic moments, it should be easy to trap them in the cusp field. Although the orbital angular momentum distribution of antihydrogen atoms formed via three-body recombination process is not known, a statistical distribution could be a reasonable guess as the first approximation. In this case, a considerable fraction of antihydrogen atoms in high Rydberg states are trapped even when the plasma temperature is much higher than assumed above. This provides a good test case for the present scheme.

[2] A value of 0.8 seconds has been reported for the trapping time of cold Na atoms in a maximum field of 0.025T in a similar trap, even for relatively poor vacuum ($\sim 10^{-8} Torr$). Collisions with background gas limited this trapping time. A. L. Migdall et al., Phys. Rev. Lett 54 (1985) 2596.

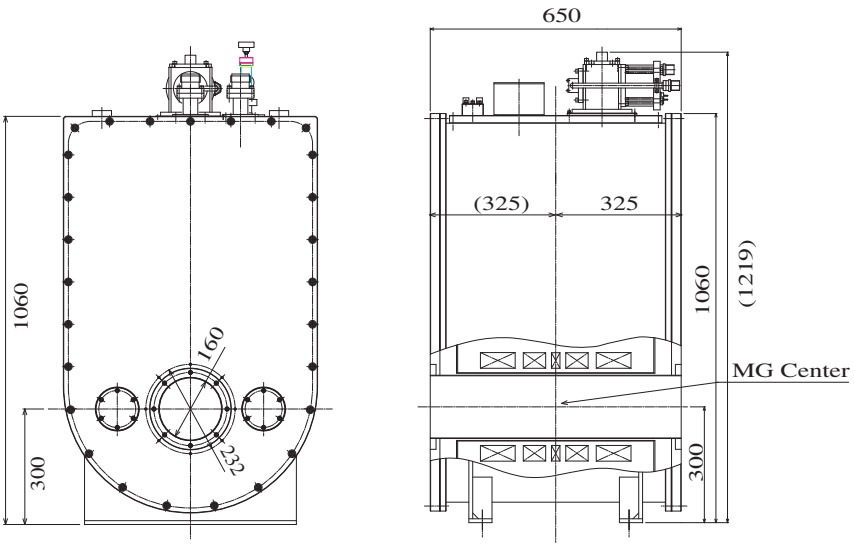

Figure C.7: *Drawing of the superconducting quadrupole magnet.*

Figure C.8: *Photograph of the superconducting quadrupole magnet.*

D. Positron source

D.1 Introduction

One of the founders of the relatively new technique of buffer-gas assisted positron trapping in a Penning trap, R. Greaves, offers through his company, First Point Scientific Inc. [140], a complete 'turn-key' device [141] that is capable of fulfilling the rather strict requirements on the beam to be used to produce antihydrogen, see table D.1.

Bunchlength	20 ns
Beamsize	$\lesssim 1$ mm (σ)
Intensity	$> 10^7$ e^+/shot
Energy	2 eV
Energy spread	$\simeq 1$ eV
Pressure	10^{-11} mbar

Table D.1: *Requirements for the positron beam quality to be used for the production of* $\overline{\mathrm{H}}$.

D.2 Positron source

The source of positrons is a conventional 50 mCi ^{22}Na radioactive e^+ source with a solid neon moderator. The energy spectrum from the ^{22}Na decay is very wide with a centroid around the electron rest mass. The function of the moderator is to intercept, cool to thermal energies and re-emit the positrons. Any solid with a negative work-function for positrons would work as a moderator. Single crystal tungsten is a stable and rugged choice for positron moderation but solid Ne offers higher moderation efficiency. In solid Ne the efficiency is $\simeq 1\%$ and the positrons are emitted with an energy spread of down to 0.25 eV (σ) [142] and for the commercial device $\simeq 2$ eV. The moderation deteriorates with about 5% per day due to contamination of the frozen Ne layer which must be replaced. This procedure takes less than 20 minutes.

D.3 Buffer-gas e^+ accumulation in a trap

Since the initial development in the mid-90s, see e.g. [143], the buffer-gas technique for trapping positrons in a Penning-trap has been widely used. The successful trapping technique developed by M. Charlton's group in the CERN collaboration ATHENA is a refinement of the original idea and C. Surko's group [143] is presently investigating e.g. molecular interactions at very low energies using this technique.

The buffer-gas method relies on slowing down of the positrons in sections that are differentially pumped with successively lower pressure, lower positron energy and deeper potential well, see figure D.1.

The commercial product is another development of the Surko-type trap: Instead of the slowing down and capture taking place in the same section, the new apparatus is modular as

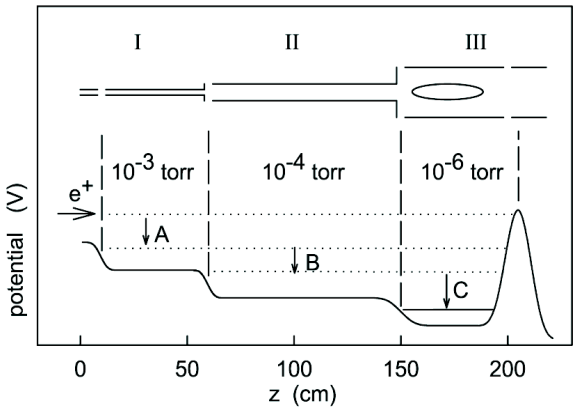

Figure D.1: *Schematic drawing of the Surko-type [143] buffer-gas trap. Differential pumping in sections I, II, and III provide a decreasing pressure while slowing down the positrons. The lower half of the figure shows the electric potential and transverse confinement is obtained by a solenoidal field along the trap axis.*

shown in figure D.2. This enables better differential pumping and thus longer lifetime (> 1000 s) of the positrons in the accumulator section. Stacking proceeds at a rate of $5 - 10$ Hz and the stacking efficiency can be almost 90% in a solenoidal field of 500 gauss. The apparatus is capable of delivering up to 80 million positrons in a single pulse.

D.4 Transverse compression

By the so-called rotating-wall method the positron plasma can be radially compressed inside the accumulator. This method relies on an azimuthally segmented electrode to which a suitably phased sinusoidal electric wave is applied. This induces a rotation of the plasma that reduces the diameter [144, 145]. The demonstrated performance has achieved a compression of a factor 13 of the diameter, i.e. more than two orders of magnitude in density. The final diameter is less than 1 mm (FWHM).

D.5 Longitudinal compression

As shown in [146] for a microtron-based electroproduced positron beam [147], longitudinal compression of the trap-based beam can be performed by applying a harmonic potential to the positron beam, providing a factor $\gtrsim 100$ compression at the expense of a spread in beam energy. Another option is the so-called timed potential method where a potential with a quadratically varying amplitude is applied to an electrode during traversal by the bunch [148]. The time structure from the two-stage trap, however, already has a 'natural' width of $\lesssim$20 ns, so compression will probably not be necessary.

D.6 Testing and verification

The Aarhus group has many years of experience in handling low energy positron beams for atomic physics experiments [149–154]. Thus, the Aarhus laboratory is well equipped with detectors

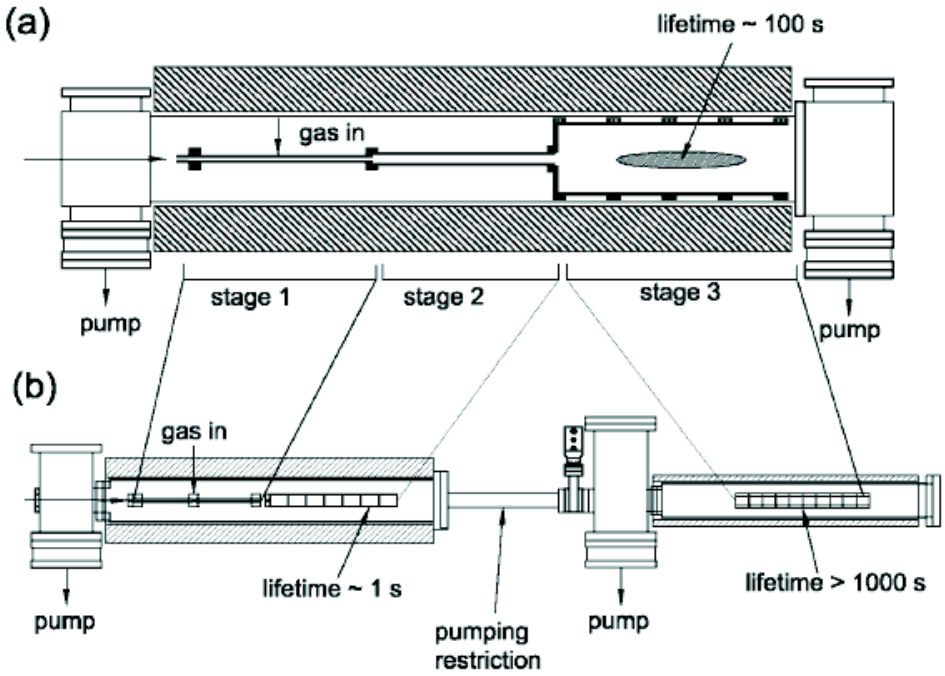

Figure D.2: *Schematic drawing of a) the Surko-type and b) the commercially available buffer-gas trap. The modules in b) are a two-stage trap and an accumulator with very long lifetime and good vacuum.*

Figure D.3: *A photograph of the two-stage trap and the accumulator.*

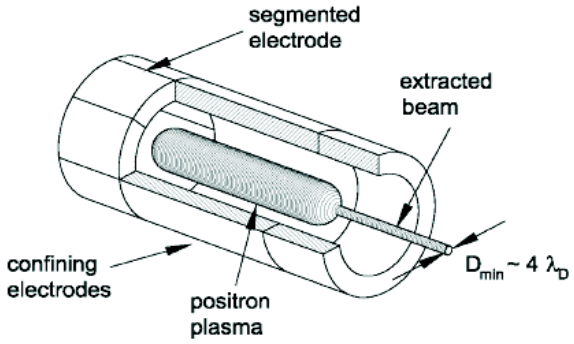

Figure D.4: *Bunch compression by the rotating-wall technique.*

suitable for testing the beam quality from the trap, e.g. to verify the factory value of the energy spread by a magnetic bottle spectrometer [155]. The magnetic bottle spectrometer has been tested with a pulsed beam of electrons and has an energy resolution of about 20 meV, ideally suited to tests of the beam from the trap.

D.7 Timeline and budget

The commercial product is available with a delivery time of approximately 9 months after receipt of order. Initial testing and verification of beam quality is proposed to take place in Aarhus and upon completion of the test phase ($\simeq$ 6 months), the apparatus will be shipped to CERN.

The cost of the sections are: RGM-1 moderator: USD 140k, Two-stage trap: USD 156k and Accumulator: USD 141k and the ^{22}Na source costs approximately USD 50k.

E. Technical details of atomic-collision experiments

E.1 Antiprotonic atom formation processes I: Collision of 10-100eV extracted antiprotons with supersonic gas-jet target

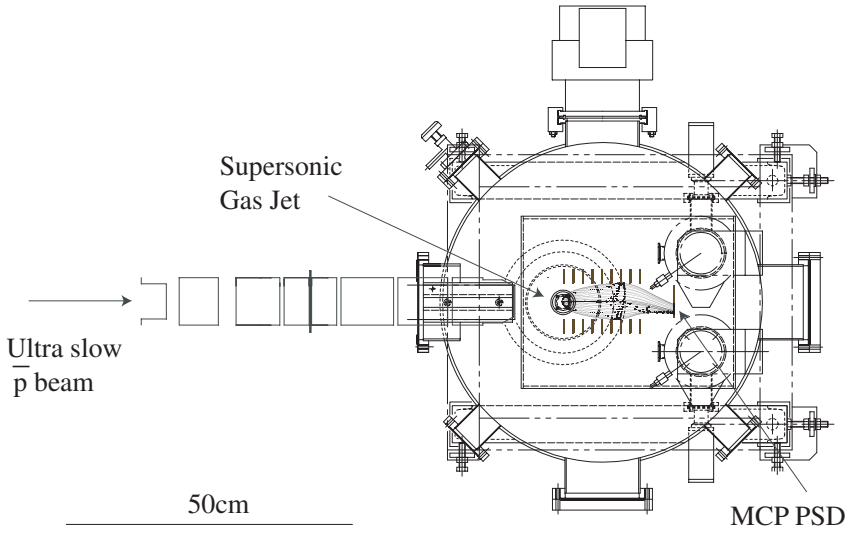

Figure E.1: *A drawing of the collision chamber with a supersonic gas-jet target and a part of the MUSASHI beamline*

Figure E.1 shows a drawing of the experimental setup. Antiprotons of 10-100eV extracted from the MUSASHI trap [156] are injected in the collision chamber, focused on the supersonic gas-jet target, and then detected by the MCPPSD (Microchannel plate position sensitive detector) placed downstream of the target. The collision chamber consists of an expansion chamber with a gas cell cooled down $\sim$ 30 K, a collimation chamber, the main chamber, and 1st and 2nd dumps of the supersonic gas jet. The expansion chamber and the gas cell nozzle of the supersonic gas-jet system are on a XYZ stage and are alignable against the skimmer fixed to the collimation chamber with a precision of several tens μm. The target gas density of the present setup can be 1×10^{13} cm^{-3} keeping the collision chamber pressure below 1×10^{-6} Torr, which satisfies the requirements of the MUSASHI beamline.

Slow electrons released during the antiproton formation process are collected to the MCPPSD by a parallel-plate electrostatic guide, which are used to select electron release events. Simulated trajectories are drawn in Fig. E.1, which indicate that the released electrons can be focused on a limited area of the MCPPSD. It was found that the antiprotons can be focused on a different position with the same electric field configuration, which helps to improve the s/n ratio. Figure E.2 shows a photo of the collision chamber together with the extraction beamline.

The antiprotonic atom formation cross sections will be measured for molecular targets (H_2, N_2, etc.) as well as multi-electron targets (He, Ne, etc.) in the collision energy range of 10-100 eV.

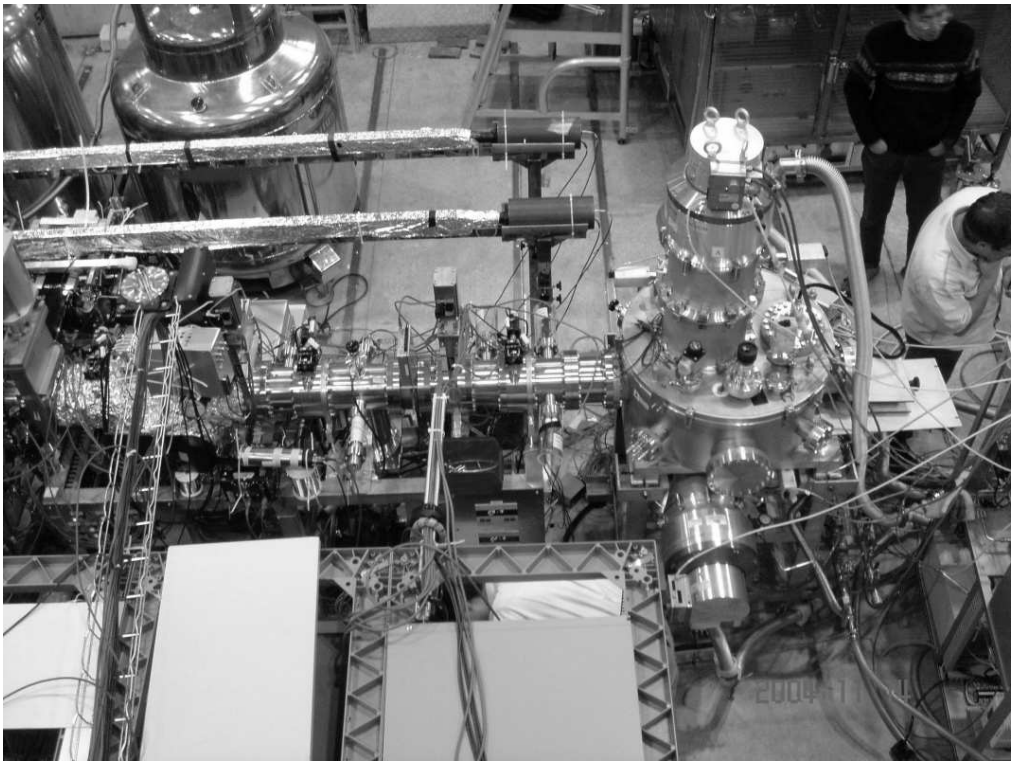

Figure E.2: *A photo of the collision chamber connected to the MUSASHI beamline*

With the MCPPSD, antiprotonic atom formation cross section differential to momentum transfer can be obtained, which is particularly interesting in the case of molecular targets.

At the target density described above, the reaction probability is $\sim 0.1\%$. Considering that the number of antiprotons extracted to the target area was a few hundred thousands every three AD shots, two energy points will be obtained with one shift.

A closed gas re-circulation system was designed for H_2 and D_2 targets to make the experiments safely, which consists of (1)gas supply system, (2)buffer and purifying system, and (3) the collision chamber. The gas supply system is to refill the gas into the re-circulating route at the beginning of the experiments. The buffer and purifying system is to remove oil mist from the re-circulating target gas. The gas cell placed on the cryohead is cooled down to 30K to increase the target density with relatively low pressure (37 Torr), which allows to operate the supersonic gas jet at relatively low gas load to the evacuation system of the expansion chamber.

E.2 Antiprotonic atom formation processes II: Collisions of supersonic gas-jet beams with trapped antiprotons

In order to study the antiprotonic atom formation processes in the meV range, a well-collimated supersonic gas jet with an internal temperature of a few μeV is injected in an antiproton target stored in a MRT (multi-ring trap) installed in a compact superconducting solenoid as shown in Fig. E.3

Antiprotons are transported from the MUSASHI trap, and stored in the MRT. In this experiments, all the antiprotonic atoms effectively annihilate in the trap, and the number of

annihilations in the MRT is the direct measure of the antiprotonic atom formation cross section.

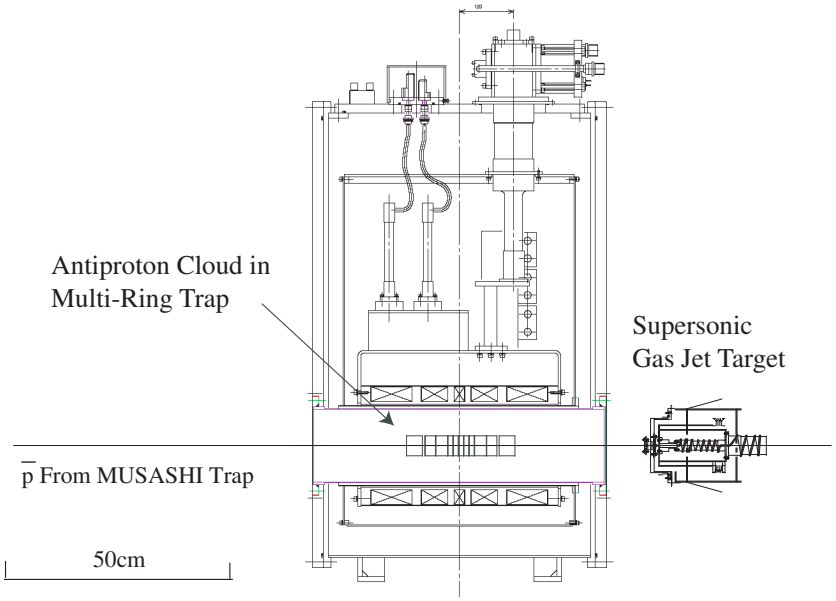

Figure E.3: *A schematic drawing showing the collision between supersonic gas-jet projectile and antiprotons stored in the multi-ring trap.*

The supersonic gas-jet beam is prepared by a free jet expansion of high-pressure gas through a nozzle. During the expansion, the velocity of the gas flow increases and approaches a so-called terminal velocity $\sqrt{\frac{2kT_0}{m}\frac{\gamma}{\gamma-1}}$ decreasing the internal temperature, where m is the atomic mass of the gas, T_0 is the temperature of the gas before expansion. When the gas is pre-cooled to 30 K, the terminal velocity is $\sim 3 \times 10^2$ m/s ($\sim$meV) and the internal temperature is below $\sim$ 1K($\sim$ μ eV). In this way, a He beam density of $10^{10}/\mathrm{cm}^3$ at $\sim$meV terminal energy is prepared. The "current" density equivalent to this gas-jet beam is as high as $\sim$ 100 $\mu\mathrm{A/cm}^2$. For the supersonic gas-jet beam having a flux of $10^{13}/\mathrm{cm}^2$ s (i.e., $\sim 10\mu\mathrm{A/cm}^2$) and flowing into a cloud of 10^6 $\overline{\mathrm{p}}$, the signal rate is as high as $\sim 10^4$ /s assuming the cross section to be 10^{-15} cm^2. Plastic scintillators are prepared around the trap to monitor the annihilation of antiprotonic atoms in the trap, the lifetime of which is evaluated by the time difference between the photon emission and the annihilation.

E.3 Antiprotonic atom formation with antiproton-ion collisions

Antiprotonic atom (ion) formation processes between antiprotons and ions will be studied by two ways, one for collision energies of 10-100 eV, and the other for collision energies below 1 eV. In both cases, antiprotons are transported from the MUSASHI accumulation trap to the experimental trap as discussed in the previous subsection.

In the case of "energetic" collisions, an ion beam of several tens of eV is injected into the trap along its axis. The strong magnetic field helps to focus the beam on the antiproton target.

As the quality of the incident A^+ beam is quite high in the sense of the angular divergence and energy width, the resultant $\bar{p}A^+$ is expected to succeed this excellent feature, *i.e.*, one can prepare a high quality $\bar{p}A^+$ beam in vacuum, which could be used for further investigations.

The yield of $\bar{p}A^+$ is evaluated to be ∼10 /s for the incident ion beam current of 1 nA into a plasma of $\sim 10^6$ antiprotons with a size of ~ 10 mm^3 in the trap.

In the case of "slow" collisions, ions as well as antiprotons are stored in a nested trap, the scheme of which has been used for antihydrogen synthesis.

E.4 The energy loss of slow antiprotons in gases and solidified gases.

One of the most important aspects of the interaction of charged particles with matter is their slowing down, which is due to collisions with the atoms of the material. Since there is a plethora of combinations of projectiles, projectile charges, projectile energies as well as target atoms, atomic compositions and target phases, it is necessary to have accurate theoretical calculations to cover the many cases where experimental data are missing. Furthermore, the physical models on which these calculations are based have to be realistic, and these models are themselves of fundamental interest.

Due to the practical importance of the slowing down and the resulting energy transfer to the target, a number of data tabulations have been compiled, with semi-empirical curves fitted to the experimental results [157].

To create a clear understanding of the mechanisms leading to energy loss, some of the members of the ASACUSA collaboration have performed extensive measurements of the so-called stopping power dE/dx, which is the loss of projectile kinetic energy per path length. We chose to compare impact of protons with impact of antiprotons, since the reversal of the sign of the Coulomb interaction between these two cases allows a direct extraction of the higher order terms in perturbation expansions of the stopping power for swift projectiles (for example polarization effects and effects of target electron correlation). This resulted in a much better understanding of the slowing down of swift particles in general [158].

For slow projectiles (defined here as projectiles moving with velocities in the order of- or smaller than those of the target electrons which cause the main part of the energy loss) the situation is much less satisfactory, since there are still open discussions of the mechanisms which cause the slowing down. Here again, our measurements with equivelocity protons and antiprotons have cleared up many outstanding questions. This is because the comparison allows a direct extraction of the polarization effects, and also because a substantial contribution to the stopping power of positive projectiles, namely capture and loss of target electrons, is absent in the case of the negative antiprotons. In our recent work [30, 31] we show that the fundamental model for energy loss of slow projectiles, namely the free electron gas model, is valid for "metallic" targets, where there exist almost free valence electrons. One of the consequences of this model, which was confirmed by our measurements, is the projectile velocity proportionality of the stopping power.

Taken together, the work mentioned above covers an antiproton kinetic energy range from several MeV to 1 keV, a feat which was made possible partly by the availability of the unique ASACUSA low energy beam line.

There are, however several outstanding questions to be elucidated, foremost among them the behavior of the stopping power for slow projectiles passing through non-metallic targets such as insulators and gases. For such targets, the free electron gas model should not work, because there exists a minimum energy transfer E_g in the interaction of the projectile with the (bound) target electrons. In 1947, Fermi and Teller [26] suggested that the effects of this minimum, which lead to a much reduced stopping power, would occur below a projectile velocity v, where

$$v v_F m = E_g.$$

Here m is the electron mass, and v_F the velocity of the active target electrons, and the left-hand side of the equation is a typical energy transfer to such an electron.

In fact, deviations from velocity proportionality of the stopping power have been observed in two cases, namely for protons on He and (to a lesser extent) for protons on Ne [159, 160], and the transition to a much steeper velocity dependence occurred approximately at the projectile velocity mentioned above.

It was therefore a great surprise when the same group [161] found strict velocity proportionality of the stopping power for slow protons in insulators such as LiF, where the band-gap is of the same order of magnitude as the lowest excitation energies of He and Ne. This was tentatively explained as being due to a sizeable contribution to the stopping from electron promotion processes, where electrons are promoted to molecular-like orbitals [162]. In the band-structure description of solids, the large band gap is therefore locally reduced by the presence of the positive projectile. This model is plausible, because it postulates a mechanism which depends on the transfer of target electrons to the projectile, a phenomenon which is known to contribute substantially to the stopping power of positive projectiles. In the same line of reasoning, it should of course not work for antiprotons as projectiles, since they are negative and do not capture target electrons.

Nevertheless, recently we observed [31] strict velocity dependence of the stopping power of slow antiprotons passing through LiF. This casts serious doubt on the "promotion" model, and leaves us in the situation where we have no sufficient understanding of the slowing down of charged particles in insulating materials.

In order to remedy this, we suggest to measure the stopping power of protons and antiprotons in gaseous targets, such as He, Ne and Ar, as well as in the solid form of Ne and Ar. It is only for gas targets that the "cut-off" in the stopping power has been observed, while for all solid targets we observe a velocity proportionality, which might be caused by the phase of the target.

E.4.1 Experimental technique - gas measurements

The proposed experimental setup is based on the already existing ESA apparatus, where the foil target will be replaced by a gas cell, as shown in Fig. E.4.

Here, the projectiles enter the first electrostatic analyzer, where their energy is determined. Then they pass the target, and their exit energy is recorded by the second analyzer followed by a channel plate detector equipped with CCD readout (not shown). The energy loss is measured as function of the target gas density. Figure E.5 shows the gas cell. It is mounted with an entrance - and an exit arrangement consisting of pieces of aligned channelplates covered by 100 Å carbon foils. This allows a dE measurement, since the energy loss in the carbon foils will be 600 eV in total, while the energy loss in 2 mbar Ne of 5 cm length will be 600 eV for 4 keV antiprotons. We have tested that such carbon foils will sustain this kind of target pressure.

An important question is the reduction of the transmission through the gas cell due to multiple scattering in the foils, and due to the limitations imposed by the channels of their support. Monte Carlo simulations show that we can expect a reduction by a factor of 5 compared to the transmission that we had in our foil measurements. Figure E.6 shows the resulting transmission, as compared with the observed transmission for the foil measurements.

In our earlier measurement we were able to reach energies as low as 1 keV. From Fig. E.6 we can see, that with the gas cell we should be able to go down to a projectile energy of 5 keV, which is sufficient to investigate the velocity dependence of the gas stopping power.

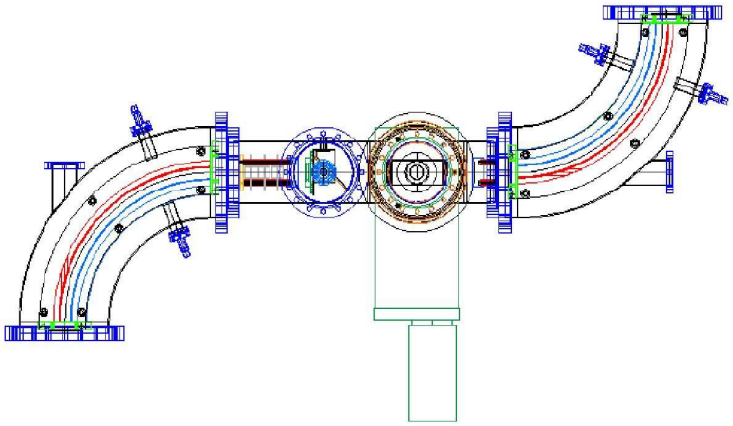

Figure E.4: *The ESA apparatus with a gas cell at the target position.*

Figure E.5: *The gas cell. It is mounted on an insulator, so that we can change the impact energy without retuning the ASACUSA RFQD, which facilitates the measurements at varying projectile energies.*

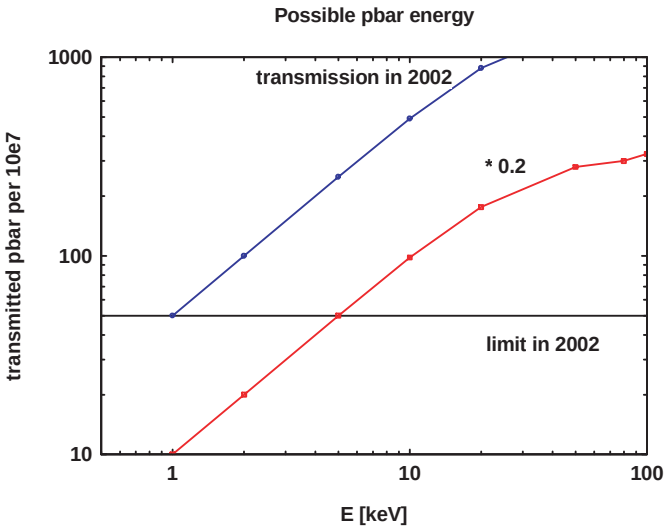

Figure E.6: *Transmission in our earlier measurements on thin foils, and the expected transmission through the gas cell.*

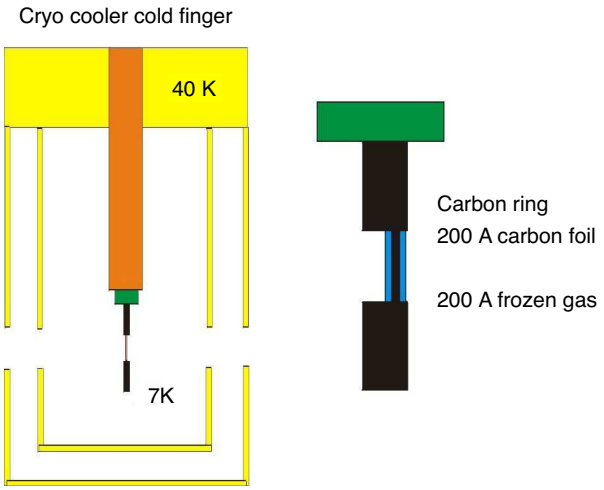

Figure E.7: *A thin carbon foil is mounted on the tip of a cryo cooler. A layer of frozen gas can be reproducibly deposited on this foil.*

E.4.2 Experimental technique – frozen gas targets

In order to investigate the dependence of the stopping power on the target phase, we suggest to measure energy loss in frozen Ne and Ar targets. Figure E.7 shows the principle:

A gas flow will create a known pressure of the target gas for a known length of time. This will give a deposited thickness reproducible within a few monolayers. Normalization of the target thickness will be achieved via measurements with protons. The "lifetime" of such a frozen layer is limited by the "dirt" deposition, which at 10^{-8} mbar is known to be ~ 1 monolayer per hour. A new target layer can be established in a few minutes.

In conclusion we suggest measuring the stopping power of gaseous targets as well as of

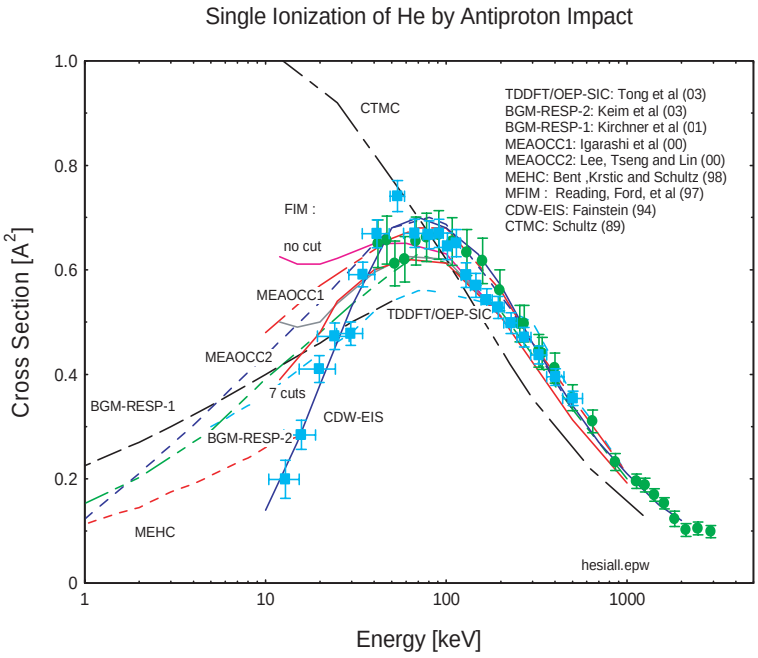

Figure E.8: *The total cross section for single ionization of helium by antiproton impact. The squares are our data from previous investigations.*

frozen gases for low energy antiprotons. For this we need the ASACUSA beamline, including the RFQD.

E.5 Measurements of the total cross section for ionization of atoms and molecules by impact of slow antiprotons

Even though the ionization of atoms in collisions with charged particles was one of the first processes investigated after the discovery of the structure of atoms in the beginning of the last century, there is still no firm theoretical basis for calculations of the ionization probability for impact of projectiles with velocities around and below those of the active electrons. This is even the case for the simplest collision systems, such as slow antiprotons impinging on targets such as atomic hydrogen and helium. There is therefore a great need for benchmark data for these systems. Antiprotons are ideal for this purpose, since electron transfer is excluded, and since the projectiles are heavy, so that their trajectories are well understood. Figure E.8 shows a compilation of the latest theoretical calculations of the total ionization cross section for the helium target, compared with our previous experimental data for antiproton impact [163].

As can be seen, there are considerable differences among the various calculations, and between the calculations and our previous data. It can also be noted that new calculations are appearing frequently, illustrating the interest from theorists in this problem. Clearly there is a need to investigate this cross section for impact energies in the range 1 – 30 keV. A similar situation is found for the total cross section for single ionization of atomic hydrogen as well as for double ionization of helium.

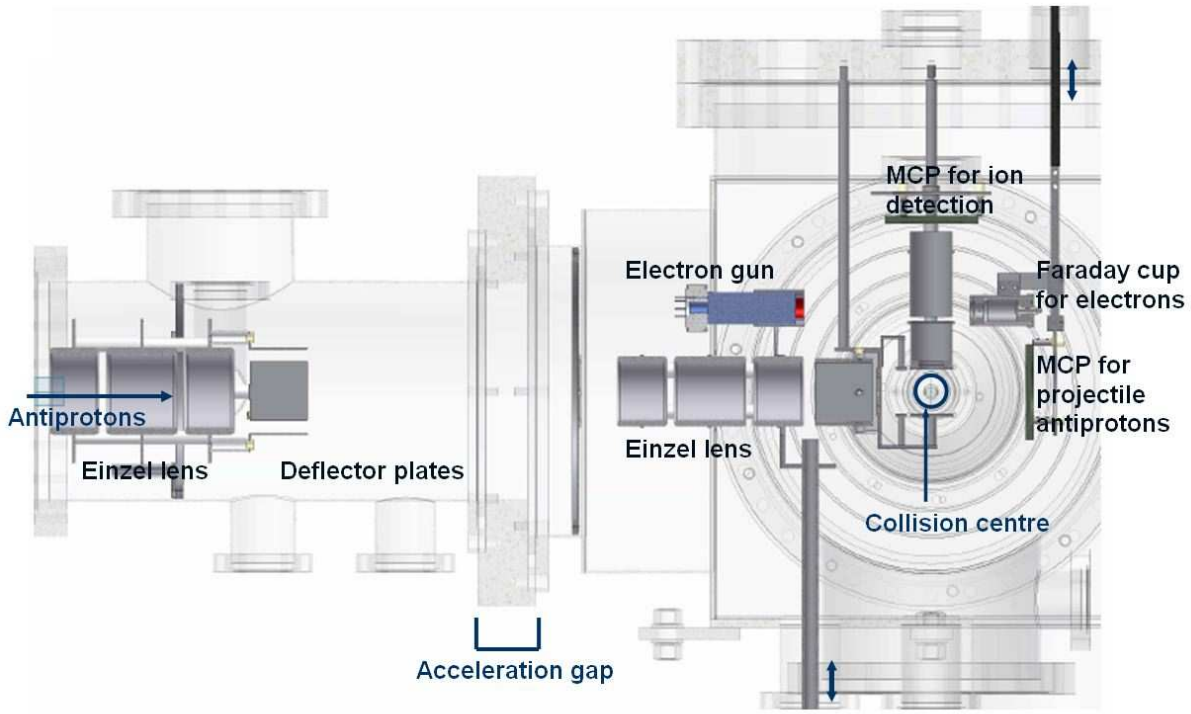

Figure E.9: *The central part of the AIA (Aarhus Ionization Apparatus).*

E.5.1 Experimental technique

The basic principle for the measurements is that we cross a beam of low energy antiprotons with an effusive beam of the target atoms. We then extract and detect the ions created, and measure their time-of-flight, so as to determine their mass-to-charge ratio. The product of target density and detector efficiency is determined using a pulsed 3 keV electron beam for which the ionization cross sections have been measured. The number of antiprotons passing the target is determined for the signal of an MCP detector. In the special case of atomic hydrogen as target, we apply a microwave discharge cavity to dissociate the hydrogen molecules. Dissociation fractions of 80% at the target position have been reached in test runs, as well as target densities of $10^{11}/\mathrm{cm}^3$. For the other target gases, target densities of $10^{12}/\mathrm{cm}^3$ are obtained. The central part of the AIA apparatus is shown in Fig. E.9.

The low energy antiprotons are produced in the ASACUSA beam lime, which delivers bunches to the MUSASHI penning trap. Here the antiprotons are captured and cooled. Then they are extracted as a 250 eV DC beam of 10 sec duration which passes through a differentially pumped beamline. At the end of this beam line we typically get 5×10^5 antiprotons per 3 AD shots. Entering our apparatus, the antiprotons are accelerated to their collision energy, which can be up to 25 keV. They are then collimated and pass the target region. We were able to detect approximately 20% of the antiprotons on our end detector. These results were obtained during 2004 mostly due to a great effort by the members of the Komaba group.

The estimated signal for a typical ionization cross section of 10^{-16} cm^2 would be

$$N = \sigma n l N_{\mathrm{proj}} = 10^{-16}\mathrm{cm}^2 10^{12}\mathrm{cm}^{-3} 1\mathrm{cm} N_{\mathrm{proj}} = 10^{-4} N_{\mathrm{proj}}.$$

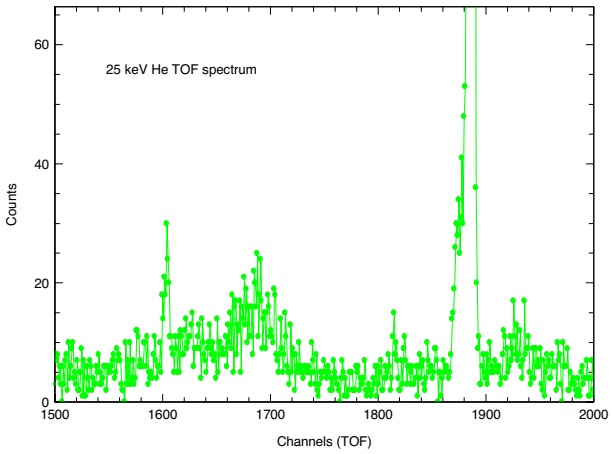

Figure E.10: *The TOF spectrum of the AIA apparatus for 25 keV antiprotons on helium. The "prompt" peak is at channel 1880 and the He^+ peak is at channel 1600.*

With 10 extractions from the Penning trap per hour this gives 100 counts in the ionization TOF peak per hour. Consequently, we can measure one cross section per shift, including time used to set up the extraction and for background measurements.

During the last days of the 2004 run, where the extraction of antiprotons from the MUSHASI trap worked well, we were able to obtain spectra like the one shown in Fig. E.10. Here the TOF spectrum shows a broad background with a narrow peak (at channel 1600) stemming from He^+ ions created by 25 keV antiproton impact on helium gas. Approximately 4 hours were used for the accumulation. This proves the ability of our apparatus, as expected.

In conclusion, we suggest performing measurements of the total cross sections for single and multiple ionization of atomic hydrogen, molecular hydrogen, helium, neon and argon for $1 - 30$ keV antiproton impact.

E.6 Multiple angular scattering of antiprotons

One of the limiting factors in the design of experiments using antiproton beams such as the slowing down of antiprotons in a helium target for pbar-helium measurements, the capture of antiprotons in a Penning trap (AD1 and AD2) as well as the utilization of antiprotons in cancer treatment (the AD4 collaboration) is the angular spreading of the antiprotons in multiple collisions while traversing solid or gaseous targets. The angular scattering of positive ions is fairly well understood [164], but no information exists on antiproton multiple scattering.

Due to the practical importance of this phenomenon, we suggest to measure multiple scattering distributions of antiprotons in a number of targets. Considerations of scattering in screened Coulomb potentials [165] lead to the suggestion that the width (FWHM) of such distributions for antiprotons should be larger than the corresponding widths for protons of the same energy. It is particularly important for applications that for sufficiently small values of the target thickness, deviations from a Gaussian distribution may be large, and in contrast to the Gaussian (where it is 50%), up to 80% of the intensity may be found outside the FWHM [166]. As the angular distributions generally scale inversely proportional to energy, such distributions may conveniently be studied in the keV range, but the results extrapolated well into the MeV range.

Multiple scattering distributions are known to be influenced by channeling in crystallites of

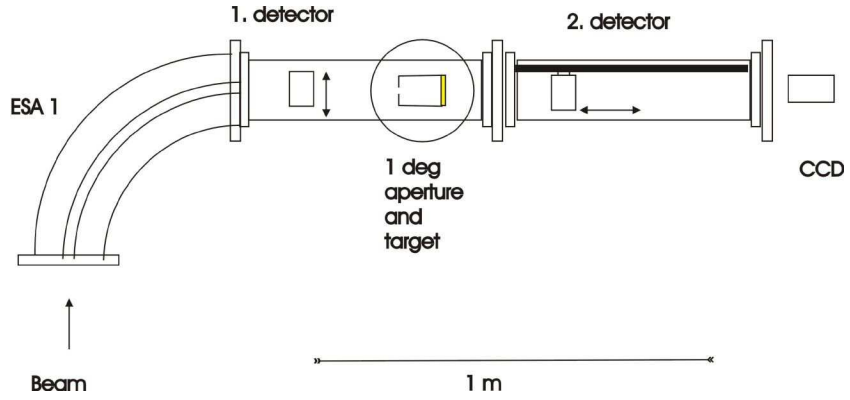

Figure E.11: *The experimental setup for the measurement of multiple angular scattering of antiprotons*

the target, so we should aim to apply amorphous targets, such as carbon and selenium, which are known to contain no crystallites.

E.6.1 Experimental technique

Figure E.11 shows the suggested setup. It consists of the first half of our ESA apparatus, where antiprotons in the energy range 10 – 100 keV from the ASACUSA RFQD are energy selected, followed by a 1° aperture.

A channelplate detector fitted with a fluorescent screen and readout by a CCD camera records the total distribution of the antiprotons transmitted through the target.

Annihilation of the antiprotons in the detector will (infrequently) give rise to recoil tracks that may substantially broaden the angular distributions. Different techniques for deconvolution may be envisaged. Which method will work best may be estimated only through tests with real beams, and are hence part of the proposed experiment.

In conclusion, we suggest measuring the multiple angular scattering distributions of 10 – 100 keV antiprotons transmitted through amorphous, thin targets consisting of carbon or selenium.

Bibliography

[1] M. Iwasaki, S. Nakamura, K. Shigaki, Y. Shimizu, H. Tamura, T. Ishikawa, R. Hayano, E. Takada, E. Widmann, H. Outa, M. Aoki, P. Kitching, and T. Yamazaki, Phys. Rev. Lett. 67 (1991) 1246.

[2] T. Yamazaki, E. Widmann, R. Hayano, M. Iwasaki, S. N. Nakamura, K. Shigaki, F. J. Hartmann, H. Daniel, T. von Egidy, P. Hofmann, Y. S. Kim, and J. Eades, Nature 361 (1993) 238.

[3] N. Morita, M. Kumakura, T. Yamazaki, E. Widmann, H. Masuda, I. Sugai, R. S. Hayano, F. E. Maas, H. A. Torii, F. J. Hartmann, H. Daniel, T. von Egidy, B. Ketzer, W. Müller, W. Schmid, D. Horváth, and J. Eades, Phys. Rev. Lett. 72 (1994) 1180.

[4] T. Yamazaki, N. Morita, R. Hayano, E. Widmann, and J. Eades, Phys. Rep. 366 (2002) 183.

[5] M. Hori, J. Eades, E. Widmann, H. Yamaguchi, J. Sakaguchi, T. Ishikawa, R. S. Hayano, H. A. Torii, B. Juhász, D. Horváth, and T. Yamazaki, Phys. Rev. Lett. 87 (2001) 093401.

[6] M. Hori, J. Eades, R. S. Hayano, T. Ishikawa, W. Pirkl, E. Widmann, H. Yamaguchi, H. A. Torii, B. Juhász, D. Horváth, and T. Yamazaki, Phys. Rev. Lett. 91 (2003) 123401.

[7] V. I. Korobov, Phys. Rev. A 54 (1996) R1749.

[8] V. I. Korobov and D. D. Bakalov, Phys. Rev. Lett. 79 (1997) 3379.

[9] V. I. Korobov, Phys. Rev. A 67 (2003) 062501.

[10] Y. Kino et al., Hyperfine Interactions 138 (2001) 179.

[11] Y. Kino, M. Kamimura, and H. Kudo, Nucl. Instrum. Methods Phys. Res. B 214 (2004) 84.

[12] G. Gabrielse, A. Khabbaz, D. S. Hall, C. Heimann, H. Kalinowsky, and W. Jhe, Phys. Rev. Lett. 82 (1999) 3198.

[13] A. M. Lombardi, W. Pirkl, and Y. Bylinsky, in *Proceedings of the 2001 Particle Accelerator Conference, Chicago, 2001*, pages 585–587, IEEE, Piscataway, NJ, 2001.

[14] T. B. Day, Nuovo Cimento 18 (1960) 381.

[15] M. Leon and H. A. Bethe, Phys. Rev. 127 (1962) 636.

[16] M. Hori et al., submitted to PRL.

[17] E. Widmann, J. Eades, T. Ishikawa, J. Sakaguchi, T. Tasaki, H. Yamaguchi, R. S. Hayano, M. Hori, H. A. Torii, B. Juhász, D. Horváth, and T. Yamazaki, Phys. Rev. Lett. 89 (2002) 243402.

[18] D. Bakalov and V. I. Korobov, Phys. Rev. A 57 (1998) 1662.

[19] V. Korobov and D. Bakalov, J. Phys. B: At. Mol. Opt. Phys. 34 (2001) L519.

[20] Y. Kino, N. Yamanaka, M. Kamimura, and H. Kudo, Hyp. Int. 146-147 (2003) 331.

[21] A. Kreissl, A. D. Hancock, H. Koch, T. Köhler, H. Poth, U. Raich, D. Rohmann, A. Wolf, L. Tauscher, A. Nilsson, M. Suffert, M. Chardalas, S. Dedoussis, H. Daniel, T. von Egidy, F. J. Hartmann, W. Kanert, H. Plendl, G. Schmidt, and J. J. Reidy, Z. Phys. C 37 (1988) 557.

[22] G. Ya. Korenman, Elastic scattering and collisional shift of hfs transitions of metastable antiprotonic helium, in *Abstract Book of the Asia-Pacific Few Body Conference (APFB99), Kashiwa, 1999*.

[23] G. Ya. Korenman, N. Yudin, and S. Yudin, Nucl. Instr. Meth. B 214 (2004) 94.

[24] D. D. Bakalov, private communication, 2001.

[25] Y.Yamazaki, Physica Scripta T110 (2004) 286, and Nucl.Instrum.Methods B 154(1999) 174.

[26] E. Fermi and E. Teller, Phys. Rev. 72 (1947) 399.

[27] J.Cohen, Phys. Rev. A 56 (1997) 3583.

[28] J.Cohen, Phys. Rev. A 62 (2000) 022512.

[29] A. Mohri, T. Yuyama, Y. Kiwamoto, Y. Yamazawa, and T. Michishita, Jap. J. Appl. Phys. 37 (1998) L1553, A. Mohri, private communication.

[30] S. Møller, A. Csete, T. Ichioka, H. Knudsen, U. Uggerhøj, and H. Andersen, Phys. Rev. Lett. 88 (2002) 193201.

[31] S. Møller, A. Csete, T. Ichioka, H. Knudsen, U. Uggerhøj, and H. Andersen, Phys. Rev. Lett. 93 (2004) 042502.

[32] S. Eidelman et al., Phys. Lett. B 592 (2004) 1.

[33] M. Niering et al., Phys. Rev. Lett. 84 (2000) 5496.

[34] J. R. Sapirstein and D. R. Yennie, Theory of hydrogenic bound states, in *Quantum Electrodynamics*, edited by T. Kinoshita, pages 560–672, World Scientific, Singapore, 1990.

[35] K. Pachucki, 2003, private communication.

[36] B. de Beauvoir et al., Eur. Phys. J. D12 (2000) 61.

[37] K. Pachucki and U. Jentschura, Phys. Rev. Lett. 91 (2003) 113005.

[38] S. G. Karshenboim, Simple atoms, quantum electrodynamics, and fundamental constants, in *Precision Physics of Simple Atomic Systems*, pages 142–162, Springer, Berlin, Heidelberg, 2003, hep-ph/0305205.

[39] S. G. Karshenboim, Phys. Lett A 225 (1997) 97.

[40] M. S. Fee et al., Phys. Rev. A 48 (1993) 192.

[41] R. S. van Dyck, P. B. Swinberg, and G. Dehmelt, Phys. Rev. Lett. 59 (1987) 26.

[42] G. G. Simon, C. Schmitt, F. Borokowski, and V. Walther, Nucl. Phys. A 333 (1980) 381.

[43] I. Sick, Phys. Lett. B 476 (2003) 62.

[44] T. Udem et al., Phys. Rev. Lett. 79 (1997) 2646.

[45] N. Ramsey, Atomic hydrogen hyperfine structure experiments, in *Quantum Electrodynamics*, edited by T. Kinoshita, pages 673–695, World Scientific, Singapore, 1990.

[46] I. I. Rabi, J. M. B. Kellogg, and J. R. Zacharias, Phys. Rev. 46 (1934) 157.

[47] I. I. Rabi, J. M. B. Kellogg, and J. R. Zacharias, Phys. Rev. 46 (1934) 163.

[48] J. M. B. Kellogg, I. I. Rabi, and J. R. Zacharias, Phys. Rev. 50 (1936) 472.

[49] J. E. Nafe and E. B. Nelson, Phys. Rev. 73 (1948) 718.

[50] A. G. Prodell and P. Kusch, Phys. Rev. 88 (1952) 184.

[51] H. M. Goldenberg, D. Kleppner, and N. F. Ramsey, Phys. Rev. Lett. 8 (1960) 361.

[52] M. Eides, Physics Reports 342 (2001) 63.

[53] S. G. Karshenboim, Can. J. Phys. 77 (1999) 241, hep-ph/971234.

[54] D. Colladay and V. A. Kostelecky, Phys. Rev. D 55 (1997) 6760.

[55] R. Bluhm, V. A. Kostelecky, and N. Russell, Phys. Rev. Lett. 79 (1997) 1432.

[56] R. Bluhm, V. A. Kostelecky, and N. Russell, Phys. Rev. D 57 (1998) 3932.

[57] V. A. Kostelecky, Phys. Rev. Lett. 80 (1998) 1818.

[58] R. Bluhm, V. A. Kosteleck?, and N. Russell, Phys. Rev. Lett. 82 (1999) 2254.

[59] H. Dehmelt, R. Mittleman, R. S. Van Dyck, Jr., and P. Schwinberg, Phys. Rev. Lett. 83 (1999) 4694.

[60] R. K. Mittleman, I. I. Ioannou, H. G. Dehmelt, and N. Russell, Phys. Rev. Lett. 83 (1999) 2116.

[61] D. Bear, R. E. Stoner, R. L. Walsworth, V. A. Kostelecky, and C. D. Lane, Phys. Rev. Lett. 85 (2000) 5038.

[62] D. F. Phillips, M. A. Humphrey, E. M. Mattison, R. E. Stoner, R. F. C. Vessot, and R. L. Walsworth, Phys. Rev. D 63 (2001) 111101.

[63] V. W. Hughes, M. G. Perdekamp, D. Kawall, W. Liu, K. Jungmann, and G. Putlitz, Phys. Rev. Lett. 87 (2001) 111804.

[64] J. M. Link *et al.* (FOCUS collaboration), Phys. Lett. B 556 (2003) 7?

[65] P. J. Mohr and B. N. Taylor, to appear in Review of Modern Physics **76** (2004); also available on web at http://physics.nist.gov/constants.

[66] C. Cesar et al., Phys. Rev. Lett. 77 (1996) 255.

[67] A. G. Martin, K. Helmerson, V. S. Bagnato, G. P. Lafyatis, and D. E. Pritchard, Phys. Rev. Lett. 61 (1988) 2431.

[68] K. Helmerson, A. G. Martin, and D. E. Pritchard, J. Opt. Soc. Am. B 9 (1992) 483.

[69] CERN Courier, July/August 2000.

[70] A. Bianconi et al., Phys.Lett. B 481 (2000) 194.

[71] A.Bianconi et al., Phys. Lett. B 492 (2000) 254.

[72] G.Bendiscioli and D.Kharzeev, Rivista del Nuovo Cimento 17 (1994) 1.

[73] V.G.Ableev et al., Il Nuovo Cimento 107 A (1994) 943.

[74] E.Botta, talk presented at LEAP2000 conference, Venice (2000).

[75] A.Zenoni et al., Phys.Lett. B 461 (1999) 405.

[76] A.Zenoni et al., Phys.Lett. B 461 (1999) 413.

[77] M. Augsburger et al., Phys. Lett. B 461 (1999) 317.

[78] S.Wycech et al., "Nuclear interactions of antiprotons: theory", in the proceedings of the conf. LEAP 98, Nucl. Phys. **A 655** (1999) 257c; Harmand et al., ibidem.

[79] R.Schmidt et al., Phys Rev C 60 (1999) 0543309.

[80] S.Wycech, A.M.Green, and J.A.Niskanen, Phys.Lett. 152 (1985) 308.

[81] G.Q.Liu, J.M.Richard, and S.Wycech, Phys.Lett B260 (1991) 15.

[82] Ye.S.Golubeva and L.A.Kondratyuk, Nucl.Phys. **B** (proc. suppl.) 56A (1997) 103.

[83] E.Friedman and A.Gal, Phys. Lett. B 459 (1999) 43.

[84] E.Friedman and A.Gal, Nucl. Phys. A 658 (1999) 345.

[85] K.V.Protasov, G.Bonomi, E. Rizzini, and A.Zenoni, Eur.Phys.Jour. A 7 (2000) 429.

[86] V.A.Karmanov, K.V.Protasov, and A.Yu.Voronin, Eur.Phys.Jour. A 8 (2000) 429.

[87] A.Bianconi, G.Bonomi, M.P.Bussa, E. Rizzini, L.Venturelli, and A.Zenoni, Phys. Lett. B 483 (2000) 353.

[88] A.Bianconi, G.Bonomi, E. Rizzini, L.Venturelli, and A.Zenoni, Phys. Rev. C 62 (2000) 014611.

[89] A.Bianconi, G.Bonomi, M.P.Bussa, E. Rizzini, L.Venturelli, and A.Zenoni, Europhys. Lett. 54 (2001) 443.

[90] A.Gal, E.Friedman, and C.J.Batty, Phys. Lett. B 491 (2000) 219.

[91] W.Brückner et al., Z.Phys. A335 (1990) 217.

[92] A.Bertin et al., Phys. Lett. B369 (1996) 77.

[93] A.Benedettini et al., Nucl. Phys. B (Proc. Suppl.) 56 A (1997) 58.

[94] W.Brückner et al., Z.Phys. A 339 (1991) 379.

[95] J.Haidembauer, T.Hippchen, K.Holinde, and J.Speth, Z.Phys. A 334 (1989) 467.

[96] A.S.Jensen, in "Antiproton-nucleon and antiproton-nucleus interactions", eds. F.Bradamante, J.-M.Richard and R.Klapish, Ettore Majorana international science series, Plenum Press 1990, p.205.

[97] S.Wycech, talk presented at LEAP2000 conference, Venice (2000).

[98] F.Iazzi et al., Phys. Lett. B 475 (2000) 378.

[99] A.G.Cohen, A. Rújula, and S.L.Glashow, ApJ B 495 (1998) 539.

[100] J.B.Rehm and K.Jedamzik, Phys. Rev. Lett. 81 (1998) 3307.

[101] H.Kurki-Suonio and E.Sihvola, Phys. Rev. D 62 (2000) 103508.

[102] E. Rizzini et al., Phys. Rev. Lett. 89 (2002) 183201.

[103] E. Rizzini et al., Phys. Lett. B 599 (2004) 190.

[104] A.Bianconi et al., Phys. Rev. A 70 (2004) 032501.

[105] M. Amoretti et al., Nature 419 (2002) 456.

[106] G. Gabrielse et al., Phys. Rev. Lett. 89 (2002) 213401.

[107] G. Gabrielse et al., Phys. Rev. Lett. 89 (2002) 233401.

[108] G. Gabrielse, S. L. Rolston, L. Haarsma, and W. Kells, Phys. Lett. A 129 (1988) 38.

[109] G. Gabrielse et al., Phys. Rev. Lett. 93 (2004) 073401.

[110] M. Amoretti et al., Phys. Lett. B 583 (2004) 59.

[111] A. Wolf, Hyp. Int. 76 (1993) 198.

[112] A. Müller and A. Wolf, Hyp. Int. 109 (1997) 233.

[113] A. Vassiliev et al., Rev. Sci. Instr. 71 (2000) 3331.

[114] G. Isaeva et al., Nucl. Instr. Meth. Res. A 411 (1998) 201.

[115] ASACUSA collaboration, Atomic spectroscopy and collisions using slow antiprotons, CERN/SPSC 97-19, CERN/SPSC 2000-04, 1997/2000.

[116] P. Kusch and V. W. Hughes, Atomic and molecular beam spectroscopy, in *Encyclopedia of Physics Vol. XXXVII/1*, pages 1–172, Springer, Berlin, 1959.

[117] W. Paul, Rev. Mod. Phys. 62 (1990) 531.

[118] D. A. Church and H. G. Dehmelt, J. Appl. Phys. 40 (1969) 3421.

[119] M. Kishore and P. Ghosh, Int. J. Mass Spectrom. Ion Phys. 29 (1979) 345.

[120] C.-S. O and H. Schuessler, Int. J. Mass Spectrom. Ion Phys. 40 (1981) 53, J. Appl. Phys. 52 (1981) 1157.

[121] R. B. Moore and G. Rouleau, J. Mod. Optics 39 (1992) 361.

[122] H. G. Dehmelt and F. L. Walls, Phys. Rev. Lett. 21 (1968) 127.

[123] D. J. Wineland and H. G. Dehmelt, J. Appl. Phys. 46 (1975) 919.

[124] L. S. Brown and G. Gabrielse, Rev. Mod. Phys. 58 (1986) 233.

[125] G. Gabrielse, New Scientist 158 (1998) 51.

[126] Y. Maeno, M. Tachikawa, Y. Moriwaki, and T. Shimizu, Jap. J. Appl. Phys. 34 (1995) L174.

[127] R. Blümel, C. Kappler, W. Quint, and H. Walther, Phys. Rev. A 40 (1989) 808.

[128] R. Blümel, Phys. Rev. A 51 (1995) 620.

[129] E. A. Cornell et al., Phys. Rev. Lett. 63 (1989) 1674.

[130] W. Quint et al., Hyp. Int. 132 (2001) 457.

[131] M. Hori, to be submitted to Nucl. Instr. Meth. Phys, Res. A.

[132] M. Hori, K. Yamashita, R. S. Hayano, and T. Yamazaki, Nucl. Instr. Meth. Phys. Res. A 496 (2003) 102.

[133] J. P. Schermann and F. G. Major, Appl. Phys. 16 (1978) 225.

[134] A. Mohri and Y. Yamazaki, Europhys. Lett. 63 (2003) 207.

[135] J. Berkowitz, H. Grad, and H. Rubin, in *Proc. Second United Nations Conf. on the Peaceful Uses of Atomic Energy, Vol. 31*, pages 177–189, United Nations, Geneva, 1958.

[136] A. Mohri, Y. Kiwamoto, T. Yuyama, et al., in *Proceedings of the 27th EPS Conference on Controlled Fusion and Plasma Physics, Vol. 24B (EPS)*, edited by K. Szegoe et al., pages 149–152, 2000.

[137] G. Breit and I. Rabi, Phys. Rev. 38 (1931) 2082.

[138] E. Majorana, Nuovo Cimento 9 (1932) 43.

[139] Y. Yamazaki, Physica Scripta, to be published.

[140] First Point Scientific, Inc., 5330 Derry Ave. Suite J., Agoura Hills, CA 91310.

[141] R. Greaves and J. Moxom, to be published; available at http://www.firstpsi.com.

[142] A. Mills and E. Gullikson, Appl. Phys. Lett. 49 (1986) 1121.

[143] S. Gilbert et al., Appl. Phys. Lett. 70 (1997) 1944.

[144] F. Anderegg et al., Phys. Rev. Lett. 81 (1998) 4875.

[145] R. Greaves and C. Surko, Phys. Rev. Lett. 85 (2000) 1883.

[146] J. Merrison et al., Rev. Sci. Instrum. 74 (2003) 3284.

[147] J. Merrison, N. Hertel, H. Knudsen, S.Stahl, and E. Uggerhøj, Appl. Surf. Science 149 (1999) 11.

[148] A. Mills, Appl. Surf. Science 22 (1980) 273.

[149] D. Schrader, F. Jacobsen, N. Frandsen, and U. Mikkelsen, Phys. Rev. Lett. 69 (1992) 57.

[150] H. Knudsen and J. Reading, Phys. Rep. 212 (1992) 107.

[151] F. Jacobsen, N. Frandsen, H. Knudsen, U. Mikkelsen, and D. Schrader, J. Phys. B 28 (1995) 4691.

[152] F. Jacobsen, N. Frandsen, H. Knudsen, and U. Mikkelsen, J. Phys. B 28 (1995) 4675.

[153] H. Bluhme, H. Knudsen, J. Merrison, and M. Poulsen, Phys. Rev. Lett. 81 (1999) 73.

[154] H. Bluhme, H. Knudsen, J. Merrison, and K. Nielsen, J. Phys. B 32 (1999) 5835.

[155] P. Kruit and F. Read, J. Phys. E 16 (1983) 313.

[156] K. Franzen, N.Kuroda, H.A.Torii, M.Hori, Z.Wang, H.Higaki, S.Yoneda, B.Juhasz, D.Horvath, K. A.Mohri, and Y.Yamazaki, Rev.Sci.Instrum. 74 (2003) 3305.

[157] ICRU (International Commission for Radiation Units) Report 49, Stopping Powers and Ranges for Protons and Alpha Particles, 0-913394-47-5 (1993).

[158] See e.g. S.P. Møller, E. Uggerhøj, H. Bluhme, H. Knudsen, U. Mikkelsen, K. Paludan, and E. Morenzoni, Phys. Rev. A56, 2930 (1997).

[159] R. Golser and D. Semrad, Phys. Rev. Lett. 66 (1991) 1831.

[160] A. Schiefermüller, R. Golser, R. Stohl, and D. Semrad, Phys. Rev. A 48 (1993) 4467.

[161] K. Eder et al., Phys. Rev. Lett. 79 (1997) 4112.

[162] See e.g. C. Auth, A. Mertens, H. Winter and A. Borisov, Phys. Rev. Lett. 81 4831 (1998). M. Penalba, J.I. Juaristi, E. Zarate, A. Arnau and P. Bauer, Phys. Rev. A 64, 012902 (2001) and J.I. Juaristi et al., Phys. Rev. Lett. 84 2124 (2000).

[163] See e.g P. Hvelplund, H. Knudsen, U. Mikkelsen, E. Morenzoni, S.P. Møller, E. Uggerhøj and T. Worm J. Phys.B27, 925 (1994).

[164] See e.g. H.H. Andersen, J. Bøttiger ,H. Knudsen, P. Møller Pedersen and T. Wohlenberg Phys. ReV. A10, 1568 (1974).

[165] H. Andersen, F. Besenbacher, P. Loftager, and W. Møller, Phys. Rev. A21 (1980) 1891.

[166] H. Andersen, J. Bøttiger, and H. Knudsen, Radiat. Eff. 13 (1972) 203.